



EXTENDING RESOLUTION IN ALL DIRECTIONS:
IMAGE SCANNING MICROSCOPY AND
METAL-INDUCED ENERGY TRANSFER

SEBASTIAN ISBANER

EXTENDING RESOLUTION IN ALL DIRECTIONS:
IMAGE SCANNING MICROSCOPY AND
METAL-INDUCED ENERGY TRANSFER

Dissertation

zur Erlangung des mathematisch-naturwissenschaftlichen
Doktorgrades
"Doctor rerum naturalium"
der Georg-August-Universität Göttingen

im Promotionsprogramm

Physics of Biological and Complex Systems
der Göttingen Graduate School of Neurosciences, Biophysics,
and Molecular Biosciences (GGNB)
der Georg-August University School of Science (GAUSS)

vorgelegt von

SEBASTIAN ISBANER
aus Bremerhaven.
Göttingen, Dezember 2018

BETREUUNGS-AUSSCHUSS

Prof. Dr. Jörg Enderlein (Referent)
Drittes Physikalisches Institut - Biophysik
Georg-August-Universität Göttingen

Prof. Dr. Helmut Grubmüller
Theoretical and Computational Biophysics
Max-Planck-Institut für Biophysikalische Chemie, Göttingen

Prof. Dr. Andreas Janshoff
Institut für Physikalische Chemie
Georg-August-Universität Göttingen

PRÜFUNGSKOMMISSION

REFERENT: Prof. Dr. Jörg Enderlein
Drittes Physikalisches Institut - Biophysik
Georg-August-Universität Göttingen

KORREFERENT: Prof. Dr. Helmut Grubmüller
Theoretical and Computational Biophysics
Max-Planck-Institut für Biophysikalische Chemie, Göttingen

WEITERE MITGLIEDER DER PRÜFUNGSKOMMISSION

Prof. Dr. Andreas Janshoff
Institut für Physikalische Chemie
Georg-August-Universität Göttingen

Prof. Dr. Fred S. Wouters
Institut für Neuropathologie
Universitätsklinikum Göttingen

Dr. Alexander Egner
Laser-Laboratorium Göttingen

Dr. Sarah Adio
Institut für Microbiologie und Genetik
Georg-August-Universität Göttingen

TAG DER MÜNDLICHEN PRÜFUNG: 13.02.2019

EXTENDING RESOLUTION IN ALL DIRECTIONS:
IMAGE SCANNING MICROSCOPY AND
METAL-INDUCED ENERGY TRANSFER

Dissertation

to acquire the doctoral degree in mathematics and natural science
"Doctor rerum naturalium"
at the Georg-August-Universität Göttingen

within the doctoral degree program

Physics of Biological and Complex Systems
of the Göttingen Graduate School of Neurosciences, Biophysics,
and Molecular Biosciences (GGNB)
of the Georg-August University School of Science (GAUSS)

submitted by

SEBASTIAN ISBANER
from Bremerhaven, Germany
Göttingen, December 2018

THESIS COMMITTEE

Prof. Dr. Jörg Enderlein
Third Institute of Physics - Biophysics
Georg-August-University Göttingen

Prof. Dr. Helmut Grubmüller
Theoretical and Computational Biophysics
Max Planck Institute for Biophysical Chemistry, Göttingen

Prof. Dr. Andreas Janshoff
Institute for Physical Chemistry
Georg-August-University Göttingen

EXAMINATION BOARD

FIRST REFEREE: Prof. Dr. Jörg Enderlein
Third Institute of Physics - Biophysics
Georg-August-University Göttingen

SECOND REFEREE: Prof. Dr. Helmut Grubmüller
Theoretical and Computational Biophysics
Max Planck Institute for Biophysical Chemistry, Göttingen

OTHER MEMBERS OF THE EXAMINATION BOARD:

Prof. Dr. Andreas Janshoff
Institute for Physical Chemistry
Georg-August-University Göttingen

Prof. Dr. Fred S. Wouters
Institute for Neuropathology
University Medical Center Göttingen

Dr. Alexander Egner
Laser Laboratory Göttingen

Dr. Sarah Adio
Institute for Microbiology and Genetics
Georg-August-University Göttingen

DATE OF ORAL EXAMINATION: 13.02.2019

ABSTRACT

Fluorescence microscopy is a powerful tool in the life sciences and is used to study structure and function on length scales from cells down to single molecules. In recent years, fluorescence microscopy has seen enormous improvements on the sensitivity to detect single molecules and on the resolution to look at ever smaller details. However, the resolution of an optical microscope is fundamentally limited by the diffraction limit of light. This limit can be bypassed using superresolution methods, but they often come with a trade-off against the complexity of the method which limits its wide application. In this thesis, we present three techniques that each improve the resolution of fluorescence microscopy: First, we increased the lateral resolution and the contrast of a confocal spinning disk microscope with image scanning microscopy. We developed a software package that controls the image acquisition and performs the image reconstruction. This allows to upgrade confocal spinning disk systems with a superresolution option without changing the optical path of the microscope. Second, we used metal-induced energy transfer to increase the axial resolution. We localized single emitters on DNA origami nanostructures with a precision of 5 nm along the optical axis and demonstrated colocalization of up to three emitters. This method allows exceptional axial resolution within a range of 100 nm for microscopes which are able to measure fluorescence lifetimes. Third, we developed an algorithm to correct dead-time artifacts in fluorescence lifetime imaging. This enabled us to accurately measure fluorescence lifetimes at high count rates which allows to increase the frame rate and thereby the time resolution of fluorescence lifetime imaging. All our methods extend the resolution in a different direction and thereby expand the capabilities of fluorescence microscopy.

ZUSAMMENFASSUNG

Die Fluoreszenzmikroskopie ist eine bedeutende Methode in den Lebenswissenschaften zur Erforschung von Struktur und Funktion auf Längenskalen von Zellen bis hin zu einzelnen Molekülen. In den letzten Jahren hat die Fluoreszenzmikroskopie enorme Verbesserungen hinsichtlich der Empfindlichkeit der Detektion einzelner Moleküle und der Auflösung immer kleinerer Strukturen erfahren. Die Auflösung eines optischen Systems ist jedoch grundsätzlich durch das Beugungslimit des verwendeten Lichts begrenzt. Dieses kann zwar mit hochauflösenden Methoden umgangen werden, die gesteigerte Auflösung geht allerdings oft auf Kosten erhöhter methodischer Komplexität, was ihre breite Anwendung beschränkt. In dieser Arbeit stellen wir drei Methoden vor, die eine Verbesserung der Auflösung eines Fluoreszenzmikroskops bieten: Im ersten Teil haben wir die laterale Auflösung und den Kontrast eines konfokalen Spinning-Disk-Mikroskops mithilfe des Image-Scanning-Microscopy-Verfahrens erhöht. Wir haben ein Softwarepaket entwickelt, das die Bilderfassung steuert und die Bildrekonstruktion durchführt. Dadurch können Spinning-Disk-Mikroskope zu hochauflösenden Mikroskopen aufgerüstet werden, ohne dass der Strahlengang des Mikroskops verändert werden muss. Im zweiten Teil haben wir das Phänomen des metallinduzierten Energietransfers zunutze gemacht, um die axiale Auflösung zu erhöhen. Wir haben damit einzelne Emitter auf DNA-Origami-Nanostrukturen mit einer Genauigkeit von 5 nm auf der optischen Achse lokalisiert und die Kolo-kalisation von bis zu drei Emittern gezeigt. Dieses Verfahren ermöglicht Fluoreszenzlebensdauer-Mikroskopen eine herausragende axiale Auflösung innerhalb eines Bereichs von etwa 100 nm. Im dritten Teil haben wir einen Algorithmus entwickelt, um Totzeit-Artefakte in der Fluoreszenzlebensdauer-Mikroskopie zu korrigieren. Wir haben damit genaue Messungen der Fluoreszenzlebensdauer bei hohen Zählraten durchführen können, was es erlaubt, die Bildfrequenz und damit die Zeitauflösung der Fluoreszenzlebensdauer-Mikroskopie zu erhöhen. Alle unsere Methoden erhöhen die Auflösung in eine andere Richtung und erweitern dadurch das Anwendungsspektrum der Fluoreszenzmikroskopie.

AFFIDAVIT

Hereby, I declare that the presented thesis has been written independently and with no other sources and aids than quoted.

Parts of this thesis and some figures have been published in the articles listed below.

LIST OF RELATED PUBLICATIONS

*Sebastian Isbaner*¹, Narain Karedla¹, Daja Ruhlandt, Simon Christoph Stein, Anna Chizhik, Ingo Gregor, and Jörg Enderlein. "Dead-time correction of fluorescence lifetime measurements and fluorescence lifetime imaging." In: *Optics Express* 24.9 (May 2, 2016), pp. 9429–9445. DOI: [10.1364/OE.24.009429](https://doi.org/10.1364/OE.24.009429)

Thilo Baronsky, Daja Ruhlandt, Bastian Rouven Brückner, Jonas Schäfer, Narain Karedla, *Sebastian Isbaner*, Dirk Hähnel, Ingo Gregor, Jörg Enderlein, Andreas Janshoff, and Alexey I. Chizhik. "Cell-Substrate Dynamics of the Epithelial-to-Mesenchymal Transition." In: *Nano Letters* 17.5 (May 10, 2017), pp. 3320–3326. DOI: [10.1021/acs.nanolett.7b01558](https://doi.org/10.1021/acs.nanolett.7b01558)

Arindam Ghosh, *Sebastian Isbaner*, Manoel Veiga-Gutiérrez, Ingo Gregor, Jörg Enderlein, and Narain Karedla. "Quantifying Microsecond Transition Times Using Fluorescence Lifetime Correlation Spectroscopy." In: *The Journal of Physical Chemistry Letters* 8.24 (Dec. 21, 2017), pp. 6022–6028. DOI: [10.1021/acs.jpcllett.7b02707](https://doi.org/10.1021/acs.jpcllett.7b02707)

Sebastian Isbaner, Narain Karedla, Izabela Kaminska, Daja Ruhlandt, Mario Raab, Johann Bohlen, Alexey Chizhik, Ingo Gregor, Philip Tinefeld, Jörg Enderlein, and Roman Tsukanov. "Axial Colocalization of Single Molecules with Nanometer Accuracy Using Metal-Induced Energy Transfer." In: *Nano Letters* 18.4 (Apr. 11, 2018), pp. 2616–2622. DOI: [10.1021/acs.nanolett.8b00425](https://doi.org/10.1021/acs.nanolett.8b00425)

Shama Sograte-Idrissi, Nazar Oleksiievets, *Sebastian Isbaner*, Mariana Eggert-Martinez, Jörg Enderlein, Roman Tsukanov, and Felipe Opazo. "Nanobody Detection of Standard Fluorescent Proteins Enables Multi-Target DNA-PAINT with High Resolution and Minimal Displacement Errors." In: *Cells* 8.1 (Jan. 10, 2019), p. 48. DOI: [10.3390/cells8010048](https://doi.org/10.3390/cells8010048)

Göttingen, December 2018

¹ These authors contributed equally to this work.

CONTENTS

| | | |
|-------|--|----|
| 1 | INTRODUCTION | 1 |
| 2 | FUNDAMENTALS | 3 |
| 2.1 | Motivation | 3 |
| 2.2 | Fluorescence | 4 |
| 2.3 | Time Correlated Single Photon Counting | 8 |
| 2.3.1 | TCSPC Hardware | 9 |
| 2.3.2 | TCSPC Schemes | 11 |
| 2.4 | Theory of Metal-induced Energy Transfer | 13 |
| 2.4.1 | Oscillating Dipole | 13 |
| 2.4.2 | Electric Field of a Dipole Near a Metal Surface | 16 |
| 2.4.3 | Metal-induced Energy Transfer | 20 |
| 2.4.4 | Angular Distribution of Radiation Near a Metal Surface | 23 |
| 3 | CONFOCAL SPINNING DISK IMAGE SCANNING MICROSCOPY | 25 |
| 3.1 | Introduction | 25 |
| 3.2 | Theory | 29 |
| 3.2.1 | ISM Theory | 29 |
| 3.2.2 | Image Reconstruction | 29 |
| 3.3 | Methods | 33 |
| 3.3.1 | Setup | 33 |
| 3.3.2 | Software | 33 |
| 3.4 | Results | 35 |
| 3.4.1 | Spinning Disk Trigger Signal | 35 |
| 3.4.2 | Reference Measurements | 36 |
| 3.4.3 | Image Artifacts | 38 |
| 3.4.4 | Example 1: Fluorescent Beads | 40 |
| 3.4.5 | Example 2: Argo-SIM Fluorescent Slide | 42 |
| 3.4.6 | Example 3: 3D Multi-Color Imaging of Cells | 43 |
| 3.5 | Discussion | 46 |
| 4 | AXIAL CO-LOCALIZATION USING MIET | 49 |
| 4.1 | Introduction | 49 |
| 4.2 | Methods | 55 |
| 4.2.1 | Sample Preparation | 55 |
| 4.2.2 | Setup | 56 |
| 4.2.3 | Measurement Procedure | 58 |
| 4.2.4 | Data Analysis | 59 |
| 4.3 | Results | 63 |
| 4.3.1 | Axial Localization of Single Emitters | 63 |
| 4.3.2 | Co-localization of Two Emitters | 70 |
| 4.3.3 | Multi-Emitter Co-localization of Three Emitters | 80 |

CONTENTS

| | | |
|-------|---|-----|
| 4.4 | Discussion | 84 |
| 4.5 | Outlook – MIET with DNA-PAINT | 87 |
| 4.5.1 | Proof-of-Principle Experiments | 87 |
| 5 | DEAD-TIME CORRECTION FOR TCSPC SYSTEMS | 91 |
| 5.1 | Introduction | 91 |
| 5.2 | Theory | 93 |
| 5.2.1 | Distortion Effects in TCSPC Measurements | 93 |
| 5.2.2 | Dead-time Effects on TCSPC Histograms | 96 |
| 5.2.3 | Determination of the Photon Hit Rate | 99 |
| 5.2.4 | Determination of Detector and Electronics Dead-times | 101 |
| 5.3 | Methods | 105 |
| 5.3.1 | Monte Carlo Simulations | 105 |
| 5.3.2 | Software | 105 |
| 5.3.3 | Setup for Cell Measurements | 105 |
| 5.3.4 | Setup for Solution Measurements | 106 |
| 5.3.5 | Cell Culture and Staining | 106 |
| 5.4 | Results | 108 |
| 5.4.1 | Numerical Simulation of Dead-time Correction | 108 |
| 5.4.2 | Fluorescence Decay Measurements on Dye Solution | 109 |
| 5.4.3 | Fluorescence Lifetime Imaging | 110 |
| 5.5 | Discussion | 116 |
| 6 | CONCLUSION | 119 |
| A | OTHER CONTRIBUTIONS | 121 |
| A.1 | Cell-Substrate Dynamics of the Epithelial-to-Mesenchymal Transition | 122 |
| A.2 | Quantifying Microsecond Transition Times Using Fluorescence Lifetime Correlation Spectroscopy | 124 |
| A.3 | Multi-Target Exchange-PAINT with Nanobodies | 126 |
| | BIBLIOGRAPHY | 129 |

LIST OF FIGURES

| | | |
|-------------|---|----|
| Figure 2.1 | Jablonski diagram | 5 |
| Figure 2.2 | Spectrum of Atto647N in PBS | 6 |
| Figure 2.3 | TCSPC principle | 8 |
| Figure 2.4 | TCSPC setup | 9 |
| Figure 2.5 | TCSPC scheme | 11 |
| Figure 2.6 | Angular distribution of radiation of a dipole | 15 |
| Figure 2.7 | Geometry of a plane wave refracted at a planar interface | 17 |
| Figure 2.8 | Emission power | 19 |
| Figure 2.9 | Local quantum yield and collection efficiency | 21 |
| Figure 2.10 | MIET brightness and emission channels | 22 |
| Figure 2.11 | Angular distribution of radiation | 23 |
| Figure 3.1 | Principle of CSDISM | 26 |
| Figure 3.2 | Principle of ISM | 30 |
| Figure 3.3 | ISM image reconstruction algorithm | 31 |
| Figure 3.4 | CSDISM setup | 34 |
| Figure 3.5 | Trigger signal timing | 36 |
| Figure 3.6 | Reference measurement | 37 |
| Figure 3.7 | Reconstruction artifacts | 38 |
| Figure 3.8 | CSDISM Example 1: Fluorescent beads | 41 |
| Figure 3.9 | Resolution enhancement factor | 41 |
| Figure 3.10 | Example 2: Argo-SIM slide | 42 |
| Figure 3.11 | Multi-color CSDISM image of a fixed cell | 44 |
| Figure 3.12 | Example 3: 3D multi-color CSDISM | 45 |
| Figure 4.1 | Orientation factor in FRET | 53 |
| Figure 4.2 | DNA origami pillar | 56 |
| Figure 4.3 | FLIM Setup | 57 |
| Figure 4.4 | Scan image of the sample | 58 |
| Figure 4.5 | Data analysis | 59 |
| Figure 4.6 | MIET curve for the pillar experiments | 61 |
| Figure 4.7 | Results: single labeled pillar | 64 |
| Figure 4.8 | 3D-DNA-PAINT experiment | 66 |
| Figure 4.9 | MIET curve error | 68 |
| Figure 4.10 | On-times of the filtered T ₂ data | 71 |
| Figure 4.11 | Lifetime Histograms of T ₂ | 72 |
| Figure 4.12 | Height histograms of T ₂ | 72 |
| Figure 4.13 | Distance histograms of T ₂ | 74 |
| Figure 4.14 | Simulation of the T ₂ pillar lifetime fitting | 75 |
| Figure 4.15 | Protection from photobleaching by MIET | 76 |
| Figure 4.16 | Height histogram of B ₂ and layer thickness estimation | 78 |
| Figure 4.17 | T ₃ measurement | 80 |

| | | |
|-------------|---|-----|
| Figure 4.18 | Localization of three emitters | 82 |
| Figure 4.19 | Summary of the smMIET experiments on the DNA origami pillar | 84 |
| Figure 4.20 | smMIET combined with DNA-PAINT | 88 |
| Figure 5.1 | Dead-time effects in different TCSPC schemes | 94 |
| Figure 5.2 | Schematic of possible effects of detector and electronics dead-time | 96 |
| Figure 5.3 | Schematic of two successive photon recording events | 97 |
| Figure 5.4 | Monte Carlo Simulation with dead-time | 99 |
| Figure 5.5 | Inter-photon time distribution | 100 |
| Figure 5.6 | Autocorrelation function | 103 |
| Figure 5.7 | Setup for FLIM and solution measurements | 107 |
| Figure 5.8 | Dead-time correction of simulated data | 109 |
| Figure 5.9 | Measured TCSPC histograms and correction | 110 |
| Figure 5.10 | Dead-time correction: solution | 111 |
| Figure 5.11 | FLIM of a cell with high laser power | 112 |
| Figure 5.12 | FLIM of a cell with low laser power | 114 |
| Figure 5.13 | FLIM of a cell – line plots | 115 |
| Figure A.1 | Cell-Substrate Dynamics of EMT | 122 |
| Figure A.2 | Quantifying Microsecond Transition Times using FLCS | 124 |
| Figure A.3 | Multi-Target Exchange-PAINT with Nanobodies | 126 |

LIST OF TABLES

| | | |
|-----------|-----------------------------------|----|
| Table 4.1 | Microscope Resolution | 51 |
| Table 4.2 | Layers for MIET curve calculation | 61 |
| Table 4.3 | Heights of single labeled pillars | 65 |
| Table 4.4 | Heights of dual labeled pillars | 73 |
| Table 4.5 | Height difference T2 | 74 |
| Table 4.6 | Heights T3 | 81 |
| Table 4.7 | Height difference T3 | 83 |

ACRONYMS

| | |
|-----------|---|
| NA | Numerical Aperture |
| QY | Quantum Yield |
| TCSPC | Time-Correlated Single Photon Counting |
| CSD | Confocal Spinning Disk |
| ISM | Image Scanning Microscopy |
| CSDISM | Confocal Spinning Disk Image Scanning Microscopy |
| PSF | Point Spread Function |
| OTF | Optical Transfer Function |
| SIM | Structured Illumination Microscopy |
| AOTF | Acousto-Optical Tunable Filter |
| FPGA | Field-Programmable Gate Array |
| DMD | Digital Micromirror Device |
| MIET | Metal-Induced Energy Transfer |
| smMIET | single-molecule Metal-Induced Energy Transfer |
| FRET | Förster Resonance Energy Transfer |
| DNA-PAINT | DNA Points Accumulation for Imaging in Nanoscale Topography |
| STED | Stimulated Emission Depletion |
| RESOLFT | Reversible Saturable Optical Fluorescence Transitions |
| STORM | Stochastic Optical Reconstruction Microscopy |
| PALM | Photoactivation Localization Microscopy |
| TIR | Total Internal Reflection |
| TIRF | Total Internal Reflection Fluorescence |
| vaTIRF | variable angle TIRF |
| SAF | Supercritical Angle Fluorescence |
| SEM | Standard Error of the Mean |
| FWHM | Full Width at Half Maximum |

ACRONYMS

| | |
|--------|--|
| FLIM | Fluorescence Lifetime Imaging |
| SPAD | Single-Photon Avalanche Diode |
| APD | Avalanche Photodiode |
| PMT | Photomultiplier Tube |
| CFD | Constant Fraction Discriminator |
| TDC | Time-to-Digital Converter |
| TAC | Time-to-Analog Converter |
| ADC | Analog-to-Digital Converter |
| TTTR | Time-Tagged Time-Resolved |
| (E)GFP | (Enhanced) Green Fluorescent Protein |
| FLCS | Fluorescence Lifetime Correlation Spectroscopy |
| EMT | Epithelial-to-Mesenchymal Transition |

INTRODUCTION

Fluorescence microscopy has become a powerful tool in modern biology and medicine [6, 7]. The high sensitivity of fluorescence detection together with the high specificity of labeling allows studying living and fixed cells in terms of structure and dynamics. However, fluorescence microscopy is limited by the diffraction of light, rendering all detail smaller than about 200 nm invisible. Many cellular structures are smaller and many cellular processes are carried out by molecules only a few nanometers in size. Huge efforts have been made to overcome this limitation. In the last thirty years, the field has seen tremendous advances by the detection of single fluorescent molecule [8, 9] and the development of superresolution techniques [10–13]. Single molecule techniques have allowed for example to track labeled proteins within cells with nanometer precision [14] and superresolution microscopy techniques have looked at cellular structures with unprecedented detail [15–17]. Spectroscopic techniques such as Förster resonance energy transfer (FRET) have allowed to study biomolecules of a few nanometers in size and advanced our understanding of the structure and function of the cellular machinery at the single molecule level [18, 19].

Improving the spatial resolution of fluorescence microscopy is often a trade-off against the speed or the complexity of the method. The complexity of a method is connected to the alignment and maintenance required to operate the system and to the availability and cost of the equipment needed. The speed of a method is important for high-throughput screening applications which aim at optimizing the data collection efficiency [20, 21]. Furthermore, it is connected to the time resolution (e.g. the frame rate) which is crucial for following fast processes within living cells.

The challenge of fluorescence microscopy today is to resolve fine structures within the cell at the detail of cellular machinery. The demand to optical microscopy and spectroscopy is thus to develop techniques that enable measurements with high resolution in space and time, and are low in complexity to be widely applied. In this work, we present three techniques that each improve the resolution in a different direction:

- Image Scanning Microscopy (ISM) improves the lateral resolution of a confocal microscope. We present an ISM upgrade for a confocal spinning disk system which is easy to implement, improves resolution and contrast, and offers fast image acquisition.

INTRODUCTION

- Metal-induced energy transfer (MIET) is used to resolve single emitters along the optical axis. With this method, emitters can be localized with nanometer precision on the optical axis within a range of more than 100 nm and it has the potential to measure intra-molecular distances of large biomolecular complexes.
- A dead-time correction algorithm enables the accurate determination of fluorescence lifetimes even at high count rates. Because the dead-times induce distortions of the measured fluorescence decay, this limited the acquisition speed of fluorescence lifetime imaging (FLIM). The correction allows FLIM imaging at higher frame rates, i.e. recording data at higher time resolution.

With these three techniques, we expand the toolbox of fluorescence microscopy and spectroscopy and tackle the challenge for higher resolution.

In this chapter, we lay the theoretical foundations for the thesis. We start with a general motivation on fluorescence and then explain the physical background and some key parameters such as the fluorescence lifetime and quantum yield. Following this, we introduce time correlated single photon counting (TCSPC) which we examine in depth with respect to its accuracy at high count rates in Chapter 5. TCSPC is a technique that allows measuring the fluorescence lifetime which is a prerequisite for axial localization using metal-induced energy transfer (MIET) as in Chapter 4. To provide the theoretical background, we give an introduction to the theory of MIET at the end of this chapter.

2.1 MOTIVATION

Fluorescence is an every-day phenomenon and can be observed in nature in living as well as in non-living systems. A fluorescent object has the ability to emit light in a different color than it is illuminated with. Three examples are listed below:

- Minerals such as calcites (CaCO_3) fluoresce in UV to visible light. The source of the fluorescence are impurities in the crystal. These ions are called activators and determine the emission spectrum. Manganese (Mn^{2+}) is the most common source for the red to orange fluorescence of calcite under UV light. Other impurities such as iron or copper may also act as quencher and prevent fluorescence. The fluorescent properties can help to identify origin or composition of a mineral [22].
- The jellyfish species *Aequorea victoria* is famous for its bioluminescence. The protein aequorin can emit flashes of blue light when stimulated by calcium ions. The so-called green fluorescent protein (GFP) converts it into green light that can be seen as a glowing ring around the margin of the jellyfish. Although the biological function of the bioluminescence is not well known, GFP has become famous for many biochemical applications. It is widely used for example in cell biology to study protein expression and in biophysics to label cell structures of interest [23].
- Quinine is probably best known for its use as a malaria drug and as an ingredient of tonic water. The substance can be isolated from the bark of cinchona trees and its fluorescence has

been described already in 1845 by Sir John Herschel which makes it the first known fluorophore [24]. It absorbs UV light (around 350 nm) and fluoresces in bright blue (around 460 nm). Like most organic dyes, quinine has an aromatic ring structure that is responsible for the fluorescence. Electrons in aromatic rings are delocalized in molecular π orbitals, making it an ideal structure for a Hertzian dipole which is the most simple theoretical model of an emitter (see also Section 2.4.1).

The fluorescence can be used to label structures of interest in cells or in biomolecular complexes. The already mentioned GFP can be genetically encoded into proteins, and organic fluorophores can be chemically bound to structures of interest or to antibodies, which in turn bind to structures of interest. The fluorescence signal then is specific to the structures of interest and can be measured with high sensitivity. With appropriate filters in the illumination and detection side of a microscope, the fluorescence from different components can be distinguished and viewed separately. This is important to visualize the interplay of cellular processes and structures. New developments such as superresolution methods have allowed to view cellular machinery and structure in fixed and living cells at unprecedented detail and enabled researchers to ask entirely new questions in biological research [16, 17, 25–27]. In summary, fluorescence microscopy has become an indispensable tool for biological research. In the following section, we will look at fluorescence in more detail.

2.2 FLUORESCENCE

Fluorescence is the process of light absorption and re-emission. Light as a form of energy can be transmitted only in quantized energy portions, the photons. In the quantum mechanical picture, a fluorescent emitter can be seen as an energetic two state system. The system is excited into the higher energetic state by the absorption of a photon. When the system returns back into its ground state, the energy can be released in form of a fluorescent photon (radiative transition). Alternatively, the energy is dissipated into heat or transferred into another excited state and no photon is emitted (non-radiative transition). This model is visualized in a Jablonski diagram, see Fig. 2.1. A state is displayed as a vertical line and transitions between the states by arrows. Because electrons in the fluorescent material interact with the light, the main states are called electronic states. The transition of the singlet ground state S_0 to the first excited state S_1 requires the absorption of a photon with an energy equal to the energy difference of the two states. However, the electronic states have additional vibronic substates which allow many more transitions with slightly different energies. Additionally, thermal fluctuations can slightly shift the energetic states which is the reason that the absorption spectra are broad as for example in Fig. 2.2. Relaxation of the excited vibronic states into

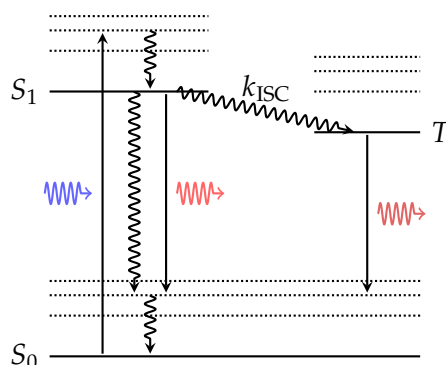


Figure 2.1: Jablonski diagram. Straight black arrows indicate radiative transitions between electronic states. Curly black arrows symbolize non-radiative transitions, and curly colored arrows indicate photon absorption (blue) and emission (red).

the vibronic ground states happens non-radiatively on the picosecond time scale. This leads to a lower energy of the emission which is observed as a shift of the emission spectrum to longer wavelengths as can be seen in Fig. 2.2. The shift between the two spectra is known as the Stokes shift. Furthermore, the fast relaxation of the vibronic states is the reason that emission spectra are usually independent of the excitation wavelength, known as Kasha's rule.

The electronic transition from S_1 to one of the vibronic states of S_0 can occur radiatively or non-radiatively with a probability given by the transition rates k_r and k_{nr} , respectively. In a non-radiative processes to the ground state, the energy of the photon is released as thermal heat to the environment, whereas in a radiative process a photon is emitted by the system. The average time the emitter spends in the excited state is characteristic for the system and is given by

$$\tau = \frac{1}{k_r + k_{nr}}. \quad (2.1)$$

This is the so-called fluorescence lifetime which is usually on the order of nanoseconds (10^{-9} seconds) for organic fluorophores. Another characteristic quantity of an emitter is the quantum yield

$$\text{QY} = \frac{k_r}{k_r + k_{nr}} = k_r \tau. \quad (2.2)$$

It gives the probability that a decay is a radiative process, i.e. what fraction of absorbed photons is again emitted as photons, and is thus connected to the brightness of the emitter. Together with the fluorescent lifetime, these two quantities are the most important characteristics of a fluorophore to describe the interaction with a metal surface in Section 2.4.

The above proposed model is of course a very simplified model. For most organic dyes, an additional state exists: the triplet state (labeled by T in Fig. 2.1). The transition from the singlet S_1 state to the

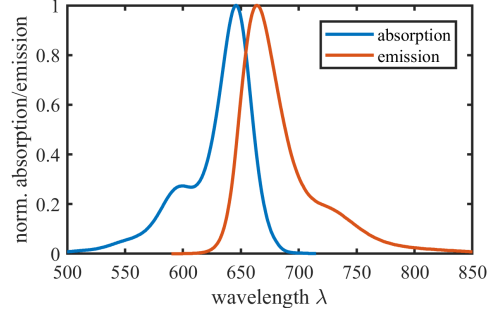


Figure 2.2: Spectrum of Atto647N in PBS. The blue curve shows the absorption spectrum of the dye and the red curve the emission spectrum. The peak of the emission is shifted to longer wavelengths which is known as the Stokes shift. Data provided by the manufacturer ([ATTO-TEC](#)).

triplet state is called inter-system crossing (ICS) and occurs with a rate k_{ICS} . Because the transition requires a spin change it belongs to the so-called forbidden transitions. In practice, there is still a small probability of the transition to occur, resulting in transition rates between the singlet and the triplet states that are several orders of magnitude smaller than the rates between the singlet states. The average residence time in the triplet states is on the order of microseconds to milliseconds during which the emitter is dark. This is often referred to as blinking.

Because the rate for inter-system crossing is orders of magnitude smaller than the fluorescent rate, we can approximate fluorescence as a two state system. Then, the probability that the system is still in the first excited state S_1 after some time t is given by

$$p(t) = \frac{1}{\tau} e^{-\frac{t}{\tau}}, \quad (2.3)$$

where τ is the average time in the excited state as given in Eq. (2.1).

The fluorescent lifetime can be measured by exciting the molecule with a short laser pulse and measuring the time t until a photon is emitted. The arrival time t follows the probability distribution of a fluorescence decay according to Eq. (2.3). The average arrival time is then an estimator of the fluorescence lifetime:

$$\langle t \rangle = \int_0^{\infty} dt t p(t) = \tau. \quad (2.4)$$

The uncertainty of this measurement is $\sigma_{\tau} = \sqrt{\langle t^2 \rangle - \langle t \rangle^2} = \tau$. Repeating the measurement N times reduces the uncertainty of the lifetime to

$$\Delta\tau = \frac{\tau}{\sqrt{N}}. \quad (2.5)$$

This is a simplification because in an experiment one has to account for different factors such as a background or the finite response time

of the photon detector. Therefore, the lifetime is usually determined in a different way: A histogram of arrival times is fitted with $I(t) = A \cdot p(t) + b$ as fit function, where A is the amplitude of the fluorescence decay and b the background. However, Eq. (2.5) is still a good approximation of the error as it provides a lower bound for the error of a fluorescence lifetime measurement. Experimentally, the measurement can be realized by time correlated single photon counting (TCSPC) and will be explained in detail in the next section.

2.3 TIME CORRELATED SINGLE PHOTON COUNTING

With the advent of pulsed lasers and single-photon sensitive detectors, time-resolved spectroscopy has become an important tool in the life sciences, fundamental physics, and chemistry. The sample is illuminated with a short laser pulse and the time-dependent intensity decay of the sample is recorded. The direct recording of this decay is very challenging: Fast processes on the order of nanoseconds require a high time resolution on the order of picoseconds which cannot be achieved with traditional photodiodes and amplifiers. Furthermore, a high number of photons is required to observe the whole decay after one excitation cycle which, for example, is impossible to obtain from a single emitter. Time Correlated Single Photon Counting (TCSPC) solves these problems by exciting the sample with a periodic train of laser pulses. This extends the observation over multiple excitation and emission cycles and the decay can be reconstructed from all single photon events collected over many cycles. The photon flux on the detector can be orders of magnitude less than the repetition rate of the laser. Each detector signal indicates the arrival of a single photon which is recorded as a time stamp with respect to the laser pulse. Only by recording a large number of these events and histogramming the arrival times, the periodic signal is recovered. See Fig. 2.3 for an illustration of this principle for the measurement of a fluorescence lifetime decay.

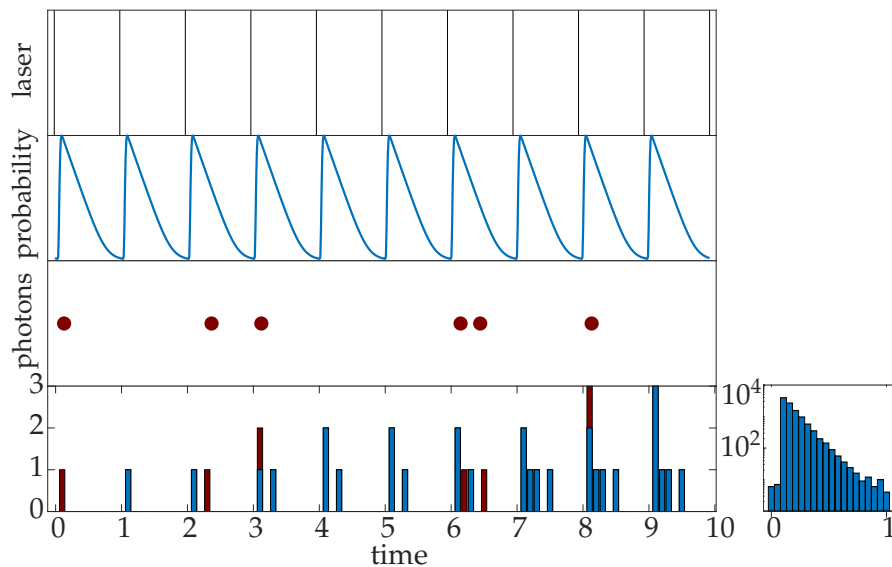


Figure 2.3: TCSPC principle. Top row: A pulsed laser excites fluorescence. The probability of a fluorescence decay is shown in the row below (in logarithmic scale). Less than one photon is detected in one excitation period on average. The detected photons (red dots) are histogrammed (bottom row). Each excitation period shows the full histogram with new photons in red. Right: After many excitation periods, the histogram resembles the decay probability.

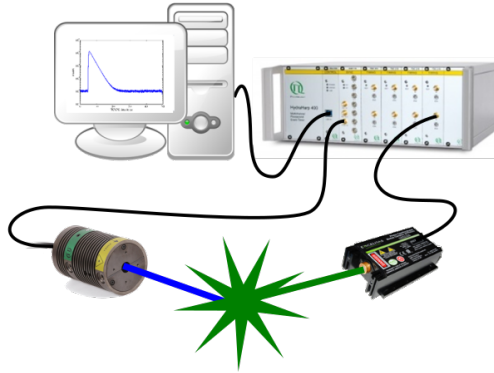


Figure 2.4: A minimal TCSPC setup: A pulsed laser (left) excites fluorescence in the sample which is detected by a fast single-photon counter. Both the laser and the detector are connected to the TCSPC electronics which records the time difference between the laser pulse and the detected photon.

Single-photon arrival times can be recorded at much higher time resolution than analog intensity recording with a precision up to picoseconds. TCSPC can then be used to measure the fluorescence lifetime by using a repetition rate smaller than the inverse of the fluorescence lifetime. Apart from spectroscopy, an important application of TCSPC is ranging with light (lidar) [28]: The reflected light from a target is measured and the return time is proportional to the distance. Combined with a laser scanning setup, this can be used to make a 3D representation of the target and is employed, for example, to make high-resolution maps in geodesy [29] or for control and navigation for autonomous cars [30].

2.3.1 TCSPC Hardware

A TCSPC setup consists of a pulsed excitation source and a detector which both are linked to the TCSPC electronics, see Fig. 2.4. The excitation source provides a reference signal given by the repetition rate of the light pulses, the so-called *sync*. The detector provides an electrical pulse for each photon that it detects. In the TCSPC electronics, both signals are processed and photon events are eventually stored in a computer.

DETECTORS Detectors generate an electrical signal proportional to the incoming light flux. For single-photon counting applications, the detectors generate an electrical pulse upon the incidence of a single photon. Thus, detectors for photon counting applications need to have a high gain in order to produce a useful signal for the TCSPC electronics from a single photon. The signal is usually a short pulse where the width limits the minimum distance between two arriving photons, thus limiting the count rate. The minimum time between

two successive signals is also called the dead-time of the detector. However, for the timing precision of the TCSPC measurement, the timing jitter or the transit time spread (TTS) of the pulse is more important than the pulse shape. Because the TTS is typically much smaller than the response signal of the detector, TCSPC has a much better timing resolution in contrast to analog techniques that record the photo-response of the detector directly [31].

Typical detector types are the photomultiplier tube (PMT) and the single-photon avalanche photodiode (SPAD), and all detector types have their individual strengths and shortcomings. For example, the counting efficiency of PMTs is typically in the range of 10 % to 40 %, limited by the frequency a photo-electron is generated by an incident photon (the so-called quantum efficiency). For SPADs, the quantum efficiency can be $> 70\%$, but a smaller active area makes focusing the light on the SPAD more challenging [32]. Typical values for the dead-time are in the tens of nanoseconds range, limiting the count rate to a few tens of MHz. The timing jitter in SPADs is mainly due to the different depth in which photons are absorbed, resulting in different times for the avalanche built-up [33], and is on the order of 100 ps. A comprehensive review on PMTs, SPADs, and more detector types can be found in Ref. [32].

TCSPC ELECTRONICS The TCSPC electronics converts the output pulses of the detector and an external sync into a timing information. The most important building block in modern TCSPC hardware is the time-to-digital converter (TDC), an electronic timer. It is typically based on a crystal oscillator and converts a time into a digital output. Because the output pulses of the detector may have different amplitudes, a constant fraction discriminator (CFD) ensures triggering at a constant fraction of the pulse amplitude and produces a normed signal for the TDC [34]. Instead of an TDC, older TCSPC hardware typically use a time-to-amplitude converter (TAC) together with an analog to digital converter (ADC). When the TAC is activated, the TAC charges a capacitor until stopped. The charge in the capacitor is proportional to the time between start and stop of the TAC and is read out and converted into a digital signal by the ADC. During the time of the capacitor discharge and the read-out, the TCSPC electronics is unable to process further events. We refer to this as the electronic dead-time. If the dead-time is much shorter than the average time between two photons, TCSPC reaches a near ideal counting efficiency. In particular, the efficiency is much higher than for gated techniques which shift a time-gate over the periodic signal (see for example Ref. [24, Chapter 4]).

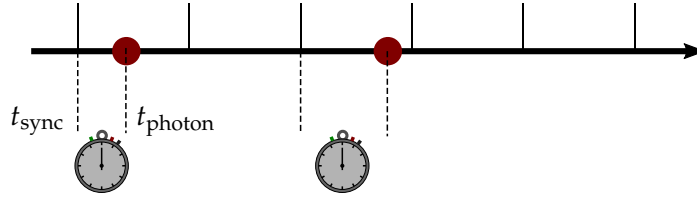


Figure 2.5: TCSPC scheme. Laser pulses (black bars) excite the sample and start a timer. The arrival of a photon (red circle) stops the timer. The measured time $t = t_{\text{sync}} - t_{\text{photon}}$ is used for the TCSPC histogram.

2.3.2 TCSPC Schemes

TCSPC records the the arrival time of a photon t_{photon} with respect to a sync signal t_{sync} . In Fig. 2.5, the vertical bars mark the beginning of a new period from the sync signal. A photon is symbolized by a circle and the arrival time of a photon relative to the laser pulse $t = t_{\text{sync}} - t_{\text{photon}}$ is recorded. In a classical TCSPC system, this is realized by starting a timer at each sync event and stopping it at the arrival of a photon and called “forward start-stop TCSPC”. With the advent of pulsed laser with repetition rates in the MHz regime, this approach became unfeasible: Because in most excitation periods no photon is detected, the TDC needs to be reset at each sync signal. Photons detected during the dead-time of the electronics would be discarded, thus limiting the count rate and making the system less efficient. To avoid this, TCSPC electronics can be operated in reverse mode. Here, the arrival of a photon starts the timer and the next sync stops it. This avoids unnecessary resets of the TDC, and the conversion rate of the timer is equal to the count rate which is usually much smaller than the repetition rate. Care has to be taken if the repetition rate of the laser is unstable. Then, the reference pulses from the light source need to be shifted, so that they arrive after the pulses from the detector. Furthermore, the time axis of the histogram needs to be internally reversed to obtain the decay [35].

Recent TCSPC electronics works in forward start-stop mode, but with an independent timing of the photons and the sync signal [36]. This works even with lasers with high repetition rates because a divider in front of the sync input reduces the input rate so that the period is at least as long as the dead-time of the TDC. Internal logic determines the sync period and re-calculates the sync signals that were divided out. Because the photon TDC is independent of the sync TDC, no photon events are discarded as in classical forward TCSPC. If a photon is detected, the times t_{photon} and t_{sync} of the two TDCs are used to calculate the time difference $t = t_{\text{sync}} - t_{\text{photon}}$ internally. This allows – in principle – to detect several photons per excitation period an furthermore to record the absolute times with respect to the start of the experiment, as described below.

TTTR SCHEME The time t is also called the *micro time* and is distinguished from the global arrival time with respect to the start of the experiment, the *macro time*. Modern TCSPC hardware allows the simultaneous recording of both times, so that not only the TCSPC histogram can be constructed, but also the time trace of the count rate with high time resolution [37]. The macro time is usually recorded on the coarser timescale of the sync, t_{sync} . In this so-called time-tagged time-resolved (TTTR) data format, a stream of events is stored consecutively where each record consists of the arrival times (micro time t and macro time t_{sync}) together with information such as the detection channel. Additional records can be added to synchronize the data stream to the experiment. These so-called markers are for example used in a scanning confocal microscope to indicate a line change or the end of a frame. Later, each photon can be assigned to a line and a pixel number and an intensity image can be constructed. TCSPC histograms in a single pixels can be used to estimate the fluorescence lifetime, enabling Fluorescence Lifetime Imaging (FLIM). The TTTR recording scheme is thus a valuable extension to the above discussed TCSPC schemes and allows to follow processes from picoseconds to seconds in a single measurement.

TTTR is useful for a multitude of techniques in the life sciences such as Fluorescence Correlation Spectroscopy (FCS) [38], Fluorescence Lifetime Correlation Spectroscopy (FLCS) [39, 40], photon-arrival-time interval distribution (PAID) [41, 42], and others. Furthermore, photon counting and antibunching experiments are extensively used in quantum optics experiments and quantum sensing [43].

2.4 THEORY OF METAL-INDUCED ENERGY TRANSFER

Metal-induced Energy Transfer (MIET) describes the phenomenon that a fluorescent emitter is quenched by a metal surface. Experimental studies by Drexhage, Kuhn, and Schäfer in 1968 showed how the fluorescent lifetime of phosphorescent europium chelate complexes changes in proximity to a metal mirror [44]. Their model included the interference of the reflected wave with the electric field of the emitter which was in agreement to the oscillations of the radiative rate they observed. It failed however at distances shorter than the wavelength, where the emitters are quenched due to non-radiative energy transfer from the excited molecule to the metal.

The interaction of a dipole in close proximity to a metal surface has been described theoretically by Kuhn where the dipole is considered as a damped oscillator and involves the calculation of the reflected field at the dipole's position [45]. A few years later, Chance, Prock and Silbey developed a comprehensive description of the energy transfer from a dipole emitter to a metal surface which they termed the energy-flux method [46]. This theory allows to separate the energy flux into the bottom and top half-spaces and gives the exact amount of radiation that propagates through a thin semi-transparent metal film. In contrast to the experiments by Drexhage and coworkers who used a thick metal mirror, the use of a thin metal film allows some part of the radiation to propagate into the dielectric medium below. This enables the optical detection of fluorescence through the metal film which was experimentally demonstrated by Amos and Barnes [47]. A few years later, the detection of single molecules through a metal film was reported [48]. The quenching of the fluorescence due to the interaction with the metal film has then been used to measure nanometer axial distances [49]. Recently, the localization of single fluorescent emitters along the optical axis with a precision of about 3 nm has been demonstrated [50].

An excellent introduction on the physics and the mathematical description of an oscillating dipole in the context of MIET is given in Ref. [51]. In the following, we briefly state the main points and discuss how the properties of an emitter such as fluorescent lifetime or brightness are changed close to a metal surface.

2.4.1 *Oscillating Dipole*

An oscillating dipole is a fundamental source of electromagnetic radiation: a charge oscillating along a line. The charge generates an electric field in space and the oscillations lead to changing electric and magnetic fields, an electromagnetic wave. The emission of many fluorescent molecules can be well described by such a dipole emitter.

We begin by recalling the electric field of a static dipole. The dipole consists of two opposite charges q with a distance d apart and is

characterized by its electric dipole moment $\mathbf{p} = q\mathbf{d}$. The embedding medium is described by its permittivity ε which can be thought of as the microscopic polarizability of the medium. The electric field of the static dipole is given by

$$\mathbf{E}(\mathbf{r}) = \frac{3(\hat{\mathbf{r}} \cdot \mathbf{p})\hat{\mathbf{r}} - \mathbf{p}}{\varepsilon r^3}, \quad (2.6)$$

where \mathbf{r} is the position, $r = |\mathbf{r}|$, and $\hat{\mathbf{r}} = \frac{\mathbf{r}}{r}$. When the charges oscillate with a frequency ω , the electric field becomes a function of time. If we switch to polar coordinates and assume that the dipole is oriented along the polar axis, we can write the electric field as

$$\mathbf{E}(\mathbf{r}) = k_0^2 k \left[\left(-1 - \frac{3i}{kr} + \frac{3}{(kr)^2} \right) (\hat{\mathbf{r}} \cdot \mathbf{p})\hat{\mathbf{r}} + \left(1 + \frac{i}{kr} - \frac{1}{(kr)^2} \right) \mathbf{p} \right] \frac{e^{ikr}}{kr} \quad (2.7)$$

where $k = k_0 n$, $k_0 = \frac{\omega}{c} = \frac{2\pi}{\lambda}$ with the velocity of light c is the wave vector in vacuum, and $n = \sqrt{\varepsilon}$ is the refractive index. The time evolution of the field of the oscillating dipole is given by multiplying $\mathbf{E}(\mathbf{r})$ with the phase factor $e^{-i\omega t}$. Although all of the terms extend to infinity, only a part of it actually transports energy. The total energy flux is given by the time-averaged Poynting vector $\mathbf{S}(\mathbf{r}) = \frac{c}{8\pi} \Re \{ \mathbf{E} \times \mathbf{B}^* \}$, where \Re denotes the real part and $*$ denotes complex conjugation. The magnetic field corresponding to Eq. (2.7) can be computed by means of Maxwell's equation in free space from $i\omega \mathbf{B}(\mathbf{r}, t) = \nabla \times \mathbf{E}(\mathbf{r}, t)$ [52].

Although the emitted energy is constant at any distance from the dipole, it is spread over an area that increases with distance. The surface area of a sphere with radius r around the dipole will increase with r^2 , thus all terms that fall off faster than r^2 will not contribute to the energy flux far away from the emitter. One can show that the contributing terms in Eq. (2.7) are proportional to r^{-1} . These terms are called the far-field and correspond to the part of the field that contribute to the energy transport. In contrast to the far-field, one can also define a near-field. Close to the dipole, the term r^{-3} dominates the electric field and is thus called the near-field of the dipole. In the static limit $k \rightarrow 0$ the whole field reduces to the near field term and is equal to the field of the static dipole in Eq. (2.6).

For the radiation that can be detected optically, we usually consider the far-field. We can neglect components in \mathbf{E} and \mathbf{B} that fall off faster than r^{-1} and compute the Poynting vector as

$$\mathbf{S} = \frac{cnk_0^4}{8\pi r^2} \hat{\mathbf{r}} (|\mathbf{p}|^2 - (\hat{\mathbf{r}} \cdot \mathbf{p})^2) = \frac{cnk_0^4}{8\pi r^2} p^2 \sin^2(\theta) \hat{\mathbf{r}}, \quad (2.8)$$

where the last equal sign holds true when the dipole axis is oriented along the polar axis. The power radiated in a solid angle element $d\Omega = d\phi \sin(\theta) d\theta$ is

$$\frac{d^2 S}{d\Omega} = r^2 S = \frac{cnk_0^4}{8\pi} p^2 \sin^2(\theta), \quad (2.9)$$

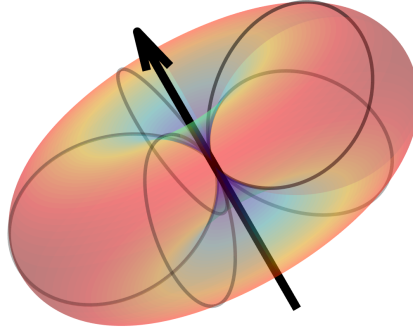


Figure 2.6: Angular distribution of radiation of a dipole. The black arrow represents the orientation of the dipole moment and the color indicates the radiation power which is weak (blue) along the direction of the dipole moment and strong (red) perpendicular to it.

i.e. the angular distribution of radiation follows a simple $\sin^2(\theta)$ law with a toroidal shape, see Fig. 2.6 for an illustration. Note that here and in the following we will use the terms “energy flux” and “emission power” synonymously. The total power of a free dipole is obtained by integrating over a solid angle element $d\Omega$

$$S = \int_0^{2\pi} d\phi \int_0^\pi d\theta \sin(\theta) \frac{d^2S}{d\Omega} = cnk_0^4 p^2 / 3 \quad (2.10)$$

An interesting observation is that the dipole radiation depends on the refractive index of the medium n which is related to the polarizability of the medium. The dielectric properties of the environment thus directly influence the emission of a dipole.

Until now we have used Maxwell’s classical field theory to derive these results. In a quantum mechanical picture, energy is emitted in discretized portions, the photons. A photon is characterized by its energy $\hbar\omega$ and its polarization state. Therefore, the photon energy is given by the oscillation frequency of the dipole ω and Planck’s constant \hbar . The polarization is – in the classical sense – given by the direction of the electric field vector. The angular distribution of radiation can be interpreted as a probability distribution in which direction a photon is emitted. By exciting the molecule repeatedly and measuring the direction of the emitted photons, the $\sin^2(\theta)$ distribution is recovered. The magnitude of the radiation power is proportional to the number of photons emitted by the molecule in unit time (the emission rate), thus for a high magnitude the time the molecule spends in the excited state is reduced. The total radiation power is thus inversely proportional to the excited state lifetime τ . Along the same lines, we can estimate the quantum yield in a different medium: As-

suming that the radiative rate changes proportionally to the emission power of a dipole, we find

$$QY = QY_0 \frac{n}{n_0} \frac{\tau}{\tau_0}, \quad (2.11)$$

where the subscript 0 denotes the known quantum yield and fluorescent lifetime in a medium with refractive index n_0 .

2.4.2 Electric Field of a Dipole Near a Metal Surface

We have already seen that the environment (i.e. the refractive index of the medium) can have an influence on the dipole's emission properties. When a dipole emitter is placed in the vicinity of a dielectric or metallic surface, its local environment is not altered, but at each interface the electro-magnetic (EM) waves can be reflected or transmitted. Reflected waves will interfere with the waves emitted by the dipole, changing the electric field. Furthermore, the near-field of the emitter can couple to the metal and transfer energy which again changes the emission properties, as we will see. Also the propagation of the EM waves is affected: Inside a metal, the energy of an EM wave is attenuated by absorption. This is reflected in the non-zero imaginary part of the refractive index of a metal. As above, we will start the description with the electric field and use it to calculate the energy flux.

We assume a dipole emitter with dipole moment \mathbf{p} is located in the vicinity of an infinitely extended planar interface. For plane wave, Fresnel's equations describe the transmission and reflection at a planar interface, see for example Ref. [52]. We assume the interface is in the xy -plane at $z = 0$ and the incoming wave comes from the upper half-space ($z < 0$). This situation is depicted in Fig. 2.7: the incoming plane wave with wave vector \mathbf{k}_1^+ is traveling in a medium with refractive index n_1 . At the interface to a second medium with refractive index n_2 , the wave is partly reflected (\mathbf{k}_1^-) and partly transmitted (\mathbf{k}_2^+). Here, we decompose the wave vector \mathbf{k}_1^+ into a horizontal component \mathbf{q} (parallel to the surface) and a vertical component w_1 (orthogonal to the surface). For these components the relation $w_1 = \sqrt{k_1^2 - q^2}$ with $k_1 = n_1 k_0$ holds true. Furthermore, we define a new coordinate system spanned by the orthogonal vectors \mathbf{k}_1^\pm , $\hat{\mathbf{e}}_{1p}^\pm$, and $\hat{\mathbf{e}}_s$. $\hat{\mathbf{e}}_{1p}^\pm$ is the unit vector in the plane spanned by \mathbf{k}_1^\pm and the surface normal (p-wave). $\hat{\mathbf{e}}_s$ is the unit vector orthogonal to the plane spanned by \mathbf{k}_1^\pm and the surface normal (s-wave) and is thus parallel to the surface (see Fig. 2.7). Writing the electric field of the dipole in this new coordinate system, we find

$$\mathbf{E}(\mathbf{r}) = \frac{ik_0^2}{2\pi} \iint \frac{d^2\mathbf{q}}{w_1} \left[\hat{\mathbf{e}}_{1p}^\pm (\hat{\mathbf{e}}_{1p}^\pm \cdot \mathbf{p} + \hat{\mathbf{e}}_s (\hat{\mathbf{e}}_s \cdot \mathbf{p})) \right] e^{i\mathbf{q} \cdot (\boldsymbol{\rho} - \boldsymbol{\rho}_0) + iw_1 |z - z_0|}, \quad (2.12)$$

with the position vector $\mathbf{r} = (\boldsymbol{\rho}, z)$ and the position of the emitter $\mathbf{r}_0 = (\boldsymbol{\rho}_0, z_0)$. This is the so-called Weyl representation and conveniently describes the electric field as a sum of plane waves [53]. In

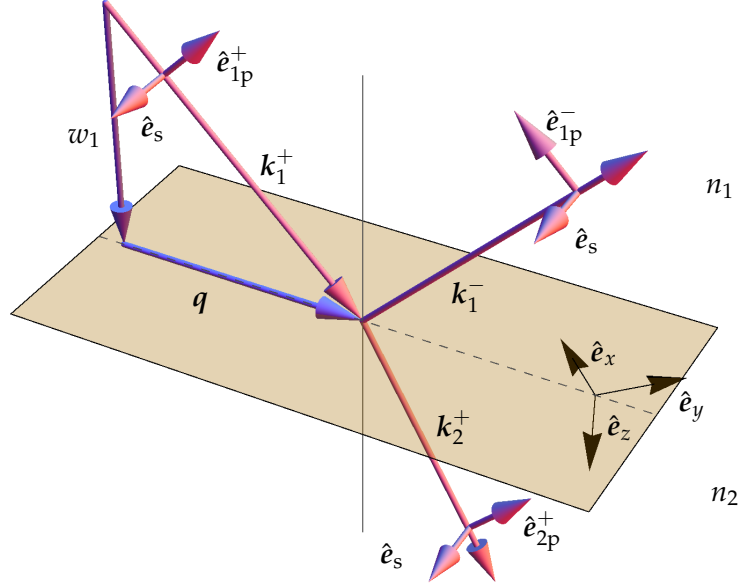


Figure 2.7: Geometry of a plane wave refracted at a planar interface. An incoming wave with wave vector k_1^+ is traveling in a medium with refractive index n_1 . At the interface to a second medium with refractive index n_2 , the wave is partly reflected (k_1^-) and partly transmitted (k_2^+). The coordinate system is chosen so that the interface is in the xy -plane and \hat{e}_z parallel to the surface normal.

this representation we can apply Fresnel's theory to obtain the amplitude of the electric field of the reflected and transmitted waves. For the transmitted wave, the Fresnel coefficients are

$$T_p = \frac{2n_2 n_1 w_1}{w_2 n_1^2 + w_1 n_2^2} \quad \text{and} \quad T_s = \frac{2w_1}{w_1 + w_2} \quad (2.13)$$

for p-waves and s-waves respectively. Thus, the electric field of the transmitted wave is given by

$$E_T(\mathbf{r}) = \frac{ik_0^2}{2\pi} \iint \frac{d^2\mathbf{q}}{w_1} \left[T_p \hat{e}_{1p}^\pm (\hat{e}_{1p}^\pm \cdot \mathbf{p} + T_s \hat{e}_s (\hat{e}_s \cdot \mathbf{p})) \right] e^{i\mathbf{q} \cdot (\boldsymbol{\rho} - \boldsymbol{\rho}_0) + iw_1 |z - z_0|}. \quad (2.14)$$

Similarly, the result for the reflected wave can be obtained. With this result, we are able to calculate the electric field on both sides of the interface: Below the interface it consists simply of the transmitted electric field (Eq. (2.14)), but above the interface, one has to take into account that the electric field is the superposition of the reflected field and the field of the free dipole, Eq. (2.7). With this result, we are able to calculate the Poynting vector \mathbf{S} as in the previous section. Since we are interested in the total energy flux only, we project the Poynting

vector on \hat{z} and integrating over an area A , which encloses the dipole and is parallel to the interface. The energy flux through A is then

$$S_A = \frac{c}{8\pi} \Re \left\{ \iint dA \hat{z} \cdot (\mathbf{E} \times \mathbf{B}^*) \right\}, \quad (2.15)$$

where \mathbf{B} can be obtained from $i\omega\mathbf{B} = \nabla \times \mathbf{E}$ as before. Using the transmitted electric field according to Eq. (2.14) at the interface ($z = 0$) and extending the area A to infinity, we obtain the energy flux into the lower medium which we will denote as S_{\downarrow} . Note that because of energy conservation, the result is identical if one uses the electric field in the lower half-space (between the interface and the emitter position) at the interface.

The total emission power S is obtained from the electric field at the position of the dipole $z = z_0$. One can either use the electric field in the upper or in the lower half-space, yielding the same result.

We will now simply quote the emission powers into the lower medium, S_{\downarrow} , and the total emission power S for the limiting cases of a vertical dipole (denoted by \perp) and a dipole parallel to the surface (denoted by \parallel). It can be shown that these allow us to calculate the emission power of a dipole with any (fixed) orientation α with respect to the surface normal as

$$S(\alpha, z_0) = S_{\perp}(z_0) \cos^2(\alpha) + S_{\parallel}(z_0) \sin^2(\alpha). \quad (2.16)$$

The energy flux for a vertical dipole ($\mathbf{p} = p\hat{z}$) into the lower medium is

$$S_{\perp\downarrow} = \frac{ck_0^4 p^2}{4} \Re \left\{ \int dq \frac{q^3 n_1^* w_1}{k_1 |k_1 w_1|^2} (1 - R_p)(1 + R_p^*) e^{2\Im\{w_1\}z_0} \right\}, \quad (2.17)$$

with Fresnel's reflection coefficient R_p for p-waves and \Im denoting the imaginary part. The total energy flux of a vertical dipole is given by

$$S_{\perp} = \frac{ck_0^4 p^2}{4} \Re \left\{ \int dq \frac{q^3 n_1^* w_1}{k_1 |k_1 w_1|^2} (1 - R_p e^{-2iw_1 z_0}) \right\}. \quad (2.18)$$

For a dipole parallel to the surface, one obtains

$$S_{\parallel\downarrow} = \frac{ck_0^4 p^2}{8} \Re \left\{ \int dq \frac{qn_1^*}{k_1 |w_1|^2} \left[\frac{|w_1|^2}{k_1^2} w_1 (1 - R_p)(1 + R_p^*) + w_1^* (1 - R_s)(1 + R_s^*) e^{2\Im\{w_1\}z_0} \right] \right\}, \quad (2.19)$$

and the total energy flux

$$S_{\parallel} = \frac{ck_0^4 p^2}{8} \Re \left\{ \int dq \frac{qn_1^* w_1}{k_1 |w_1|^2} \left[\frac{|w_1|^2}{k_1^2} (1 + R_p e^{-2iw_1 z_0}) + (1 + R_s e^{-2iw_1 z_0}) \right] \right\}. \quad (2.20)$$

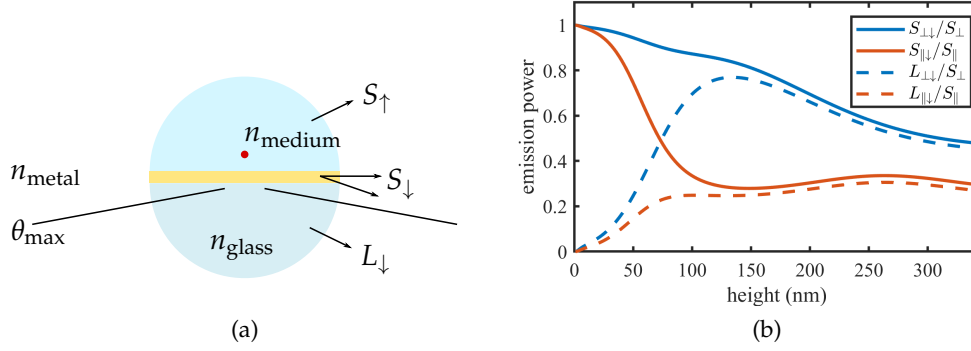


Figure 2.8: Emission power of a dipole emitter ($\lambda = 688 \text{ nm}$) in water close to a 10 nm gold film on top of a glass cover slip. a) The power is radiated into the half space above the emitter (S_{\uparrow}) or into the lower half space (S_{\downarrow}). The energy in the lower half space is partly transferred to the metal and partly radiated into the far-field (L_{\downarrow}). The collection angle θ_{max} of the objective determines the amount of radiation collected by the objective. In b) the total emission power into the lower medium (S_{\downarrow} , solid lines) is compared to the emission power in the far field (L_{\downarrow} , dotted lines). For the calculation of L_{\downarrow} , we assume an ideal collection angle of $\theta_{\text{max}} = 90^\circ$. The x-axis denotes the height of the emitter above the metal surface and the color indicates the orientation of the dipole (vertical: blue, parallel: red).

All integrals are carried out for q ranging from 0 to ∞ and for positive imaginary solutions of $w_1(q)$ only. If one limits the range to q values of propagating waves (i.e. $0 \leq q \leq k_1$), one obtains the energy flux in the far field and thus the amount of radiation that can in principle be detected. Of these propagating waves, only the ones collected by our objective can reach the detector. The maximum collection angle is given by the numerical aperture of the objective, $\text{NA} = n \sin(\theta_{\text{max}})$. Thus, by limiting the values of $q = k \sin(\theta)$ to the angles below θ_{max} , one obtains the *detectable* emission power. In the further discussion, we will use the symbol L instead of S to denote the detectable emission. In Fig. 2.8a, the difference between L and S is visualized. In Fig. 2.8b, we show an example of the emission power of a dipole close to a thin metal film. Whereas the emission power S_{\downarrow} reaches its maximum at the surface, the emission power L_{\downarrow} drops to zero. The energy contained in S_{\downarrow} is thus not transmitted into the far-field but transferred to the metal. Far away from the surface, S_{\downarrow} and L_{\downarrow} are almost equal and only differ by the amount that is absorbed by the metal film.

Until now we considered two infinitely extended media with a single interface for which the Fresnel coefficients are valid. For more complex layer structures that are used in some experiments, one has to take into account also all additional reflections at the interfaces which introduce phase shifts to the reflected electric field. For the i^{th} layer, the phase shift will depend on the layer thickness d_i and its refractive index n_i . Effective reflection coefficients can be calcu-

lated that consist of the Fresnel coefficients and the phase shift. These can be calculated for any number of layers using the transfer-matrix method [54]. These effective coefficients replace then the Fresnel coefficients in Eqs. (2.17) to (2.20) and allow the calculation of S for a dipole emitter on top (or even in between) any structure of layered media. More information on the formalism can be found in Refs. [51, 53, 54].

2.4.3 Metal-induced Energy Transfer

We have already seen earlier that the emission power of a dipole emitter depends on its environment and thereby influences the emission properties such as the fluorescent lifetime. We have extended this to the effect of thin metal films in the proximity of the emitter with the above derivation. We assume that the emitter's internal non-radiative rate k_{nr} stays constant and only the radiative rate k_{r} (not to be confused with the absolute value of the wave vector k in the previous section) changes according to the emission power S ,

$$\frac{k_{\text{r}}}{k_{\text{r}}^{\text{free}}} = \frac{S}{S_{\text{free}}}. \quad (2.21)$$

Here, $k_{\text{r}}^{\text{free}}$ and S_{free} are the radiative rate and the power of a free dipole in the same medium, i.e. far away from any interface ("free space"). $S_{\text{free}} = nS_0 = cnk_0^4 p^2 / 3$ was already calculated in Eq. (2.10).

Assuming the molecule has a quantum yield QY_0 in free space, the fluorescent rate $k_{\text{r}} + k_{\text{nr}} = 1/\tau$ is obtained as

$$\frac{k_{\text{r}}(\alpha, z_0) + k_{\text{nr}}}{k_{\text{r}}^0 + k_{\text{nr}}} = 1 - \text{QY}_0 + \text{QY}_0 \frac{S(\alpha, z_0)}{nS_0} = \frac{\tau_0}{\tau(\alpha, z_0)}. \quad (2.22)$$

Under the same assumption, we can define a local quantum yield

$$\begin{aligned} \text{QY}(\alpha, z_0) &= \frac{k_{\text{r}}(\alpha, z_0)}{k_{\text{r}}(\alpha, z_0) + k_{\text{nr}}} \\ &= \left(1 - \left(\frac{1}{\text{QY}_0} - 1 \right)^{-1} \frac{S(\alpha, z_0)}{nS_0} \right)^{-1} \\ &= 1 - \frac{\tau(\alpha, z_0)}{\tau_0} (1 - \text{QY}_0). \end{aligned} \quad (2.23)$$

In an experimental setting, a fluorescent emitter is often attached to the object of interest by a flexible linker. In solution, the emitter diffuses and randomly rotates. If this rotation diffusion is fast compared to its fluorescence lifetime, the emitter can be considered isotropic. Its radiating power is obtained by averaging over all possible orientations,

$$\begin{aligned} S_{\text{r}}(z_0) &= \frac{1}{2} \int_0^\pi d\theta \sin(\theta) [S_{\perp}(z_0) \cos^2(\theta) + S_{\parallel}(z_0) \sin^2(\theta)] \\ &= \frac{1}{3} S_{\perp}(z_0) + \frac{2}{3} S_{\parallel}(z_0). \end{aligned} \quad (2.24)$$

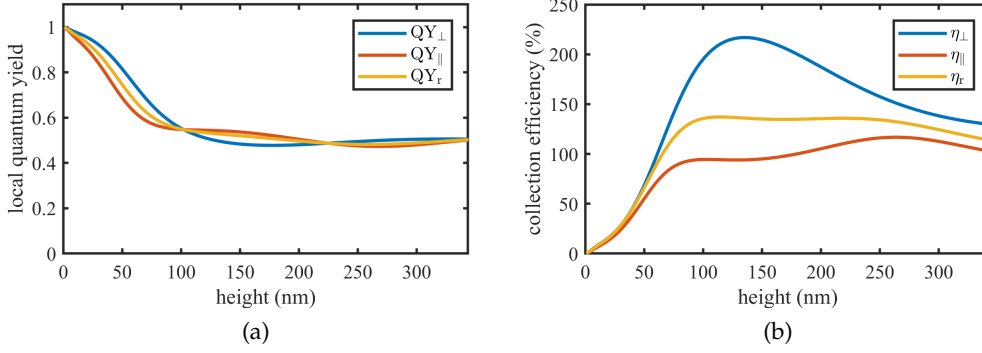


Figure 2.9: a) Local quantum yield according to Eq. (2.23) of a dipole emitter ($\lambda = 688$ nm, $QY_0 = 0.5$) in water close to a 10 nm gold film on top of a glass cover slip. b) Collection efficiency according to Eq. (2.26) of the emission of a dipole as in a) with a 1.49 NA objective. The collection efficiency is normalized to the collection efficiency far away from the surface ($z = 10\lambda$). The color indicates the orientation of the dipole with blue for vertical, red for parallel, and yellow for a randomly oriented emitter.

The emitter “samples” all possible orientations and thus decay probabilities before the emission of a photon, therefore a rate averaging is appropriate here. This result can be used to calculate the lifetime of a quickly rotating emitter, e.g. a dye with a linker, by plugging the result into Eq. (2.22). Further information on the influence of the dye’s rotational diffusion can be found in Ref. [55].

The case is slightly different when we look at an ensemble of randomly oriented, but fixed emitters: Then, we measure the superposition of all the emitters’ lifetimes weighted by their brightness. The measured average lifetime is

$$\tau_{\text{fixed}}(z_0) = \frac{1}{2} \int_0^\pi d\theta \sin(\theta) \tau(\theta, z_0) b(\alpha, z_0). \quad (2.25)$$

In addition to the rates, we can also estimate the relative brightness of an emitter. Assuming a constant excitation rate, the brightness should be proportional to the amount of energy the dipole emits. As we have seen in Section 2.4.2, The amount of radiated energy we can detect is given by the far-field energy L . This allows us to define the collection efficiency η , i.e. the probability to collect a photon in the far field with the objective:

$$\eta(\alpha, z_0) = \frac{L_\downarrow(\alpha, z_0)}{S(\alpha, z_0)}. \quad (2.26)$$

An example for the collection efficiency is shown in Fig. 2.9b. Note that the curves are similar to the curves of L_\downarrow/S in Fig. 2.8b. The difference is that here we take into account the collection angle of a 1.49 NA objective. Note that the curves are normalized to the collection efficiency far away from the surface. The figure shows that

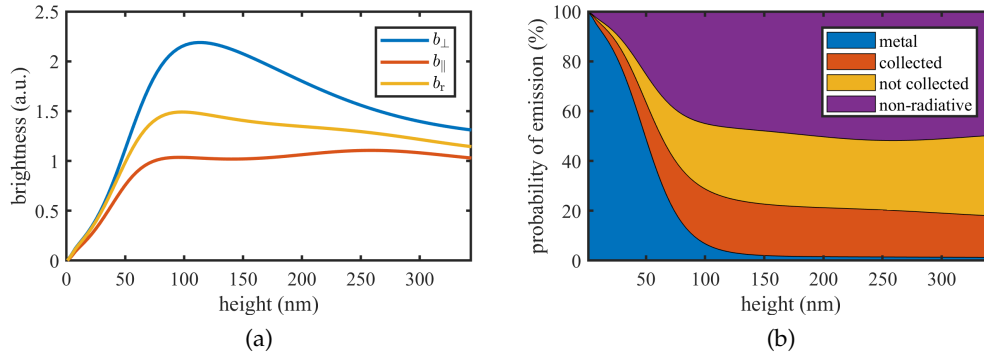


Figure 2.10: a) Brightness of a dipole emitter ($\lambda = 688$ nm, $QY_0 = 0.5$) in water close to a 10 nm gold film on top of a glass cover slip. b) Emission channels of a dipole emitter with the same parameters.

close to the surface the energy transfer to the metal dominates and the collection efficiency is low. But for vertical dipoles, the collection efficiency at around $\lambda/4$ can be a factor 2 higher than in solution.

The collection efficiency is equal to the brightness if every absorbed photon is emitted again. However, if the emitter has additional non-radiative decay channels, we need to consider the local quantum yield. The brightness b is then given as the product of the collection efficiency (Eq. (2.26)) and the local quantum yield (Eq. (2.23))

$$b(\alpha, z_0) \propto \eta(\alpha, z_0) QY(\alpha, z_0). \quad (2.27)$$

In Fig. 2.10a the brightness is shown for an emitter on top of a thin gold film. Because the local quantum yield is increased close to the surface, the brightness there is larger as one would expect by looking at the collection efficiency only. Furthermore, the oscillations at farther distances due to interference effects, which can be seen in both the local quantum yield and the collection efficiency, cancel out and lead to an almost constant brightness.

The different emission channels are summarized in Fig. 2.10b. Internal non-radiative decay channels of the emitter convert the energy into heat (purple). This mechanism is strongly suppressed close the surface (cf. also Fig. 2.9a). There, most of the energy is transferred into the metal (blue). Only a small part is emitted into the far-field and can be detected optically (red and orange). The light emitted into the upper half-space or above the collection angle of the objective is lost (orange), but the remaining part can be detected (red). Although the losses seem very high, the collection efficiency is actually comparable and can even be larger than far away from the surface as we have seen in Fig. 2.9b.

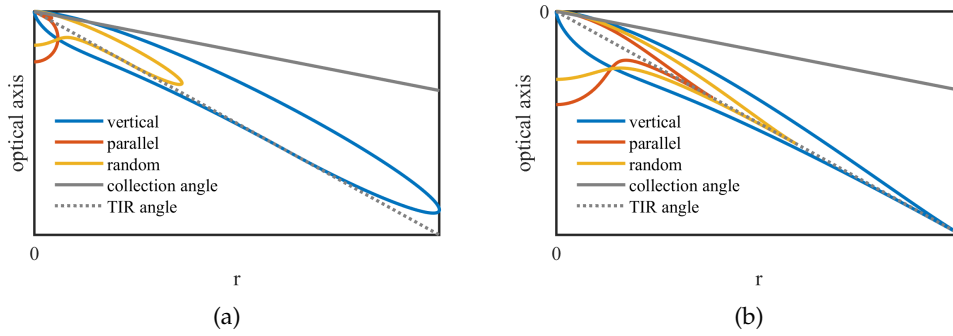


Figure 2.11: Angular distribution of radiation $\frac{d^2S_{\perp}}{d\Omega}(r, z)$ of a dipole emitter at $z_0 = \lambda/20$ in water. a) shows the distribution on a 10 nm gold film and b) on pure glass for different orientations of the dipole (which is located in the top left corner). Additionally, the dashed gray line indicates the angle of total internal reflection (TIR) for water and the solid gray line the maximum collection angle of an NA 1.49 objective. Note that only the radiation into the lower half-space is shown here because of its relevance for the collection efficiency.

2.4.4 Angular Distribution of Radiation Near a Metal Surface

In the last two sections we have studied the total radiated power of a dipole emitter close to an interface, independent of the angle under which the power is emitted. For the angular distribution of a free dipole emitter, we have seen that it follows a $\sin^2(\theta)$ law in the far-field (see Eq. (2.10) and Fig. 2.6). If the dipole comes close to a thin metal film, the near-field coupling increases the radiation towards the metal film. In Fig. 2.8b, we saw that the dipole can emit up to 100% of its radiated energy into the metal. The angular distribution thus becomes highly asymmetric towards the metal. Most of the energy will be transferred to the metal at $q = k_1$, i.e. via an EM wave traveling along the surface [55]. This wave excites oscillations of the electrons in the metal. The energy quanta of these waves are called surface plasmons, thus one can say that the energy of the photons of the dipole emitter is transferred to the surface plasmons of the metal.

Experimentally, the distribution of the far-field is more interesting because it relates to the amount of collected radiation. In Fig. 2.11, the distribution of $\frac{d^2S_{\perp}}{d\Omega}$ is shown for a dipole emitter close to a thin metal film (Fig. 2.11a) in comparison to pure glass (Fig. 2.11b). The emission of a vertical or randomly oriented dipole on gold is mostly above the angle of total internal reflection (TIR) which underlines the need for high NA objectives especially for single molecule studies with MIET.

With this, we conclude the theoretical description of MIET. We have seen how MIET influences the emission power of a dipole emitter, which in turn changes the fluorescence lifetime and the brightness detected through the metal film. Furthermore, we studied the differ-

ent emission channels and the influence of the dipole orientation in dependence of the emitter height above the surface. Further information on the MIET effect can be found in Refs. [51, 53, 54].

CONFOCAL SPINNING DISK IMAGE SCANNING MICROSCOPY

The aim of this project was to supply a combined hard- and software solution for upgrading a Confocal Spinning Disk (CSD) microscope with a superresolution option. Image Scanning Microscopy (ISM) has been shown to increase resolution and contrast in a CSD setup by our colleagues Schulz et al. [56]. To achieve this, the key point is the synchronization between the CSD and a stroboscopic illumination of the sample. Here, we present a software that works with a commercially available FPGA card and controls the complete image acquisition process. The software is written as a plugin in the open-source microscopy software μ Manager [57, 58]. Furthermore, we developed a stand-alone software for image reconstruction in Java. A manuscript is in preparation.

This work was carried out as a joint project with my colleague *Shun Qin*. My focus was on building the setup, testing the hard- and software, and running measurements. Therefore, I will not focus on the software itself, but on the general operating principle, a characterization of the setup, and give some examples of its function. The software will be covered in detail in Shun Qin's doctoral dissertation.

3.1 INTRODUCTION

The confocal spinning disk (CSD) microscope was developed to overcome the speed limitation of confocal microscopes. In the latter, the excitation light is focused into a diffraction-limited spot and fluorescence is detected by a point detector. A pinhole in the image plane suppresses out-of-focus light which gives the confocal microscope its unique sectioning capability. By shifting the laser focus relative to the sample by a known distance, a scanned image can be obtained. Even with a fast scanner the process is limited by the photon throughput of the single point detection, i.e. in an image with 100×100 pixels, each pixel is illuminated only $1/10.000$ of the time. A CSD parallelizes the image acquisition by scanning hundreds of beams through the same number of pinholes directly on a camera, achieving frame rates of up to 1.000 Hz [59]. The idea to use a patterned disk is not new, Paul Nipkow patented this idea already in 1884. It was used in the beginning of the twentieth century in mechanical television for both recording and playback. Today, CSD systems can be found in many labs all over the world and play an important role for fast 3D imaging of fluorescent samples. A good introduction to CSD systems and their applications can be found in Ref. [60, Chapter 10]. Besides its speed, one of

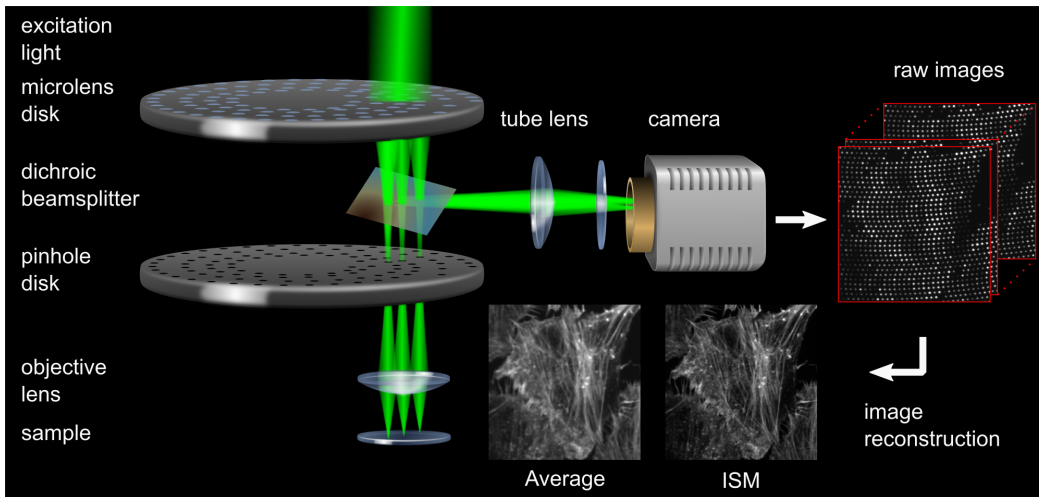


Figure 3.1: Principle of CSDISM. The excitation light is focused through the pinhole disk with the help of a second disk containing microlenses. The light is focused in the sample by the objective which also collects the emission light. The latter passes the pinholes which suppress out-of-focus light. The dichroic beamsplitter redirects the emission light onto the camera. By stroboscopic illumination, raw images are obtained that show the sample modulated by the pinhole pattern. For each frame, the disk is slightly rotated, by which the sample is scanned. Averaging of the raw data yields the standard confocal image. By reassigning the light to the most probable origin, a superresolved ISM image is obtained.

the major advantages of CSD systems over single focus confocal microscopes is the reduced photobleaching of the sample. The quantum efficiency of a modern camera can be an order of magnitude higher than for a scanning confocal microscope with a photomultiplier tube. This reduces the photobleaching and permits the acquisition of long time series [60, 61].

Compared to conventional widefield microscopy, confocal images usually have a better contrast due to sectioning, i.e. rejecting out-of-focus light at the detector. In terms of resolution, a confocal microscope should achieve a better resolution than a widefield microscope. In theory, the effective point-spread function (PSF) is the product of the detection PSF (given by the pinhole) and the excitation PSF. If both PSFs are diffraction limited, a resolution improvement of $\sqrt{2}$ should be achieved with a confocal microscope [62]. In practice, this is impossible because a diffraction limited detection PSF requires a pinhole size close to zero which implies also zero signal at the detector. Usually, the pinhole is chosen to be of similar size as the PSF to detect most of the light emitted by the sample. It can be shown that in this case the lateral resolution is not improved compared to a conventional widefield microscope. However, by replacing the pinhole with a camera, each pixel can act as a very small pinhole without losing any light. Recording an image with the camera at each scan position can be used to construct a superresolved image, increasing

signal level and contrast. This idea has been theoretically described by Sheppard [62, 63] in 1988 and first implemented by Müller and Enderlein in 2010 under the name of Image Scanning Microscopy (ISM) [64]. In this implementation, the point detector of a confocal microscope is replaced by a camera. At each scan position, one camera frame is read out which limits the acquisition speed. A straightforward way to speed up the acquisition is to parallelize it using several scanning beams.

As the CSD can be seen as a parallelized confocal microscope, the CSDISM can be seen as a parallel image scanning microscope. The scanning is achieved by using stroboscopic illumination where the duration of illumination is so short that the rotating disk can be considered stationary. The image recorded by the camera is then the product of the sample modulated with the pinhole pattern of the disk. By successively recording images at slightly different disk positions until the disk is in its initial position again, the whole sample is scanned. Figure 3.1 shows an overview of the technique. An implementation of the CSDISM was first realized by our colleagues Schulz et al. in 2013 [56].

Apart from the CSDISM, a few other implementations of a parallelized ISM have been realized. York et al. developed a multi-point scanning system termed “Multifocal SIM” [65] due to its close relation to structured illumination microscopy (SIM) [66]. The multifocal SIM system is based on a widefield microscope with scanning beams generated by a digital micromirror device (DMD). Because it parallelizes the acquisition of scan positions, it offers an improved temporal resolution but loses the sectioning ability of confocal systems. Software pinholing can be introduced to suppress out-of-focus light, but will not work in thick samples. York et al. also developed “instant SIM” [67] which is even faster: A microlens array produces the multi focus excitation, a pinhole array rejects out-of-focus light, and a second microlens array images the pinholes onto the camera with a demagnification factor of 2. The whole image is scanned by means of a galvo mirror. The $2\times$ demagnification obviates the need for post-processing, and the ISM image can be directly read from the camera. This allows for very high speeds up to 100 Hz but comes at the cost of high complexity in construction and maintenance. The idea to optically process the ISM image was also published around the same time for a confocal microscope by Roth et al., termed optical photon reassignment (OPRA) [68]. Here, a scan unit scans the excitation beam through the sample. The fluorescence light is separated from the excitation by a dichroic mirror and passed through a pinhole after descanning. Then, the beam is magnified $2\times$ via a telescope lens system and again scanned by the same scan unit and imaged on a camera. Around the same time, another optical processing method called re-scan confocal microscopy was proposed by De Luca et al. [69]. The re-scan microscope uses a second, synchronized scan unit to transfer

the beam onto a camera with twice the scan angle which results in a $2\times$ demagnification. Both methods produce an ISM image directly on the camera without further processing. By using a 2-photon laser, Gregor et al. demonstrated that the pinhole can be omitted, obviating the need to scan the beam twice [70].

Optical processing was also realized in a spinning disk by adding a second microlens array to the pinhole disk [71]. This allows very fast acquisition speed in a low maintenance system. Instead of pinholes, also lines have been used similar to the sinusoidal illumination in classical SIM [72]. A review of implementations can be found in Ref. [73].

Here, the aim was to construct and operate a CSDISM setup that can be used as an upgrade kit to add a superresolution option to existing CSD systems. To this end, we developed a plugin for the microscope control software μ Manager, enabling CSDISM imaging in one click, and a program for reconstruction of the ISM image. We investigated the performance of the setup and the ISM image reconstruction.

3.2 THEORY

The increase in resolution and contrast of the CSDISM technique is based on image scanning microscopy (ISM). This technique enables the same resolution as an ideal confocal microscope with infinitely small pinhole as explained in the last Section 3.1. Here, we will give a brief theoretical description and then focus on the image reconstruction for CSDISM.

3.2.1 *ISM Theory*

Müller and Enderlein describe ISM in terms of structured illumination microscopy (SIM). In SIM, a sinusoidal illumination pattern modulates the intensity of the recorded image. The optical transfer function (OTF) of the patterned illumination is mixed with the detection OTF, shifting high spatial frequencies into the range of the detection OTF. The illumination pattern usually has a spatial frequency close to the cutoff frequency of the detection OTF, i.e. the maximum spatial frequency moved into the supported region of the detection OTF is doubled. The same holds true for ISM, only there the illumination pattern is the PSF itself, containing all spatial frequencies up to the cutoff. It can be shown that

$$\text{OTF}_{\text{ISM}}(\boldsymbol{q}) \approx \text{OTF}_{\text{WF}}^2\left(\frac{\boldsymbol{q}}{2}\right), \quad (3.1)$$

where $\text{OTF}_{\text{WF}}(\boldsymbol{q})$ is the OTF of a widefield microscope [56]. The dependence on $\frac{\boldsymbol{q}}{2}$ illustrates the twice higher cutoff of the spatial frequency and is the reason we expect an increase in resolution by a factor of 2. But because the OTF is squared, the amplitude distribution is different, i.e. higher spatial frequencies are more damped.

The result in Eq. (3.1) can be directly translated in terms of the point spread function (PSF), since the PSF is the Fourier transform of the OTF. The Fourier transform of Eq.(3.1) is

$$\text{PSF}_{\text{ISM}}(\boldsymbol{r}) \approx \text{PSF}_{\text{WF}}(2\boldsymbol{r}) \otimes \text{PSF}_{\text{WF}}(2\boldsymbol{r}), \quad (3.2)$$

where the symbol \otimes denotes convolution. Assuming a Gaussian PSF with a width σ_{WF} , the ISM width is $\sigma_{\text{ISM}} = \sigma_{\text{WF}}/\sqrt{2}$. This is the reason that the increase in resolution is not higher than 41 % when measured by the full width at half maximum (FWHM) of the PSF. A deconvolution or reweighting of the amplitudes of the OTF can recover higher spatial frequencies depending on the noise level and further increase the resolution [56].

3.2.2 *Image Reconstruction*

A standard confocal image in the CSD is generated by exposing the camera during the rotation of the disk. Within 1/12 of a full rotation

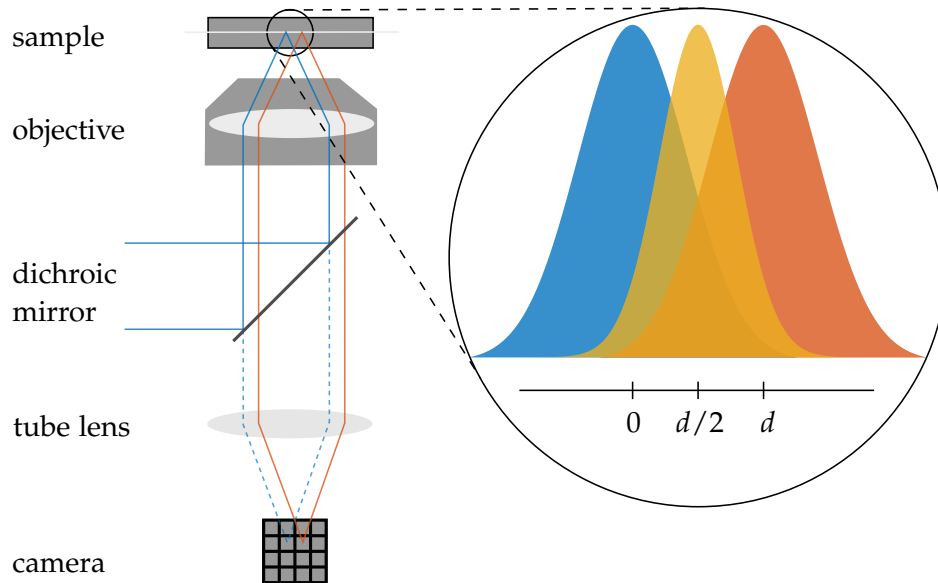


Figure 3.2: Principle of ISM. Excitation light (blue) is focused in the sample. Emission light (red) passes the dichroic mirror and is detected by the camera at pixel position d . The dotted blue line indicates the position of the excitation PSF with respect to the camera. The corresponding excitation and detection PSFs are shown on the right. The product of these is the effective PSF shown in yellow. Its maximum is at $d/2$ which corresponds to the most likely origin of light detected in pixel d . Reassigning the light to the most probable position yields the superresolved ISM image.

of the disk, a full scan is obtained which we will call a cycle. Usually, a CSD image is averaged over many cycles by adjusting the exposure time of the camera to an integer multiple of the duration of one cycle. If this condition is not met, the image is unevenly illuminated and may show stripe artifacts. Especially for small exposure times it is necessary to synchronize the camera to the spinning disk [59]. In the case of CSDISM, scan images are not averaged during the exposure, but instead the excitation light only illuminates the sample stroboscopically, i.e. for a fraction of a cycle when the disk is at a certain position. Several images with shifted disk positions are acquired by this procedure. This set of raw data we will call the CSDISM movie. The sum of this movie recovers the standard CSD image (except for read-out noise).

A superresolved ISM image can be obtained by using the ISM reconstruction method as described by Müller and Enderlein [64] and Sheppard, Mehta, and Heintzmann (“Sheppard sum”) [74]. The image of a diffraction limited spot is a mixture of light from different positions and different angles. We describe this in terms of the PSF on the imaging system. Let us consider the excitation PSF and the detection PSF of one camera pixel. The effective PSF is then the prod-

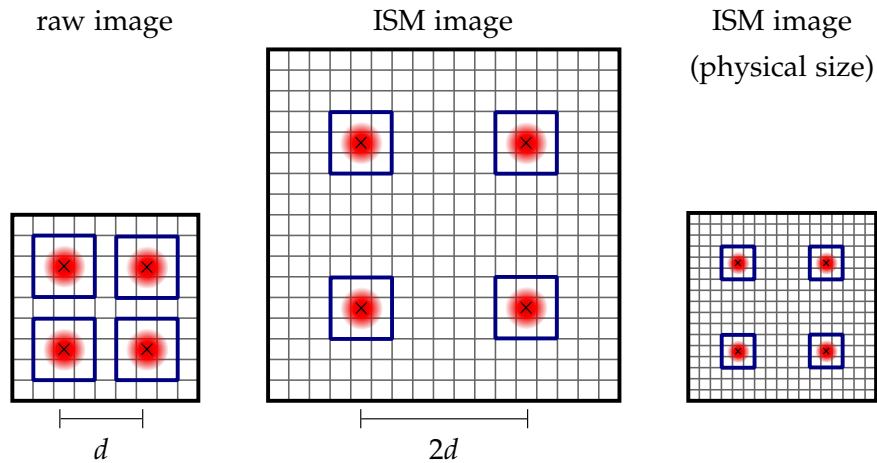


Figure 3.3: ISM image reconstruction algorithm. The bright spots (red) in the raw image are cropped at the reference positions (marked by x). The cropping window (blue rectangles) are centered around the reference positions and copied to the ISM image (middle) with twice the (pixel) distance between the reference position. The physical dimensions of the image are unchanged, resulting in a shrinking of the spot by a factor of 2.

uct of the two. The PSF of a confocal excitation spot is a diffraction limited spot which can be approximated by a Gaussian function. Vice versa, because a camera pixel is imaged as a diffraction limited object into the sample plane, the detection PSF has approximately the same shape. Assuming the excitation PSF at position zero and a detection PSF that is shifted by some distance d , the effective PSF is located at $d/2$. Thus, detecting a photon at position d most probably was emitted at position $d/2$, see also Fig. 3.2. By reassigning the light detected at d to $d/2$, the ISM image is constructed. Mathematically, this corresponds to a shrinkage of the light spots by a factor of two. The reconstruction of a CSDISM movie can be implemented on a computer in an efficient way by the following algorithm:

1. Initialize an empty image with twice the size as the raw image.
2. Crop a spot in the raw data at reference position r (measured in pixels).
3. Place the spot at position $2r$ in the new image.
4. Repeat for all spots.
5. Repeat for all raw image in the CSDISM movie.
6. Sum up all new frames.

Thereby, the distance between spots is doubled which is equivalent to shrinking the spots by a factor of 2, see Fig. 3.3 for a graphical explanation. Here, the reference position corresponds to the position of the excitation PSF on the camera and has to be determined before reconstruction as described in Section 3.4.2.

In the above algorithm the pixel values can only be placed with the accuracy of one pixel. Since the PSF size is on the order of a few pixels only, the positioning accuracy is limited. Thus, the raw images are usually upsampled by a scaling factor M before applying the algorithm. This allows an M -times higher position accuracy which is crucial for a reconstruction without artifacts as we will see in Section 3.4.3.

3.3 METHODS

3.3.1 Setup

The setup is based on a Yokogawa CSU-X1 (M1N-E) connected to the side port of an Olympus IX71 microscope. The microscope is equipped with a PIFOC objective scanner (P-725.2CD, Physik Instrumente) and controller (E-709.CRG, Physik Instrumente). The dichroic mirror in the spinning-disk unit was replaced by a custom made quad line beam splitter (zt405/473/556/640tpc, AHF) to match the laser lines. Four lasers (638L-11A Matchbox 2, Integrated Optics; MGL-N-556/500, MBL-FN-473, and MDL-III-405, all CNI Laser, China) were combined by dichroic mirrors (LaserMUX 375-405R, LaserMUX 561-594R, and LaserMUX 473-491R, all AHF) and guided into the AOTF (AOTFnC-400.650-TN with driver AA.MDS4C-B65-22-74.158, AA Optoelectronic). The first diffraction maximum was coupled into a single mode fiber (SMC-E-400Si-2.6-NA012-3-APC.EC, Schäfter and Kirchhoff) with a fiber coupler (6oSMS-1-4-RGBV11-47, Schäfter and Kirchhoff) and connected to the CSU. The camera used for the measurements was either an Andor iXon 888 Ultra (Andor) or an ORCA-Flash 4.0 sCMOS (Hamamatsu). For some measurements, a quad-band emission filter (BrightLine HC 446/523/600/677, Semrock) was used. The microscope was controlled by a PC (Windows 10 x64, Intel Core i5-4590, 16 GB RAM) with an FPGA board (NI PCIe-7842R, National Instruments) using μ Manager (version 1.4). The triggering signals from the connector block (SCB-68A with SHC68-68-RMIO cable) were connected to the camera, the AOTF driver, and to the control unit of the CSU (CSUX1CU, Yokogawa). The setup with its connections is shown in Fig. 3.4.

The CSU provides an additional $1.2\times$ magnification, so the pixel sizes of the cameras were 108 nm for the EMCCD and 54 nm for the sCMOS with a $100\times$ objective which ensured Nyquist sampling.

The trigger signal for the camera was a TTL signal with HIGH indicating to start the exposure until the signal was LOW again. The time until the next HIGH was used for read-out (about 4 cycles for the ORCA Flash and up to 40 cycles for the Andor EMCCD camera, configured via the μ Manager control plugin). In order for the camera to comply with these specifications, the trigger mode of the cameras was set as following: for the Andor camera, the trigger setting was set to *external exposure*, and for the ORCA Flash, the *trigger source* was set to *external*, the *trigger active* property to *level*, and the *trigger polarity* to *positive*.

3.3.2 Software

The CSDISM setup was controlled with the μ Manager [57] software. A custom written plugin by *Shun Qin* allowed the recording of CS-

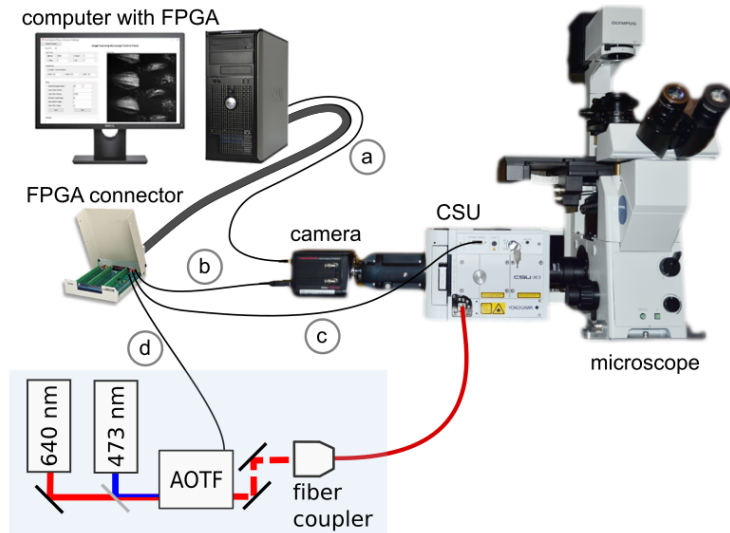


Figure 3.4: The CSDISM setup. A personal computer runs μ Manager with a custom CSDISM plugin which controls the camera (a). The FPGA computes the disk position of the confocal spinning disk unit (CSU) from the CSU's trigger signal (c) and controls the camera (b) and the AOTF (d).¹

DISM movies and also z-stacks of CSDISM movies. The plugin allowed to control several parameters (typical values in brackets): the number of frames for a CSDISM movie (100 – 500), the number of averaging cycles per frame (1 – 100), the number of laser pulses per cycle (4 – 8), the illumination time in a pulse (6 μ s), and a delay for the camera read-out (4 – 40 cycles).

The image reconstruction was performed with custom written *Matlab* scripts and a Java program written by *Shun Qin*.

¹ The picture of the microscope with camera and CSU was taken by *Shun Qin*. The pictures of the FPGA connector and the computer were taken from the National Instruments website and the DELL website, respectively.

3.4 RESULTS

The CSDISM image acquisition involves two steps: the data acquisition of a stroboscopically illuminated CSDISM movie and the reconstruction of the superresolved image (see Section 3.2.2). The illumination time of the laser is limited by the rotation speed: a too long illumination would smear out the foci. We used an illumination time of $6\ \mu\text{s}$ for a disk rotation speed of 1800 rpm. $6\ \mu\text{s}$ is usually too short to acquire sufficient fluorescence signal from most samples, so we usually average over several illumination periods. The position of the disk has thus to be known with sufficient precision so that the disk can be illuminated repeatedly at the same microlens position. We investigate the trigger signal of the disk which corresponds to its position in Section 3.4.1. For the image reconstruction it is vital to know the position of the foci. We outline the procedure to take a reference measurement in Section 3.4.2. Because most artifacts can already (and best) be seen in the reference movie, we give a few examples in Section 3.4.3. We finally illustrate the power of the CSDISM method on three examples: fluorescent beads, a structured fluorescent slide with known pattern, and multi-color 3D imaging of fixed cells.

3.4.1 *Spinning Disk Trigger Signal*

The trigger signal from the spinning disk control unit was measured with an event timer (HydraHarp 400, PicoQuant). On the spinning disk, the pattern for one full scan is repeated 12 times, so that a full rotation corresponds to 12 full scans. For each full scan a trigger signal is given, and a full rotation is marked by a longer duration of the trigger signal. At a set rotation speed of 1,800 rpm, the time between trigger events was 2.78 ms as expected. The standard deviation of the measurement was $< 0.1\ \mu\text{s}$ for all 12 trigger positions. Since each scan pattern had its own trigger signal, we could measure the time to the next trigger and average over full rotations. The result is displayed in Fig. 3.5a. We expected no difference between the scan patterns, but we found a sinusoidal pattern that is well visible at 5,000 rpm (Fig. 3.5b). The observed pattern could be due to a mechanical imbalance of the disk. In this case, the rotation velocity would not be uniform which would shift the pinhole position for repeated illuminations, resulting in a blurring of the recorded spots. However, the maximum deviation from the mean value was $0.17\ \mu\text{s}$ and thus much smaller than the usual illumination time of $6\ \mu\text{s}$ or the 2.78 ms of a full scan. Assuming a pinhole pitch of $250\ \mu\text{m}$ as given by the manufacturer, the maximum shift of the pinhole position was less than 20 nm which is much smaller than the size of the pinholes of $50\ \mu\text{m}$. We therefore neglected this effect and assumed a constant rotation velocity. This allowed us to estimate the duration of the next scan period from the last as implemented in our software for the FPGA.

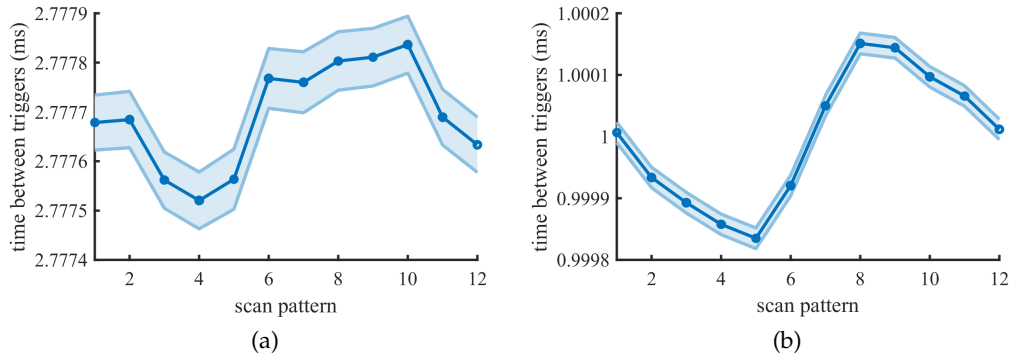


Figure 3.5: Trigger signal timing. The time between successive trigger signals was measured for each of the twelve scan patterns at a) 1,800 rpm and b) 5,000 rpm. The shape of the curve is probably due to a slight mechanical imbalance of the disk, well visible at high speed. The overall timing error is about $0.17 \mu\text{s}$.

3.4.2 Reference Measurements

As described in Section 3.2.2, the positions of the excitation PSFs are needed to reconstruct the ISM image. These reference positions were obtained by recording a CSDISM movie of a homogeneous fluorescent sample. Each spot in the raw data then corresponded to the position of a pinhole. Localization of the center of the spots gave a sub-pixel precise position of the pinhole. Because the excitation light is focused through the pinholes, we did not distinguish between the pinhole position and the position of the excitation PSF and use these synonymously, or refer to it simply as the *reference position*.

A drop of homogeneous dye solution (e.g. $1 \mu\text{M}$ Atto 655 in water) on a cover slip sufficed for a measurement of the reference positions. An example is shown in Fig. 3.6. Alternatively, autofluorescent plastic slides (92001, Chroma) can be used.

In SIM, the illumination pattern is often estimated from the raw data. If the SNR of the raw data is low, the estimation can be erroneous and introduce artifacts in the reconstruction. Here, we chose a calibration approach to circumvent this problem. This introduces an additional step to the measurement, but it only needs to be repeated in case of changes in the optical path, e.g. exchanging the camera, which are not expected to occur often in a CSD. Unlike SIM, where the pattern crucially depends on the excitation wavelength, the distances between the pinholes do not change. However, we have observed that chromatic aberrations of the setup influence the pattern. In first order approximation, this introduces a global shift of the pattern on the order of a few tens of nanometers. As long as the window size in the reconstruction software is chosen large enough, this will result in a global shift of the reconstructed image only. Thus, a reference measurement in a single color is usually enough to reconstruct

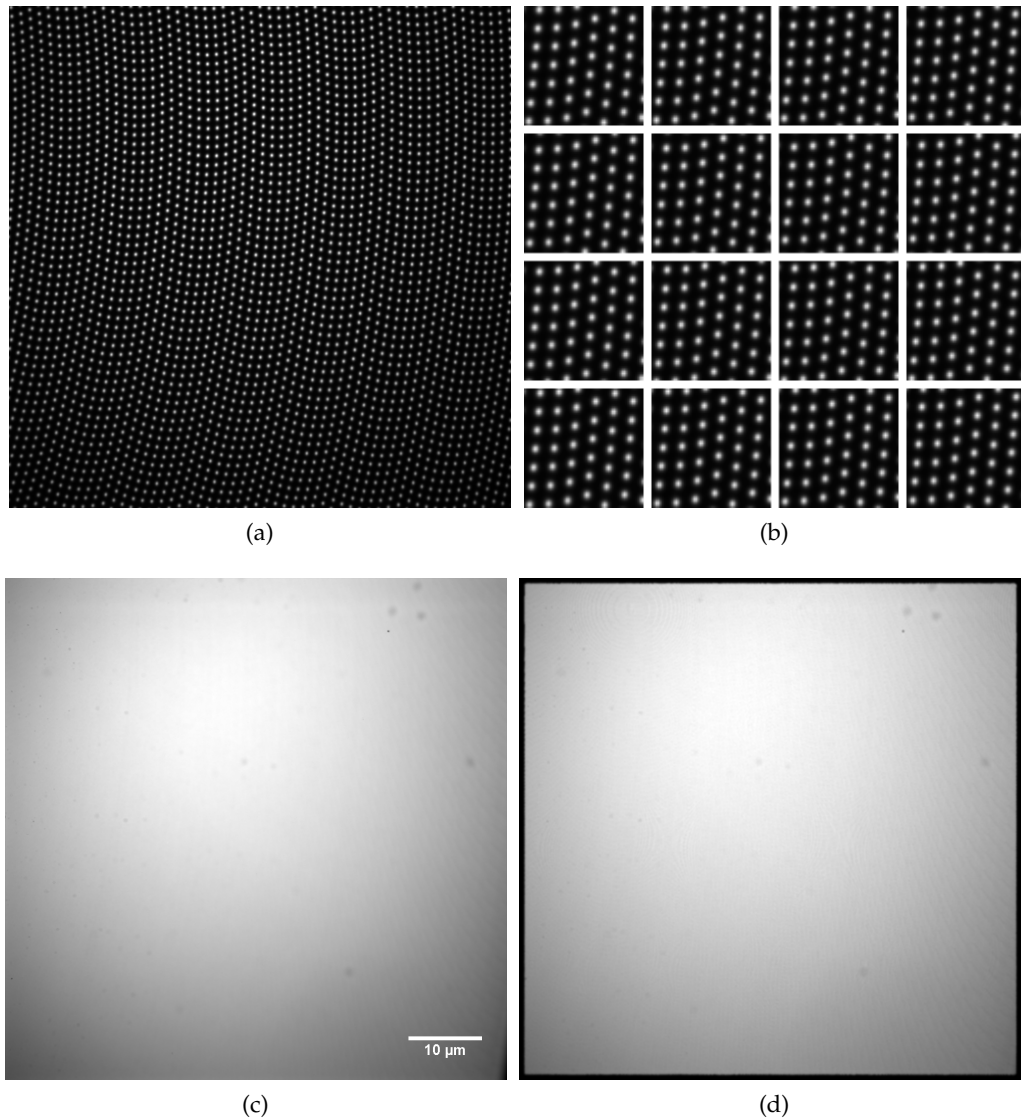


Figure 3.6: Reference measurement with Atto 655 dye solution. a) First frame of the reference movie. b) A small detail of the first 16 frames is shown, ordered from left to right and top to bottom. c) Sum of all frames. The scale bar is valid for all images except b). d) ISM reconstruction with the movie as its own reference. The edges are excluded from the reconstruction and thus appear black. An Andor EMCCD camera was used with the 640 nm laser for excitation. In total, 250 frames were acquired with the 4-pulse sequence averaged over 200 cycles. The total illumination time was 1.2 ms per frame. All images are min-max scaled.

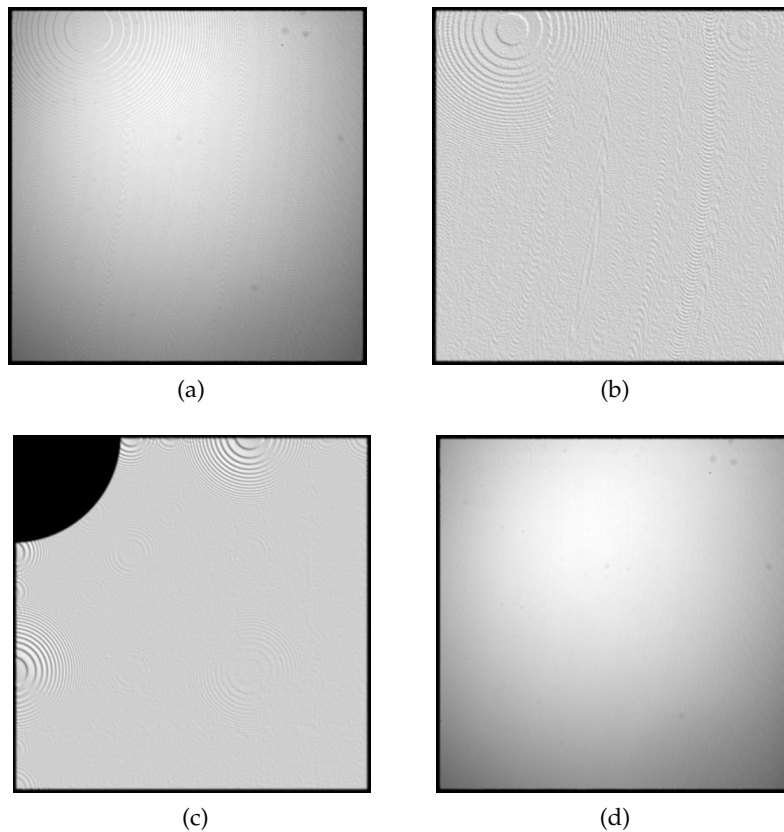


Figure 3.7: Reconstruction artifacts for a homogeneous sample. a) ISM reconstruction of the reference movie shown in Fig. 3.6 but with an upscaling factor of 2 instead of 8. Reconstruction artifacts are visible as periodic structures and rings. b) Artificial reconstruction from the position data of Fig. 3.6. A normalized Gaussian is placed at each position with the width set to 1.26 pixels as estimated from the raw data. c) Artificial reconstruction as in b) but from simulated pinhole positions. The top left corner corresponds to the center of the disk. d) ISM reconstruction with appropriate settings (same as in Fig. 3.6d, shown here for comparison).

images in any color as long as no correlative measurements are performed that require higher accuracies.

3.4.3 Image Artifacts

Sometimes, image artifacts were seen in the reconstructed images. One example is shown in Fig. 3.7a for the reconstruction of a reference movie. We would expect a homogeneous intensity as in Fig. 3.6, but instead there are concentric rings visible in the top left corner. The source of the artifact can be found either in the hardware, the reconstruction software, or in the acquisition process.

The most common encountered artifact is the appearance of stripes in the ISM image. This is often due to non-constant signal intensity caused by fluctuating excitation power or sample bleaching. The laser

power itself can fluctuate, for example because of insufficient temperature stability, low quality drivers, or a reflection causing a feedback in the cavity. The fiber coupling can act as an unwanted vibration sensor because any mechanical vibration will translate into fluctuating power if the coupler is not well aligned. With optimal coupling on a damped table the changes are usually negligible. If the fluctuation is on a similar timescale as the CSDISM image acquisition, the fluctuation will be visible as stripes of higher and lower intensity. This artifact is also visible in the sum image and can thus be easily identified. If the artifact is not visible in the sum image but only in the ISM image, there are several possibilities:

- The *reconstruction parameters*, especially the scaling factor, are chosen incorrectly. The scaling factor M determines the upsampling of the final image and is important to place the spots at the reference position with sub-pixel precision. The image is upsampled by $2M$ and later rescaled by $1/M$, so that the ISM image has twice the size of the original image. For our setup, we found an upscaling factor of 8 to be sufficient and used it for all reconstruction images, for example in Fig. 3.6. This scaling factor corresponds roughly to a precision of $\sigma_{\text{PSF}}/5 \approx 30$ nm. An example of the ISM image of an insufficient scaling factor can be seen in Fig. 3.7a.
- Because of a *low SNR* of the reference movie, the fit quality of the position estimate will suffer. Because this determines how accurate the reference positions can be estimated it can lead to an incorrect reconstruction. For example, using an inaccurate local maximum finder produces artifacts very similar to Fig. 3.7a.
- *Insufficient sampling*, i.e. too few frames, will also result in stripe artifacts. Then, parts of the image have a lower intensity, resulting in regular patterns. For a very low number of frames (e.g. 120 images), this can already be seen in the sum image.

In addition to the above mentioned scaling factor, we also found that the scaling method influences the final image quality. We tested three different methods for up- and downscaling: nearest-neighbor (NN) interpolation, linear interpolation, and Fourier interpolation. The NN method simply copies the value of the nearest pixel during upscaling and sums the pixel values to a superpixel for downscaling and was used in Ref. [56]. The linear interpolation uses a triangular kernel to interpolate pixel values in a 2×2 pixel neighborhood. Here, we used Matlab's `imresize` function with the 'bilinear' option. In Fourier interpolation, the image is Fourier transformed and then zero padded or cropped to the desired size. The inverse Fourier transform then corresponds to an interpolated version of the initial image and is optimal in the sense that the frequency content of the image is unchanged (i.e. the OTF is not altered). Here, we used a Matlab implementation by

my colleague *Simon Stein*. We found that linear interpolation showed less artifacts than nearest-neighbor or Fourier interpolation.

In the CSDISM reconstruction of the reference movie (Fig. 3.6) we used the position and intensity from the same file. To eliminate the effect of instrumental artifacts such as inhomogeneous illumination, varying excitation power, or bleaching artifacts, we created an *artificial* ISM image: Normalized Gaussians were placed at each reference position from the measured sample in an otherwise empty image and summed up. Thus, only the position information was used to exclude that the artifacts stem from the intensity or shape of the PSF in the reference movie. The image obtained in this way corresponds to an ideal homogeneous sample, excited with a uniform light source, and imaged with a Gaussian PSF. This image (Fig. 3.7b) shows the same reconstruction artifacts as before which means that the artifacts are inherent in the scan pattern.

The above described artificial reconstruction excludes the influence of an inhomogeneous intensity. To exclude that there is still an influence of the positions, for example by the fitting process, we simulate an artificial pinhole pattern of the CSD based on the description of the pinhole positions in Ref. [59]. In polar coordinates (r, θ) , the position of the n^{th} pinhole is given by

$$\begin{aligned} r_n &= r_0 + \frac{ma}{2\pi}\theta_n \\ \theta_n &= \frac{2\pi}{ma} \left[\left(r_0^2 + \frac{nma^2}{\pi} \right)^{\frac{1}{2}} - r_0 \right], \end{aligned} \quad (3.3)$$

where a is the pinhole pitch, m the number of spirals, and r_0 the innermost radius. We estimate the pinhole pitch from our data, set the number of spirals to 1, and sample one quadrant of the disk. The scanning is simulated by rotating the whole pattern. We place Gaussians at the sampled pinhole positions as before and obtain a pattern shown in Fig. 3.7c. The concentric ring pattern looks similar to the ones found experimentally. Therefore, we conclude that these artifacts are inherent in the scan pattern and cannot be completely avoided. Note that the artifacts appear even stronger than in the best experimental reconstruction (Fig. 3.6). This is due to a constant offset in the raw images which decreases the contrast of the concentric ring artifact.

3.4.4 Example 1: Fluorescent Beads

Fluorescent beads with a diameter of 100 nm (TetraSpeck, Invitrogen) were spin coated on a glass cover slip. The CSDISM image is shown in Fig. 3.8. The sum image was upsampled by linear interpolation to match the image size of the ISM image. In both images, individual beads were located by global thresholding the ISM image and then using Matlab's inbuilt `regionprops` function for candidate detection.

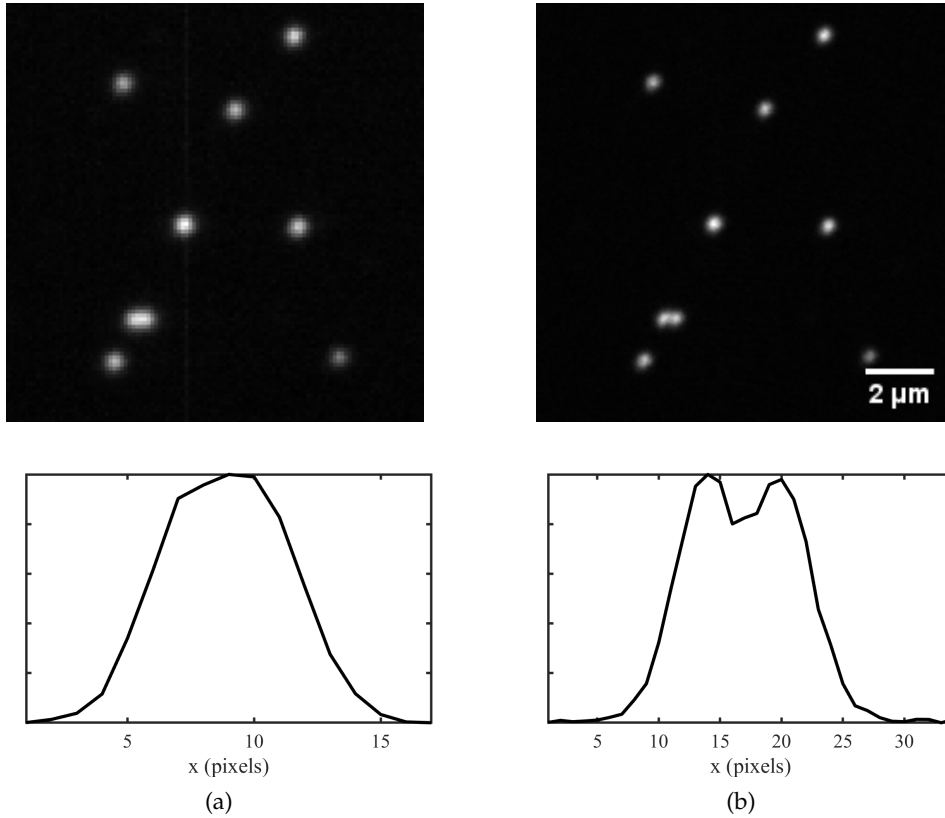


Figure 3.8: CSDISM example 1. Image of spin-coated fluorescent beads. Top row: a) Sum image and b) ISM image. Bottom row: line plot through the cluster in the left lower corner of the image. The position of the two particles can be distinguished in the ISM image. For this image, the Andor 888 Ultra EMCCD camera was used with a 640 nm laser for excitation. 250 frames were acquired with the 4-pulse sequence averaged over 60 cycles.

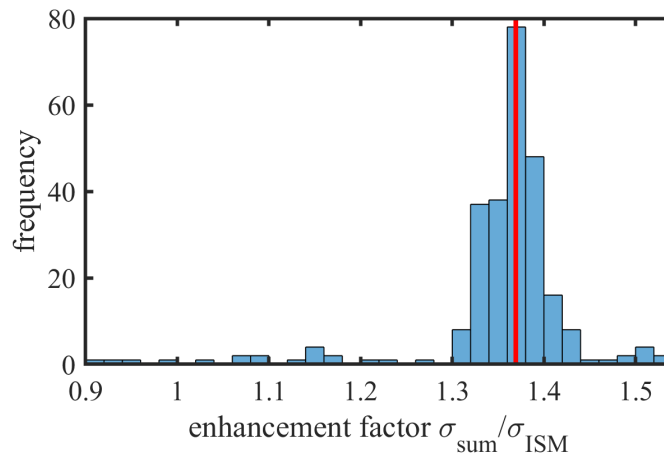


Figure 3.9: Resolution enhancement factor measured with beads. Each bead in the image was fitted by a 2D Gaussian. The width σ is a measure of resolution of the system. The ratio of the widths in the sum image to the width in the ISM image gives the resolution enhancement by ISM. The experimentally obtained average of 1.36 is close to the theoretically expected value of $\sqrt{2} \approx 1.41$ and in agreement with Ref. [56].

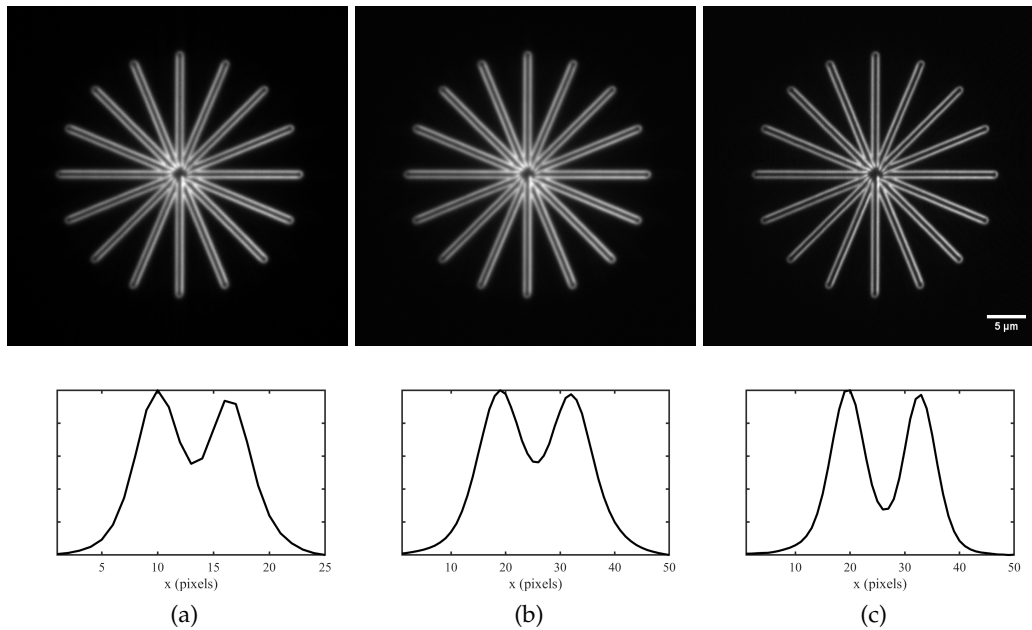


Figure 3.10: CSDISM example 2. Fluorescent star structure on the Argo-SIM slide. Top row: a) CSD image with 100 ms exposure time. b) Sum image of the CSDISM raw data. c) CSDISM image. Bottom row: line sections through the northern arm of the star. This image was acquired using the Orca Flash camera with 2×2 binning and the 4-pulse sequence for 250 images averaged over 50 cycles.

A 2D Gaussian with constant offset was then fitted to a small area around each detected spot. The width of the Gaussian σ is directly related to the FWHM and shown in Fig. 3.9. The resolution improvement factor (as measured by the FWHM) is thus $\frac{\sigma_{\text{sum}}}{\sigma_{\text{ISM}}}$. We find an average resolution improvement of 36 %, close to the theoretically expected 41 % (cf. Section 3.2.1).

3.4.5 Example 2: Argo-SIM Fluorescent Slide

The Argo-SIM slide (Argolight) is a solid state fluorescent sample that is designed for calibration and performance monitoring of SIM microscopes. It comes with a variety of different patterns of which we show one example in Fig. 3.10. There is no difference between the standard CSD and the sum image, especially for the line sections. In the ISM image however, the lines are better separated, demonstrating the improved resolution.

3.4.6 Example 3: 3D Multi-Color Imaging of Fixed Cells

CSDISM can be extended to 3D and multi-color imaging exactly as for a normal CSD setup. Because of the sectioning capability of the spinning disk, z-stacks can be recorded with the help of an objective or sample scanner. This is supported by the μ Manager plugin that is able to control any z-stage compatible with μ Manager. Multiple color channels can be recorded sequentially, and the AOTF can be used to easily switch between the colors. Because of the sequential recording, acquiring a 3D multi-color image is time consuming. A single ISM image in Fig. 3.12 takes about 40 s, thus the recording of the z stack with 12 slices in three colors takes at least 24 minutes, not counting filter changes. By decreasing the number of frames or the number of averaging cycles and increasing the pulse sequence, the imaging speed can be increased. Frame rates up to 1 Hz have been demonstrated [56].

In Fig. 3.11, we show a multi-color CSDISM image of a fixed cell from the *vero* cell line. For comparison, also the sum image of the CSDISM movie is shown which corresponds to the conventional CSD image. A z-stack of another cell is shown in Fig. 3.12. The z-stack can be used to reconstruct a 3D image of which we show a YZ section in Fig. 3.12b. The sample preparation procedure is described below.

IMMUNOSTAINING OF CELLS Vero cells, grown on cover slips for 48 h, were fixed in 4 % paraformaldehyde in PBS for 15 minutes, permeabilized with 0.5 % Triton X-100 in PBS for 10 minutes and blocked with 3 % (w/v) BSA-PBS for 30 minutes at room temperature. Then, cells were incubated with mouse monoclonal anti- α -tubulin antibody (T6199, Sigma-Aldrich) diluted at 1:200 in 3% (w/v) BSA-PBS containing 0.005 % Triton-X 100 for one hour. Subsequently, the cells were rinsed three times in PBS for 10 minutes each, followed by a 1 h incubation with FITC-conjugated goat anti-mouse IgG (F0257, Sigma-Aldrich) together with Atto 550-phalloidin (AttoTec) diluted in 3% (w/v) BSA-PBS containing 0.005 % Triton X-100. After immunostaining, cells were rinsed three times in PBS for 10 minutes each and one time with distilled water and samples were mounted using Fluoroshield with DAPI (F6057, Sigma-Aldrich). The samples were prepared by *Eugenia Butkevich*.

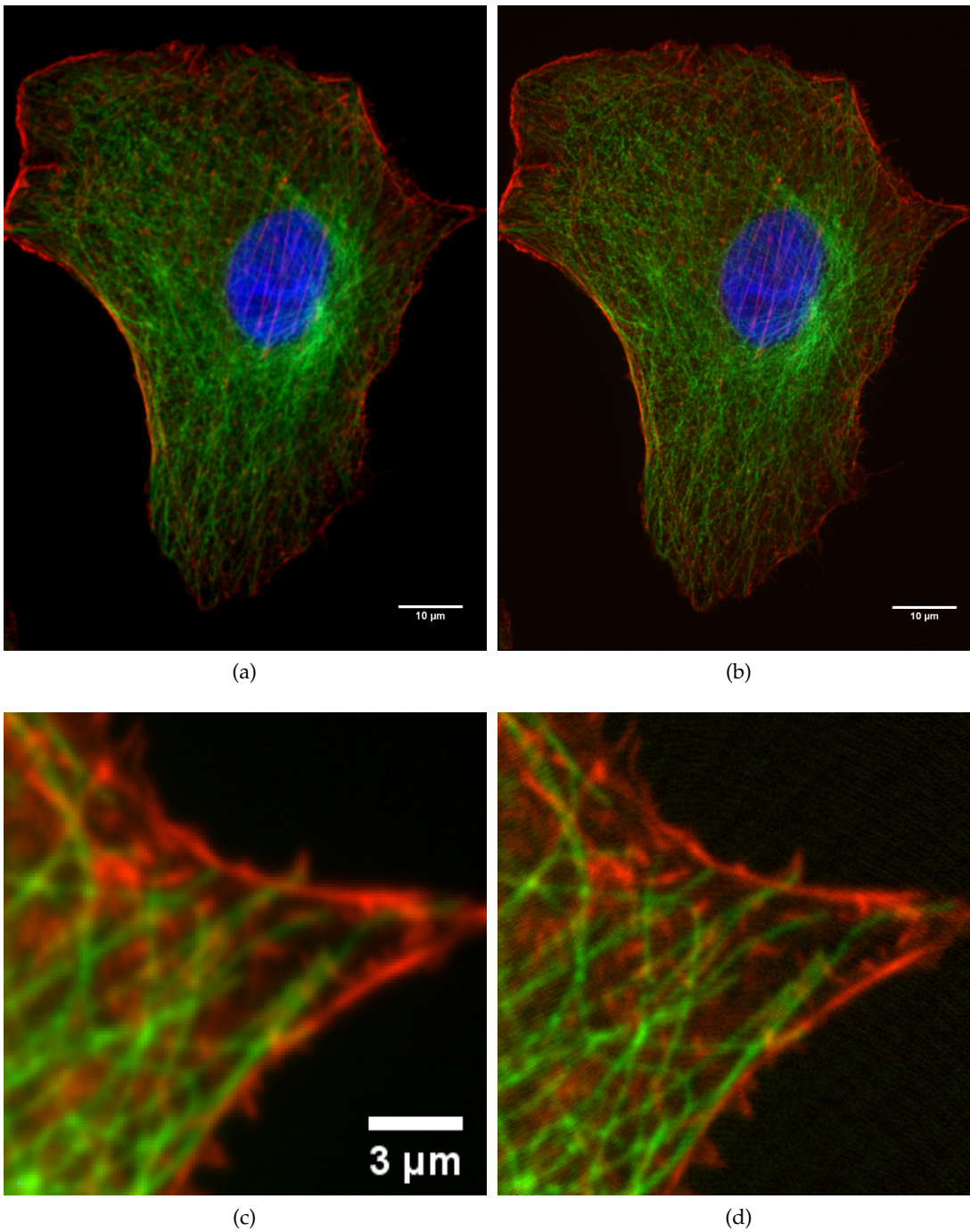


Figure 3.11: CSDISM example 3. Multi-color CSDISM image of a fixed cell from the *vero* cell line. The sum images of the raw data are on the left side and the ISM images on the right side. The top row shows the complete field of view and the bottom row a zoomed-in region (the thresholds of the color channels were separately adapted for these images). The colors correspond to: blue – nucleus (DAPI), green – tubulin (FITC- α -tub), and red – actin (Atto 550-phalloidin). This image was acquired using the Orca Flash 4.0 with 2×2 binning and the 4-pulse sequence for 250 images averaged over 30 cycles in each channel.

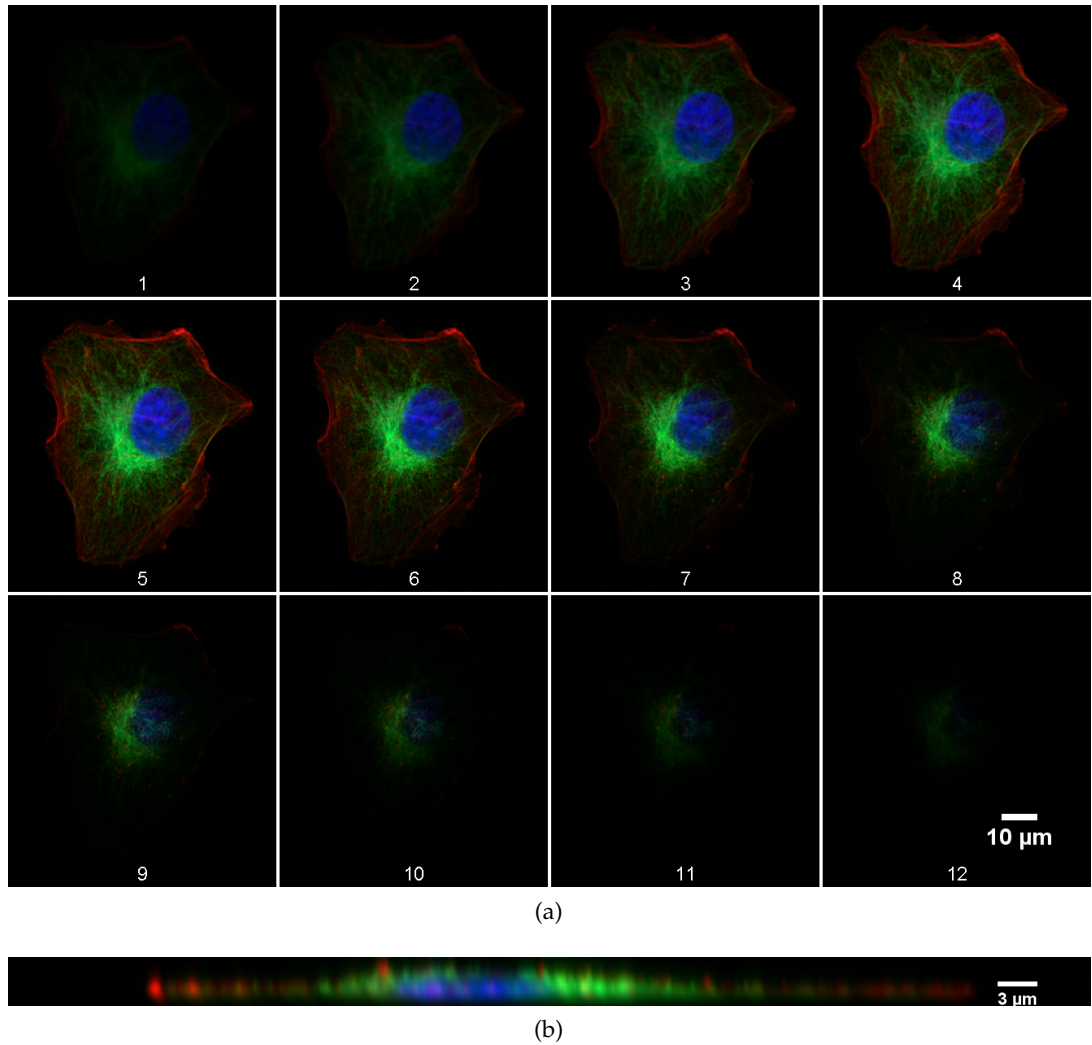


Figure 3.12: CSDISM example 3. 3D multi-color CSDISM imaging of a fixed cell. The top images show individual slices with 300 nm distance. The bottom image is a YZ section through the center of the image. The staining of the cell is the same as in Fig. 3.11. The image was acquired using the Orca Flash camera and a 60 \times water immersion objective (UPLSAPO 1.2 NA, Olympus).

3.5 DISCUSSION

A standard CSD setup was upgraded with a superresolution option for 3D multi-color imaging. We investigated the performance of the setup and identified possible artifacts in the ISM image reconstruction.

For CSDISM, the CSD setup is extended by a stroboscopic illumination which requires precise timing of the illumination with respect to the CSD rotation. We checked the accuracy of the CSD trigger signal for the disk rotation and found the timing jitter to be at most $0.17\ \mu\text{s}$ which corresponds to a shift of the position of less than 20 nm. This allows the estimation of the next scan period from the last to accurately predict the pinhole positions for the repeated stroboscopic illumination. The function of the assembled CSDISM system was demonstrated in three different examples including a sparse bead sample, a solid state fluorescent resolution target, and 3D multi-color imaging of fixed cells. With the bead sample, a resolution improvement of 36 % was demonstrated which is close to the theoretically expected maximum of 41 %. The cell images show the 3D capability of the system and the possibility to acquire three colors sequentially.

The superresolution of CSDISM is based on ISM image reconstruction of a movie of the sample with stroboscopic illumination. Typical artifacts which were observed in the reconstructed images were studied and possible sources revealed. The reference image, i.e. the CSDISM image of the reference movie, was found to be a good indicator for image artifacts. It allows to determine whether the source of the artifacts could be found in the hardware (fluctuating excitation power), the acquisition process (low signal or suboptimal imaging parameters), or in the reconstruction software (reconstruction parameters or method of localization).

The CSDISM is one of many methods that apply ISM in parallel for fast superresolution imaging. In terms of resolution, the CSDISM is close the theoretical maximum of ISM [56], thus on the same level with the parallelized ISM systems introduced in Section 3.1. In terms of speed, most of the other systems are actually faster than the CSDISM which is mainly due to its low duty cycle of excitation. Also, the optical reassignment methods do not require post-processing but directly deliver a superresolved image. However, these methods usually require an expensive, custom built setup and are difficult to align and maintain. A notable exception of the complex ISM implementations is the CSD using optical photon reassignment by Azuma and Kei of the Yokogawa company [71]. By adding a second microlens array to the backside of the pinhole disk, a $2\times$ magnification is achieved so that the ISM image is directly built up on the camera. The setup shares the ease-of-use and low maintenance of our CSDISM and additionally provides higher acquisition speed. In contrast to the CSDISM, it needs an additional magnification to ensure Nyquist sampling of

the superresolved image which crops the field of view. In CSDISM, only the raw image needs to be Nyquist sampled and additional up-sampling is only needed during post-processing.

The main advantage of the CSDISM is that any CSD system can be easily upgraded with a superresolution option. The upgrade does not require any changes in the optical path of the microscope since all optical components in the CSD are pre-aligned by the manufacturer. Furthermore, many existing CSD systems already use an AOTF to select the wavelength for excitation. Some lasers allow a fast modulation of the laser intensity, then no AOTF is needed at all. The synchronization of the AOTF or the laser with the CSD can be achieved with our μ Manager plugin and a commercially available FPGA card. Then, the acquisition of an ISM image is a one-click process. Standard CSD systems are widely spread in labs all over the world and we hope that our software will be used to upgrade them with a superresolution option, allowing researchers to look at their samples in new detail.

AXIAL CO-LOCALIZATION OF SINGLE MOLECULES USING METAL-INDUCED ENERGY TRANSFER

In this chapter, we present a new method to measure distances along the optical axis on the nanometer scale. We use single-molecule metal-induced energy transfer (smMIET) with step-wise bleaching to measure intra-molecular axial distances in DNA origami structures. This opens up new possibilities to study the structure of large biomolecules or complexes.

Parts of this chapter have been published in:

Sebastian Isbaner, Narain Karedla, Izabela Kaminska, Daja Ruhlandt, Mario Raab, Johann Bohlen, Alexey Chizhik, Ingo Gregor, Philip Tinnefeld, Jörg Enderlein, and Roman Tsukanov. "Axial Colocalization of Single Molecules with Nanometer Accuracy Using Metal-Induced Energy Transfer." In: Nano Letters 18.4 (Apr. 11, 2018), pp. 2616–2622. DOI: [10.1021/acs.nanolett.8b00425](https://doi.org/10.1021/acs.nanolett.8b00425).

4.1 INTRODUCTION

Distinguishing fluorescent emitters from each other is a prerequisite to resolve structural details in a fluorescent sample. The resolution of an optical microscope is limited by the diffraction of light. The resolution limit defines the closest distance of point emitters in focus so they can be distinguished on a screen or a camera. A first theoretical description was given by Abbe [75] in 1873 as

$$d_{xy} = \frac{\lambda}{2\text{NA}} \quad (4.1)$$

with λ being the emission wavelength and NA the numerical aperture of the objective. For a typical optical microscope, the resolution limit is on the order of 200 nm. A similar argument holds true for the axial resolution

$$d_z = \frac{\lambda}{n(1 - \cos(\theta_{\max}))} \approx \frac{2n\lambda}{\text{NA}^2}, \quad (4.2)$$

where θ_{\max} is half the opening angle of the objective given by $\text{NA} = n \sin(\theta_{\max})$, and is usually several times larger than d_{xy} , on the order of 500 – 800 nm.

Superresolution techniques developed in the past twenty years have pushed the limits of the lateral resolution down to the nanometer regime. Structured illumination microscopy (SIM) uses a diffraction limited excitation pattern which reveals new spatial frequencies in

the sample. Several recorded images are used to reconstruct an image with doubled resolution [66]. Stimulated emission depletion (STED) microscopy and other members of the reversible saturable optical fluorescence transitions (RESOLFT) family use point-spread function (PSF) engineering through optically saturable transitions of the fluorescent labels. The size of the excitation PSF is effectively reduced by an overlapping laser beam with a donut shaped PSF which depletes the fluorescence of molecules [26]. Another class of superresolution techniques is based on the precise localization of spatially well-separated fluorescent molecules. The diffraction limit is bypassed because the center position of a single fluorescent emitter can be localized much more precise than the width of the PSF [25, 76, 77]. To be able to image densely labeled samples, spatial separation is achieved by multiplexing the emission of several emitters in time: In a single camera frame, only a sparse subset of all emitters is fluorescent and can be localized. In subsequent frames, different subsets are fluorescent and the aggregated localizations can then be combined into a superresolved image. The main difference between methods of this class is the mechanism to switch molecules on or off. Stochastic optical reconstruction microscopy (STORM) and its variant direct STORM (dSTORM) use the intrinsic blinking behavior of organic dyes [13, 78]. Photoactivation localization microscopy (PALM) uses photoactivatable molecules that can be switched on by irradiation with UV light [11]. In DNA points accumulation for imaging in nanoscale topography (DNA-PAINT), fluorescently labeled oligonucleotides transiently bind to the structure of interest [79]. All of the superresolution methods above improve the lateral resolution beyond the diffraction limit but do not change the resolution along the optical axis. This limits these methods to very flat objects or poses the difficulty to interpret the images as projections of 3D objects.

Several of the lateral superresolution techniques have been extended to 3D and improved also on the axial resolution. For example, 3D-SIM extends the planar structured illumination pattern to a 3D interference pattern. In 3D-STED, the size of the excitation PSF is reduced along the optical axis by an additional depletion beam. In the localization methods, a common approach is to introduce a cylindrical lens into the emission path which introduces an artificial astigmatism in the PSF, encoding the z-position of the emitter. In biplane imaging, the emission light is split into two focal planes on the camera which hold information on the emitter position [80]. An overview over the lateral and axial resolution of the above mentioned methods can be found in Table 4.1. Although these methods greatly improve on the axial resolution, their axial resolution usually still remains a factor of 2 to 5 worse than their lateral resolution. An exception is the interferometric PALM (iPALM) method that combines localization of photo-switchable proteins with interferometric imaging and achieves a sub-20 nm isotropic resolution [81]. However, this comes at the cost of

| method | lateral resolution | axial resolution | Ref. |
|--------------------|--------------------|------------------|----------------------|
| 3D-SIM | 120 nm | 360 nm | Fiolka et al. [82] |
| 3D STED | 50 nm | 125 nm | Harke et al. [83] |
| astigmatic imaging | 20 nm | 50 nm | Huang et al. [84] |
| biplane imaging | 30 nm | 75 nm | Juette et al. [80] |
| iPALM | < 20 nm | < 10 nm | Shtengel et al. [81] |
| SAF (+ dSTORM) | 20 nm | 20 nm | Bourg et al. [85] |
| vaTIRF | ~ 200 nm | > 10 nm | Olveczky et al. [86] |

Table 4.1: Examples of the lateral and axial resolution of optical microscopy methods. Comprehensive overviews can be found in Refs. [87] and [25].

increased complexity of the system: iPALM detects single molecules with two objectives, interferes their emission in a custom-made 3-way beamsplitter, and images them onto three cameras to reconstruct the height information.

In contrast to the imaging methods discussed above, methods that use a near-field coupling of the emitter have been used for distance measurements as well. When the incidence angle of the excitation light is higher than the critical angle, an evanescent wave along the optical axis is produced which decays exponentially within a few hundreds of nanometers above the coverslip, depending on the angle of incidence. This can be used to selectively excite fluorescence close to the coverslip and is known as total internal reflection fluorescence (TIRF) [88]. Illuminating the sample with light at different incidence angles changes the distance over which the evanescent wave decays and thus the fluorescence intensity. The ratio of the observed fluorescence intensities allows to estimate the distance of an emitter from the surface and is known as variable angle TIRF (vaTIRF) and achieves an axial localization precision on the nanometer scale [86, 89, 90]. A recent implementation showed an axial resolution of 20 nm by using the intensity ratio of two excitation wavelengths in TIRF [91]. Apart from the excitation, also the emission intensity can be used to infer the height of an emitter above the coverslip. In supercritical angle fluorescence (SAF) microscopy, the emission light is split into two channels corresponding to the light emitted above and below the critical angle [92]. Because the angular distribution of radiation of an emitter close to a glass-water interface changes with height, the intensity ratio of the two channels can be used to estimate the emitter height. This method can be used for confocal as well as widefield microscopes to achieve nanometer axial resolution [93, 94]. A recent implementation combined SAF with STORM and achieved an isotropic resolution of 20 nm within a range of 150 nm from the surface [85]. The high axial

localization precision of both the SAF and the vaTIRF families depend on the precise measurement of the fluorescence intensity which suffers from cross-talk and background and thus requires careful calibration.

Another prominent example of the spectroscopic methods for distance measurements is Förster Resonance Energy Transfer (FRET): A fluorescent molecule (the donor) transfers its excited state energy to another fluorescent molecule (the acceptor). Since this process is mediated via dipole-dipole interaction, the rate of the energy transfer depends on the sixth power of the distance r :

$$k_{\text{FRET}} \propto \left(\frac{R_0}{r} \right)^6 \quad (4.3)$$

Here, R_0 is the so-called Förster radius,

$$R_0 = \frac{9 \ln(10)}{128 \pi^5 N_A} \frac{\kappa^2 \text{QY}_D}{n^4} \int d\lambda F_D(\lambda) \epsilon_A(\lambda), \quad (4.4)$$

where N_A is the Avogadro constant, and depends on the mutual orientation of the two dipole emitters κ^2 , the donor's quantum yield QY_D , the refractive index of the medium n , and the overlap integral of the donor's emission spectrum $F_D(\lambda)$ with the acceptor's absorption spectrum $\epsilon_A(\lambda)$ [95]. The value of the Förster radius is typically on the order of 5 nm, limiting the useful range of FRET to distances between 1 to 10 nm. In that range, FRET has been proven very successful to measure intramolecular distances or to study conformational dynamics in biomolecular complexes [19, 96–98].

One particularity of FRET is that it requires double labeling of the molecule of interest which can be tedious to achieve if the yield of one of the dyes' coupling reaction is low. Especially in bulk measurements, incomplete labeling leads to a skewed value of the FRET efficiency because donor-only labeled molecules will show a low FRET efficiency and acceptor-only labeled molecules show a high FRET efficiency due to direct excitation of the acceptor dye. Several techniques have been developed to overcome this limitation, notably alternating laser excitation FRET (ALEX-FRET) [99] and pulsed interleaved excitation (PIE-FRET) [100] which both aim at distinguishing single labeled from double labeled molecules.

To use FRET as a quantitative and accurate ruler, precise knowledge of the Förster radius is essential. All contributing factors in Eq. (4.4) can be measured with standard spectroscopic methods except for the orientation factor κ^2 . This factor depends on the mutual orientation of the labels

$$\kappa^2 = (\cos(\theta_{DA}) - 3 \cos(\theta_D) \cos(\theta_A))^2, \quad (4.5)$$

where the angles between the dipole moments of the two emitters are defined in Figure 4.1. κ^2 is often assumed to be equal to $\frac{2}{3}$ for freely rotating dipoles, but can vary between 0 and 4 for orthogonal and

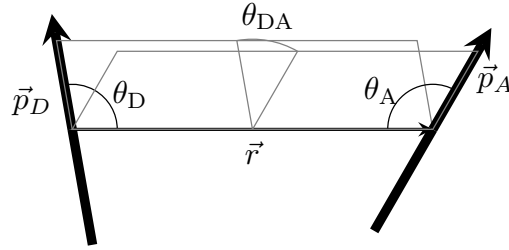


Figure 4.1: Orientation factor in FRET. The emitters are characterized by the emission dipole moment of the donor, \vec{p}_D and the excitation dipole moment of the acceptor, \vec{p}_A , which are separated by a distance r . The angles between the dipole moments and the distance vector r are θ_D and θ_A . θ_{DA} is the angle between the planes spanned by r and the dipole moments.

co-linear dipoles, having a substantial effect on R_0 . But for the case of fixed or partially restricted rotation (e.g. free rotation within a cone), it is not possible to measure all angles in the above equation for κ^2 . Even if the absolute orientations of the dipoles are known, the relative orientation θ_{DA} depends on their relative position in space and thus cannot be measured independently of the distance.

Here, we present metal-induced energy transfer (MIET) as a new approach to measure axial distances in the range of 100 nm with nanometer precision. A dipole emitter close to a metal surface can transfer energy to surface plasmons of the metal. Similar to FRET, the transfer efficiency yields information on the distance of the emitter from the metal surface. But in contrast to FRET, the interaction range between a fluorescent emitter and the metal film is roughly one order of magnitude larger leading to an effective range of about 100 nm. Since the optical absorption spectrum of a metal film is very broad, almost any fluorescent dye within the visual spectral range can be used. The fluorescent lifetime is measured and then converted into an axial distance using a theoretical model [53, 54]. The energy transfer depends on the orientation of the dye, similar to FRET. However, the only relevant angle for MIET is the angle between the emission dipole and the surface normal of the metal film. In contrast to FRET, this angle can be measured by defocused imaging or other techniques in case the dipole is not freely rotating [101–103]. Since only a single position needs to be labeled, MIET also simplifies the sample preparation. No complex instrumentation is needed, because the transfer efficiency can be accurately measured via the fluorescence lifetime. A standard confocal microscope with fluorescent lifetime imaging (FLIM) capability is thus sufficient.

MIET has been first used experimentally in 2014 to map the topography of the basal membrane of fluorescently labeled live cells with about 3 nm axial resolution [104]. The technique has been demonstrated even for single molecules: Karedla et al. performed FLIM on spin-coated single molecules on different spacer thicknesses on top of a gold film and showed that the measured lifetimes agree with

the theoretical model. Furthermore, these single molecule MIET (sm-MIET) experiments reached about the same axial localization accuracy of 3 nm as in bulk [50]. In these two publications, the absolute distances from the metal film were determined. To measure relative distances, dual-color MIET was introduced by Chizhik et al. and used to measure the distance between the two lipid membranes of the inner and outer nuclear envelope in fixed cells. There, the distances of the two differently labeled membranes from the surface were measured sequentially and afterwards the distance between them was calculated [105]. Thus, MIET has been applied successfully to measure axial distances on the single molecule level and relative distances in bulk, but not relative distances in single molecules yet.

Here, we are interested in studying large (bio)molecular complexes on the single molecule level and obtain intramolecular distances. Measuring relative distances with dual color MIET has the disadvantage that FRET between the labels influences the measurement. This can be avoided by using only a single color for co-localization. Gordon and colleagues combined the superresolution approach of single molecule localization with step-wise photobleaching to co-localize fluorescent emitters laterally. The technique was named single-molecule high-resolution imaging with photobleaching (SHRIMP) and allowed to measure the lateral distance between two emitters with a precision of 5 nm [106, 107]. Based on the same idea of step-wise bleaching, we developed a new technique for axial co-localization.

The aim of this work is to measure intramolecular distances by using only one kind of label and to axially co-localize several individual emitters on the same structure. The sample was subject to two major challenges: First, in prospect of future applications, the environment should be close to the native environment of biomolecules, i.e. aqueous solution. Second, the sample should be robust and the distances of the labels should be known to verify our method. We chose DNA origami as a reference sample because of its 3D structure, rigidity, and easy addressability with fluorescent labels. DNA origami structures are commonly employed as reference samples for superresolution microscopy and even have been recently used as a traceable distance measurement standard for fluorescence microscopy [108].

In the following, we perform axial localization of single fluorescent emitters based on single molecule MIET. We use step-wise photobleaching to achieve axial co-localization of up to three emitters. The accuracy of the method is verified by using three-dimensional DNA origami structures with well-known geometry as reference.

4.2 METHODS

4.2.1 *Sample Preparation*

The DNA origami structures used for the experiments were designed in the group of *Philip Tinnefeld* in Braunschweig. The design of the DNA origami pillar from Puchkova et al. was used because the structure was designed to be rigid, upright on the surface, and with a total height of 125 nm fitted the effective MIET range [109]. By using staple strands modified with a fluorescent dye, the structure could be labeled at different positions. Eight anchoring sites with thiol groups (or biotins) on the bottom of the structure were used to achieve a vertical orientation of the surface-immobilized pillars. A schematic representation is shown in Fig. 4.2a. All DNA origami structures used in this work were prepared by *Izabela Kaminska* in the group of *Philip Tinnefeld* in Braunschweig. Details of the assembly can be found in Ref. [110] and on the original design in Ref. [109]. Briefly, all staple strands were mixed with the scaffold strand in TE buffer containing Mg^{2+} and annealed. DNA origami structures were then purified and AFM measurements validated the yield of the synthesis and the completeness of the assembly, see Fig. 4.2b for an example. The final sample concentration was 1–2 nM and was sent to Göttingen by mail. The stock samples were diluted 30–50 times in imaging buffer (Tris 10 mM, EDTA 1 mM, MgCl_2 12.5 mM, Trolox 2 mM) to achieve a low surface concentration ($< 0.2 \mu\text{m}^{-2}$). Prior to immobilization, a silicone sheet (GBL664384, Sigma-Aldrich) with a hole of about 8 mm diameter in the middle was placed on the coverslip. The so formed chamber could easily be sealed by placing another coverslip on top.

For *thiol immobilization*, the MgCl_2 concentration in the diluted sample was adjusted to 100 mM and directly incubated on a gold coated coverslip for 30 minutes. The sample was then gently washed with imaging buffer to remove structures that did not attach to the surface and sealed with a coverslip.

For *biotin-NeutrAvidin immobilization*, silica coated coverslips were used with the silicone sheet as described above. 80 μL of BSA-biotin (0.5 mg/mL, A7641, Sigma-Aldrich) were incubated for 60 minutes and washed three times with 100 μL of buffer A (Tris 10 mM, NaCl 100 mM). This was followed by the incubation of 80 μL of NeutrAvidin (0.5 mg/mL, 31000, ThermoFisher) for 5 minutes, and finally washed three times with buffer A. The stock solution containing the DNA origami structures was diluted 30–50 times in TE buffer with 12.5 mM MgCl_2 and incubated for 60 minutes. Finally, the sample was washed at least three times with imaging buffer.

PREPARATION OF COVERSLEIPS Glass coverslips (24 mm \times 24 mm, #1.5, thickness 0.17 mm, Menzel) were cleaned in KOH solution (10 g KOH pellets in 240 ml Ethanol (80%)) in an ultrasonic bath for 10

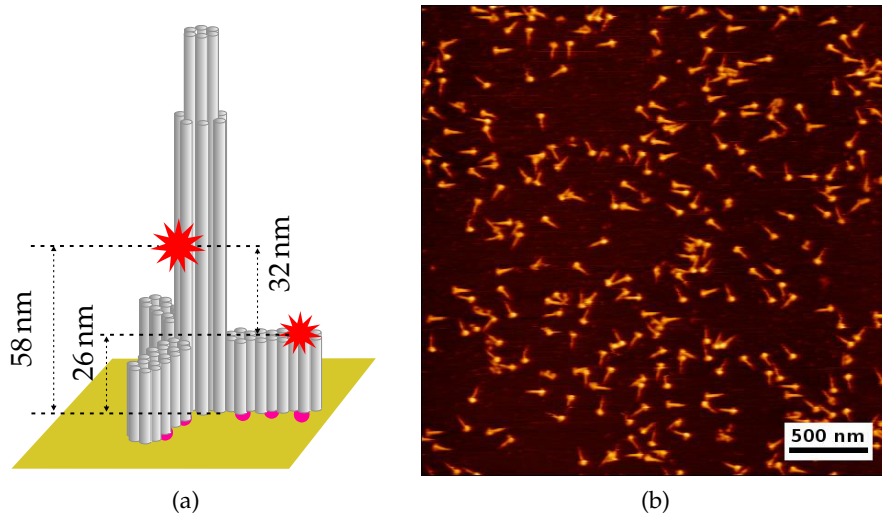


Figure 4.2: a) A DNA origami pillar was designed with dyes at different distances from the surface. Here, eight thiol groups on the bottom of the structure can bind to the gold directly to ensure the vertical orientation of the pillar. This figure was adapted from *Roman Tsukanov*. b) AFM image of the DNA origami pillars. This figure was reproduced from [110].

minutes, followed by three ultrasonic baths in deionized water for 2 minutes each. The clean coverslips were coated with a 10 nm thin film of gold or silver on top of 2 nm titanium which improves the adhesion to glass. The thin films were generated by chemical vapor deposition using an electron beam source (Univex 350, Leybold) under high-vacuum conditions (10^{-6} mbar). The lowest deposition speed of 1 \AA s^{-1} was chosen and the film thickness monitored using an oscillating quartz unit. For coverslips with a silica spacer, additional layers of 1 nm titanium and 10 nm SiO_2 were deposited in the same way.

The surface roughness of the coverslips were measured by AFM and showed a RMS roughness of 0.5 nm (cleaned glass coverslip), 1.5 nm (BSA-biotin coated on mica), and 1 nm (BSA-biotin coated on cleaned glass).

The coverslips were prepared by *Alexey Chizhik* and the AFM measurements for surface characterization were performed by *Amna Khalid*.

4.2.2 Setup

The experiments were carried out on the commercial Microtime 200 setup (PicoQuant, Germany). The light of a 640 nm pulsed diode laser (LDH-D-C-640, PicoQuant), equipped with a cleanup filter (Z640/10, Chroma Technology), was coupled into a polarization-maintaining single mode optical fiber (Schäfter + Kirchhoff). An achromatic $\lambda/4$ wave plate (Thorlabs) was used to modify the polarization from linear to circular. The light at the fiber output was collimated by an objective and reflected by a dichroic mirror (FITC/TRITC, Chroma Tech-

nology) into an inverted microscope (IX71, Olympus). An objective (UAPON 100 \times oil, 1.49 NA, Olympus) was used to focus the light into the sample and to collect the fluorescence. A tube lens focused the light on a 150 μm pinhole to block out-of-focus light. A second lens recollimated the light and a third lens focused it onto a single-photon counting module (SPCM-CD 3516 H, Excelitas Technologies). In the collimated beam path, a long pass filter (F76-649, AHF) and an emission bandpass filter (BrightLine HC 692/40, Semrock) were inserted. A laser driver (PDL 828 "Sepia II", PicoQuant) controlled the repetition rate of the laser which was set to 20 MHz. The pulses were synchronized to the TCSPC electronics (HydraHarp 400, PicoQuant) which recorded the photon arrival times with a resolution of 32 ps. A piezo stage (P-562.3CD with controller E-710.3CD, Physik Instrumente) was used to move the sample relative to the objective and scan images were acquired using the SymphoTime software (PicoQuant). A schematic of the setup can be seen in Figure 4.3.

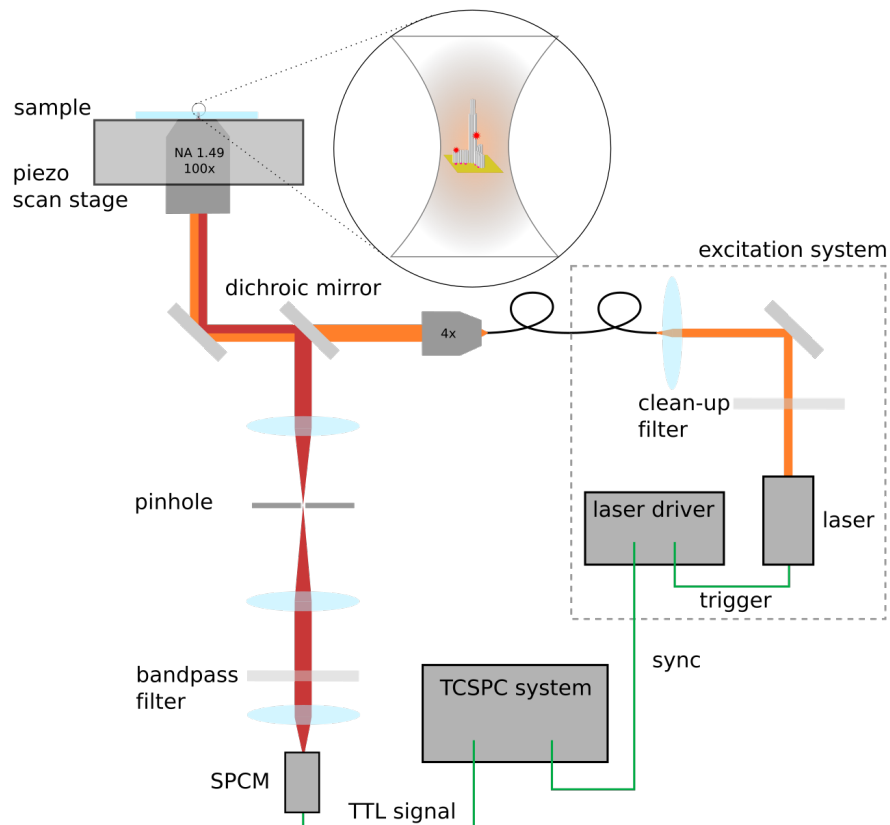


Figure 4.3: Schematic drawing of the setup. The excitation light is shown in orange and the emission from the sample in red. Green lines indicate electrical signals for the TCSPC system which was used for measuring the fluorescence lifetime. A piezo stage could move the sample relative to the objective to obtain a scan image of the sample.

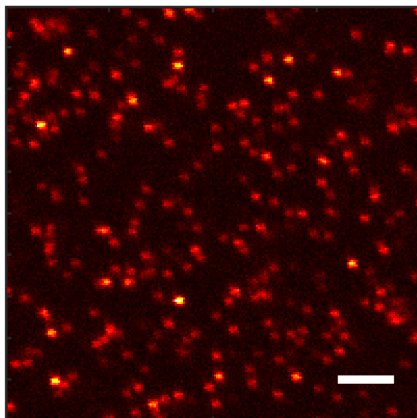


Figure 4.4: Scan image of the sample of the DNA origami pillar with two dyes on gold. Scale bar is 3 μm .

4.2.3 *Measurement Procedure*

The sample was scanned in confocal mode at a low laser power (usually by introducing a neutral-density filter (OD_1) into the excitation beam path) to avoid photobleaching. One scan region of $20\ \mu\text{m} \times 20\ \mu\text{m}$ contained about 50 to 150 labeled DNA origami structures. A typical example of a scan image can be seen in Figure 4.4.

Single molecule traces were recorded in the following manner: The laser was switched off, the focus was moved to the manually determined position of a bright spot in the scan image and a point measurement was started. Then, the laser was switched on, and the time trace was monitored until complete photobleaching of the dye, i.e. until the background level was reached. The recording was stopped, the laser switched off, and the focus could be moved to the next molecule. Very bright or very large spots would not be measured because they most probably contain aggregates (which was verified by observing more than the expected number of bleaching steps). Also, very dark spots were not recorded because they usually showed a very short lifetime or pure scattering and were probably either pillars lying flat on the surface or dirt.

In the SymphoTime recording software it was possible to define multi-point measurements for a fixed amount of time which was used to automate the process. However, we found it to be faster and more efficient to control parts of the process manually: Because bleaching time varied from a few seconds to several minutes, a large amount of time would be needed for each measurement which would increase the total measurement time. Furthermore, the software switches on the laser a bit earlier than the recording, so that a few thousands of

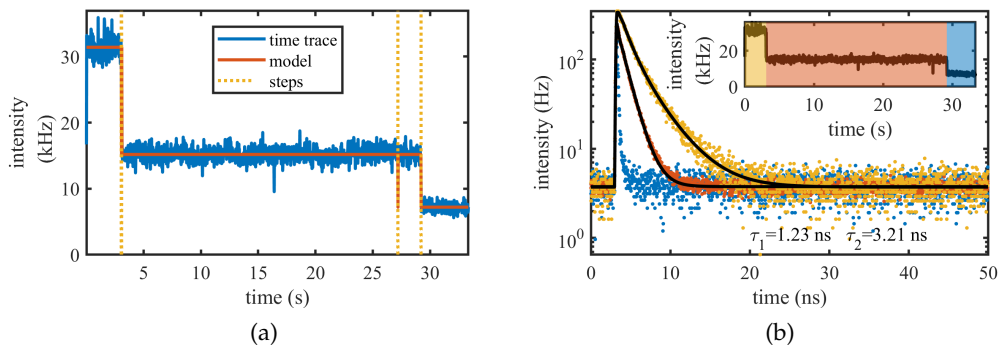


Figure 4.5: Data analysis. a) Recorded intensity time trace (blue) is analyzed with a step detection algorithm. From the model time trace (red), average intensities and transition times (yellow) can be computed. b) TCSPC histograms of the three segments (as shown in the inset) with a corresponding lifetime fit.

photons would be lost. Switching the laser on and off and stopping recordings after bleaching was thus done manually.

4.2.4 Data Analysis

Custom software written in Matlab was used throughout the project. The recorded TCSPC data files were first converted into time traces with a binning of 20 ms. Then, the traces were analyzed by the step transition and state identification method developed by Shuang and coworkers [111]. This method is based on minimizing the minimum description length (MDL) which takes into account the goodness of fit and the complexity of the model. In a first step, the optimum MDL for a given number of states is computed, and then the number of states corresponding to the global minimum MDL value is considered the optimum solution. We used a slight modification by limiting the maximum number of states to $n_E + n_B + 2$, where n_E is the number of expected labels on one structure and n_B the number of background states ($n_B = 2$ if the laser was switched on and off during the recording, $n_B = 1$ otherwise). This was done to limit the fitting complexity, and at the same time to account for additional states because of photophysics or aggregates. In the model, state changes were identified and a TCSPC histogram was computed from the raw data for each segment of the trace. An example of an intensity time trace with the fitted model is shown in Figure 4.5a. As can be seen there, not all transition steps correspond to bleaching events but also to blinking such as at about 27 s where the intensity drops shortly to the background level. Thus, the TCSPC histogram of segments from the same state were summed and then fitted to obtain the lifetime which will be explained in more detail in the following.

4.2.4.1 Lifetime Fitting

As can be seen from the blue curve in Figure 4.5b, the lowest intensity state corresponds to the background with all fluorescence bleached. The peak visible is mainly due to photoluminescence of the gold [112]. For the other TCSPC histograms, fluorescent lifetimes can be fitted using the following model function

$$I(t|n_j) = \text{IRF}(t) \otimes \sum_{i=1}^{n_j} \frac{a_i}{\tau_i} e^{-\frac{t}{\tau_i}} + a_0 \text{IRF}(t) + b, \quad (4.6)$$

where the τ_i are the fluorescence lifetimes of n_j emitters with amplitudes a_i , b is a constant background, a_0 the scattering amplitude, $\text{IRF}(t)$ is the instrument response function, and \otimes denotes convolution. For this fitting model, there are $m = 2n_j + 2$ fit parameters. As a goodness-of-fit parameter we calculated the reduced χ^2 value

$$\chi_{\text{red}}^2 = \sum_t \frac{(I(t) - H(t))^2}{I(t)(M - m)}, \quad (4.7)$$

where $H(t)$ is the measured TCSPC histogram with M bins.

Assuming that the second state corresponds to a single dye, the fit function $I(t|n = 1)$ was used and a lifetime τ_1 obtained. For the higher state, the model $I(t|n = 2)$ was fitted to the data with the lifetime τ_1 fixed from the previous fit to obtain a lifetime τ_2 .

Sometimes states did not correspond to bleaching molecules, which made the data more difficult to analyze. Possible reasons for this include blinking of the dye and state switching (probably isomerization of the dye Atto 647N or interactions of the dye with the environment). To identify those states, each histogram was first fitted with the same number of emitters as before and if the difference in lifetime was smaller than 10%, the state was considered to be the same as the previous and histograms were summed up and fitted together.

The IRF was determined from measurements that contained no fluorescence signal but only gold photoluminescence (such as the blue TCSPC histogram in Fig. 4.5b). Time resolved measurements of gold luminescence have shown that the decay is faster than picoseconds which is much smaller than the response time of our detectors or TCSPC hardware. Because the gold photoluminescence has a relatively broad emission spectrum, it can be used to measure the IRF at the same wavelength as the fluorescence emission of the dye. This is an advantage compared to other methods that use for example scattering to determine the IRF at a different wavelength since these often suffer from artifacts due to color shifts of the IRF [113]. However, small shifts could still occur because of which our fitting routine included the color shift of the IRF as an additional parameter. After a first run of the lifetime fitting for all molecules measured on one day, the mean value of all fitted color shifts was calculated and the data was fitted again with this value fixed to reduce the number of free parameters.

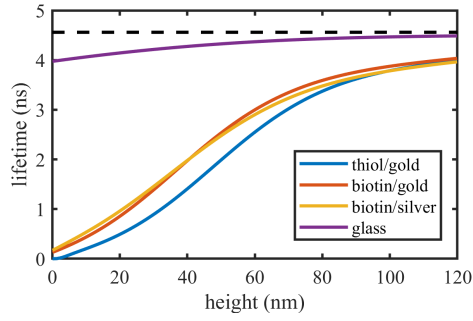


Figure 4.6: Lifetime of a dipole emitter with a free-space lifetime of 4.56 ns and a quantum yield of 82 % at 688 nm emission.

4.2.4.2 MIET Curve Calculation

Lifetimes were converted into heights by using the MIET curve shown in Fig. 4.6 assuming a random orientation of the emitter. For the MIET curve, a layered surface was assumed with glass as an infinite lower halfspace and thin films of gold or silver on top. For the biotin-avidin immobilization protocol on glass (biotinylated pillars), an additional layer of silica ($n = 1.46$) was evaporated on top. The thin film layers for all experiments can be found in Table 4.2 below and the refractive indices of the materials were taken from ellipsometry measurements by Rakić et al. [114]. Furthermore, we assumed the embedding medium to be water ($n = 1.33$).

| sample | T ₁ /T ₂ /T ₃ | B ₁ /B ₂ | B ₁ S |
|----------|--|--------------------------------|------------------|
| material | | | |
| glass | ∞ | ∞ | ∞ |
| titan | 2 nm | 2 nm | 2 nm |
| gold | 10 nm | 10 nm | |
| silver | | | 10 nm |
| titan | | 1 nm | 1 nm |
| silica | | 10 nm | 10 nm |

Table 4.2: Thickness of the layers used for the calculating the MIET curve for different samples (T/B: pillar immobilized via thiol groups or biotin-avidin; 1/2/3: number of dyes on the pillar; S: on silver, all other on gold).

The free space fluorescence lifetime of Atto647N on the origami pillars was measured in solution and found to be 4.56 ns. The manufacturer's specification for the uncoupled dye are $\tau_{\text{uncoupled}} = 3.6$ ns with a quantum yield of $\text{QY}_{\text{uncoupled}} = 65\%$. Assuming that coupling of the dye to DNA only changes the non-radiative rate, we estimated the quantum yield of the dye on the origami to be 82 % (cf. Eq. (2.11)). We set the emission wavelength of the dye to 688 nm, which is the

mean emission wavelength of Atto647N within our emission filter window (692/40 nm bandpass).

4.2.4.3 Distance Estimation

For samples with dyes at more than one position, also the distance between the emitters along the optical axis can be estimated. Because the distance is non-negative, the distribution of distances is expected to be asymmetric. This can skew the mean and standard deviation of these distributions, especially when the error is close to the expected distance. Therefore, we would prefer a model that describes the distribution. As an approximation, we will assume that our measured heights are normally distributed. Churchman et al. showed that under this assumption the distribution of the distance is non-Gaussian [115]. Instead, the probability density to measure a distance in one dimension $r = |r_2 - r_1|$ given the true distance $\mu = |r_2^{(\text{true})} - r_1^{(\text{true})}|$ is

$$p(r|\mu, \sigma) = \sqrt{\frac{2}{\pi\sigma^2}} \exp\left(-\frac{\mu^2 + r^2}{2\sigma^2}\right) \cosh\left(\frac{\mu r}{\sigma^2}\right), \quad (4.8)$$

where $\sigma^2 = \sigma_1^2 + \sigma_2^2$ is the sum of the variances of the positions r_i . We use μ as an estimator for the average distance and σ for its precision. Only for small measurement errors or large distances, the distribution becomes approximately Gaussian. More precisely, for $\frac{\mu r}{\sigma^2} \gg 1$ we find $\cosh\left(\frac{\mu r}{\sigma^2}\right) \approx \frac{1}{2} \exp\left(\frac{\mu r}{\sigma^2}\right)$, then

$$\begin{aligned} p(r) &\approx \frac{1}{\sqrt{2\pi\sigma^2}} \exp\left(-\frac{\mu^2 + r^2}{2\sigma^2}\right) \exp\left(\frac{\mu r}{\sigma^2}\right) \\ &= \frac{1}{\sqrt{2\pi\sigma^2}} \exp\left(-\frac{(\mu - r)^2}{2\sigma^2}\right). \end{aligned} \quad (4.9)$$

Fitting this distribution is accomplished by the maximum likelihood method. For a set of observations $\{r_i\}$ the likelihood of these observation given the parameters μ and σ is

$$P(\{r_i\}|\mu, \sigma) = \prod_i p(r_i|\mu, \sigma). \quad (4.10)$$

The parameters are estimated by finding the minimum of the negative log-likelihood

$$-\log P(\{r_i\}|\mu, \sigma) = -\sum_i \log p(r_i|\mu, \sigma). \quad (4.11)$$

4.3 RESULTS

4.3.1 *Axial Localization of Single Emitters*

Here, we want to measure the height of single Atto647N emitter which is attached to a DNA origami pillar at a designed height of 82 nm. The bleaching time traces were analyzed as described in Section 4.2.4. Since here only one lifetime is expected, all on-states in a single time trace were combined and the TCSPC histogram was fitted with a mono-exponential function. Three different samples were studied:

T1: DNA origami pillar immobilized via thiol groups on 10 nm gold

B1: DNA origami pillar immobilized via biotin on 10 nm gold and 10 nm silica

B1S: DNA origami pillar immobilized via biotin on 10 nm silver and 10 nm silica

In case of the biotinylated pillars, the surface was additionally coated with a BSA-biotin layer and incubated with NeutrAvidin to ensure specific immobilization. Furthermore, a control measurement of biotinylated pillars immobilized on pure glass was performed. For this sample, we obtained an average lifetime of (4.2 ± 0.2) ns which agrees with the theoretical expected value of 4.37 ns for the lifetime of the dye at the design height of 82 nm on top of a pure glass surface.

The measured lifetimes of the three samples were converted into heights using the MIET curves in Fig. 4.6. The histograms of lifetime and height are shown in Fig. 4.7. In all cases, a unimodal distribution was found and fitted with a Gaussian function with offset. We interpret the offset as a result of bad fits or tilted pillars. The mean values and standard deviations of the Gaussians are listed in Table 4.3.

The heights of all samples are very similar to each other, but do not agree with the design height of 82 nm. Furthermore, we expected a larger height for the biotinylated samples as the BSA layer should add to the height of the pillar. Since the design height of the DNA origami seemed to be underestimated in all cases, we performed an independent measurement of the DNA origami size by 3D DNA-PAINT. For this experiment, the pillar was labeled with docking strands at the bottom and top with a designed distance of 90 nm between them. The pillar was immobilized on a BSA-biotin coated glass coverslip and 3D DNA-PAINT imaging was performed. By means of astigmatic imaging, the 3D position of the docking sites could be measured, see Fig. 4.8 for the results. The distance between the two docking sites was (84 ± 10) nm, which is about 7% less than the designed distance of 90 nm. Furthermore, the 3D DNA-PAINT measurement showed a tilt distribution with an average tilt angle of $(35 \pm 21)^\circ$ with respect to the surface normal.

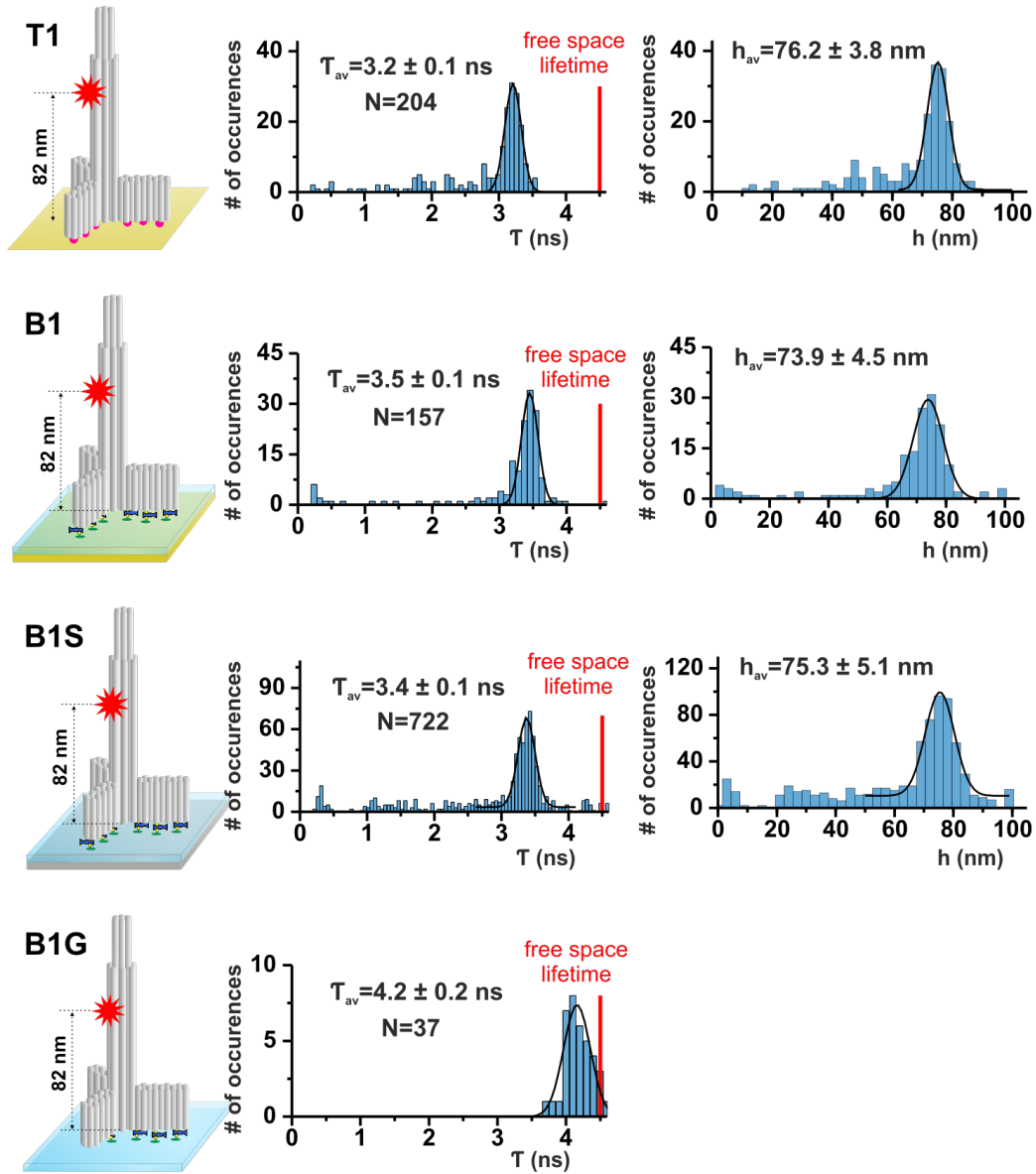


Figure 4.7: Lifetime and height histograms for the single labeled pillar on different substrates (T/B: pillar immobilized via thiol groups or biotin-avidin; S: on silver, G: on glass, all other on gold).

| design height (nm) | reference height (nm) | measured height (nm) | sample | method |
|-----------------------|--------------------------|-------------------------|--------|-----------|
| 90 | 84* | 84 ± 10 | B2G | DNA-PAINT |
| 82 | 76.5 | 76.2 ± 3.8 | T1 | MIET |
| 82 | 76.5 | 73.9 ± 4.5 | B1 | MIET |
| 82 | 76.5 | 75.3 ± 5.1 | B1S | MIET |

Table 4.3: Heights of single labeled pillars. Comparison of design heights with the measured values for different samples (T/B: pillar immobilized via thiol groups or biotin-avidin; 1/2: number of dyes on the pillar; S: on silver, G: on glass, all other on gold). The independent experiment using 3D DNA-PAINT suggests a shrinkage of the whole structure of about 7%.

*) This value is used to compute the reference value from the other design heights. smMIET experiments are in agreement with the reference values.

Deviations from the designed distances have been reported in the literature before for DNA origami structures under similar experimental conditions [116]. Furthermore, the design height was calculated using a simplified model of DNA which does neither take into account interhelical distances, bending, nor twist. We therefore assume that a deviation of the designed height from the actual height is the most probable explanation for our observations. By assuming a linear shrinkage of the whole structure, we calculated a new reference distance from the design height. This agrees with our measured heights within the error (see Table 4.3). For the T1 sample, we assume that the height of the immobilization layer (thiol bonds) is negligible and the pillar is vertical. For the biotinylated samples, the situation is more complicated: On one hand, the 3D DNA-PAINT suggest that the pillars are tilted which reduces our observed height. On the other hand, the immobilization layer thickness is unknown and adds to the measured height. By assuming a tilt angle of 35° as measured by 3D DNA-PAINT, we estimate the height of the immobilization layer to about 12 nm. A more detailed analysis of the immobilization layer thickness can be found in Section 4.3.2.8. The above interpretation of our measured heights for our three samples assumes that the heights measured by MIET are unbiased. In the next section, we study how the MIET curve can affect the accuracy of our MIET measurements.

4.3.1.1 MIET Curve Error Estimation

In the previous sections, we measured the height of emitters on a DNA origami structure and found that the measured values deviated from the design values. We could explain the deviations by sample tilt and the unknown thickness of the biotin immobilization layer. Another possible bias can be introduced when converting the lifetime to

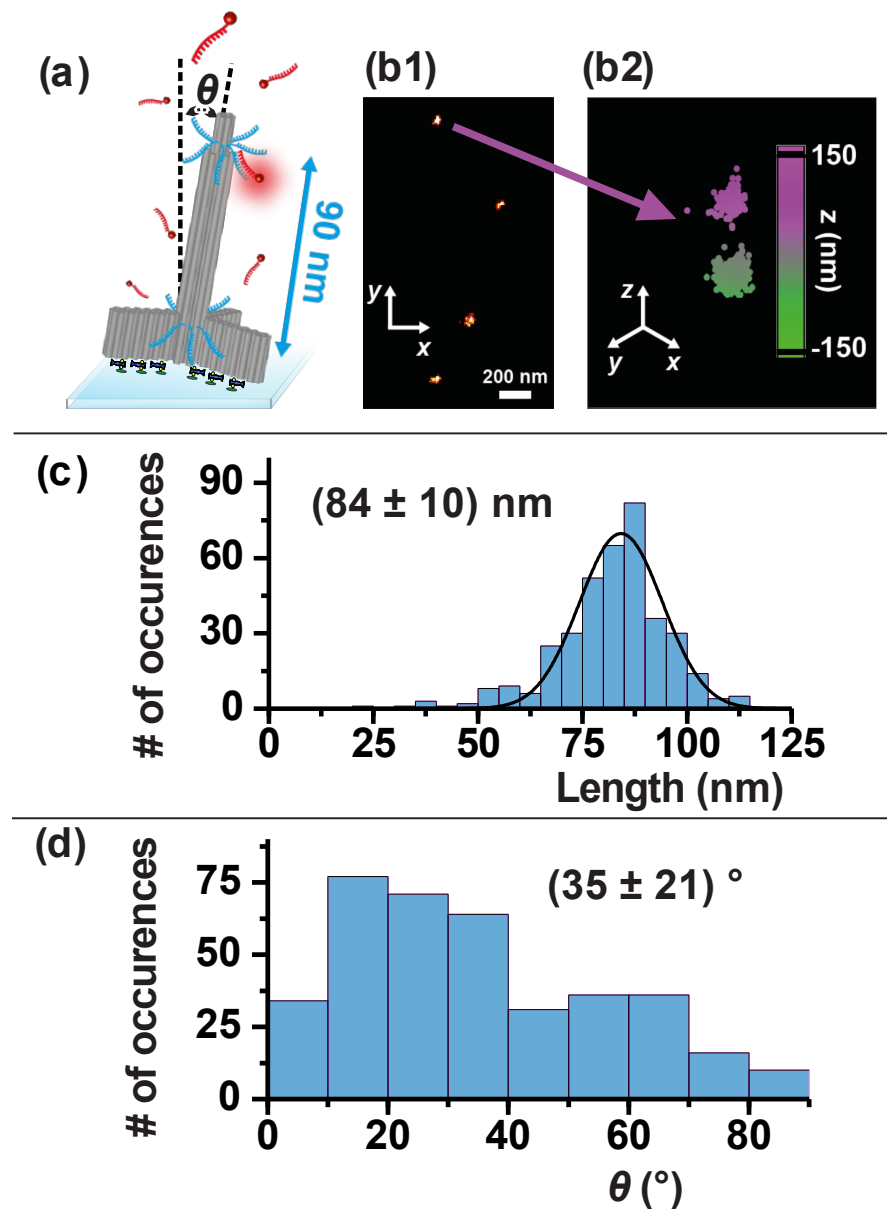


Figure 4.8: 3D DNA-PAINT experiment. a) The same DNA origami pillar as for the MIET experiments was used and immobilized via biotin to the glass surface. Docking strands were attached with a design distance of 90 nm. b1) Localization map of the DNA origami structures. b2) Astigmatic imaging yields a z position of each blinking event. Each point is a localization event. From the two point clouds, the length of the pillar and its tilt angle is estimated. c) Length histogram. The mean length is about 7% shorter than the design value. d) Tilt distribution. The experiment and the data analysis were performed by *Mario Raab*. The figure was adapted from Ref. [110].

the height by means of the MIET curve. Here, we investigate the influence of the MIET curve on the accuracy of the heights.

The theory of MIET enables us to calculate the exact dependence of the fluorescent lifetime of a dipole emitter on top of a metal surface with respect to its height. This curve, the MIET curve, is then used to estimate the height from the measured lifetime. Its shape depends on the layer system of the surface as well as intrinsic properties of the dye (cf. Section 2.4). If these parameters are not precisely known, the heights measured by MIET will not be accurate. To estimate the error, we performed theoretical calculations of the MIET curve, varying the parameters up to 10%. Our experimentally determined parameters from Section 4.2.4.2 were assumed as the ground truth and used for the calculation of the true MIET curve $\tau(z|\mathbf{p}_{\text{true}})$. Here, \mathbf{p}_{true} is the parameter vector of all parameters entering the calculation. Usually, a measured lifetime is converted into a height by using the inverted curve $z(\tau|\mathbf{p}_{\text{true}})$. This curve accurately predicts the height of an emitter with lifetime τ . However, if one parameter in \mathbf{p} is estimated erroneously, we would compute the corresponding MIET curve $\tau(z|\mathbf{p})$ and use its inverse $z(\tau|\mathbf{p})$ to convert the lifetime into a height. The height error is then $\Delta z = z(\tau|\mathbf{p}) - z(\tau|\mathbf{p}_{\text{true}})$.

In Fig. 4.9, we show the influence of six parameters on the axial localization error. Each parameter was allowed to vary by $\pm 10\%$ from the ground truth, and the height error is shown as a function of the varied parameter and the true height. We investigated intrinsic parameters such as the free space lifetime, the free space quantum yield, and the orientation¹ as well as parameters of the metal film, such as the thickness of the gold film, and the real and imaginary part of the refractive index of the gold. For the intrinsic parameters of the dye, the error increases with height whereas the parameters of the gold film show a minimum error around 50 nm. Below 20 nm, the error by variations of the intrinsic parameters is less than 2 nm, but can increase to more than 5 nm above a height of 60 nm. Note that the error has an opposite sign when the free space lifetime and the quantum yield are over- or underestimated at the same time. In contrast, the errors by over- or underestimating the imaginary part of the refractive index of gold and the film thickness correlate with each other. Notably, the real part of the refractive index of the gold has almost no effect on the MIET curve. Apart from that, all other parameters influence the MIET curve.

The effect of a 10% uncertainty in the parameters lead to an accuracy of MIET on the order of 5 nm which is comparable to the precision we obtained in our experimental results. However, the influence was probably much smaller. Of all parameters we explored above, the free space lifetime showed the maximum error of 15 nm which, however, could be accurately measured in bulk. The measurement in

¹ Here, the orientation was described by the ratio of vertical to parallel emitters in an ensemble.

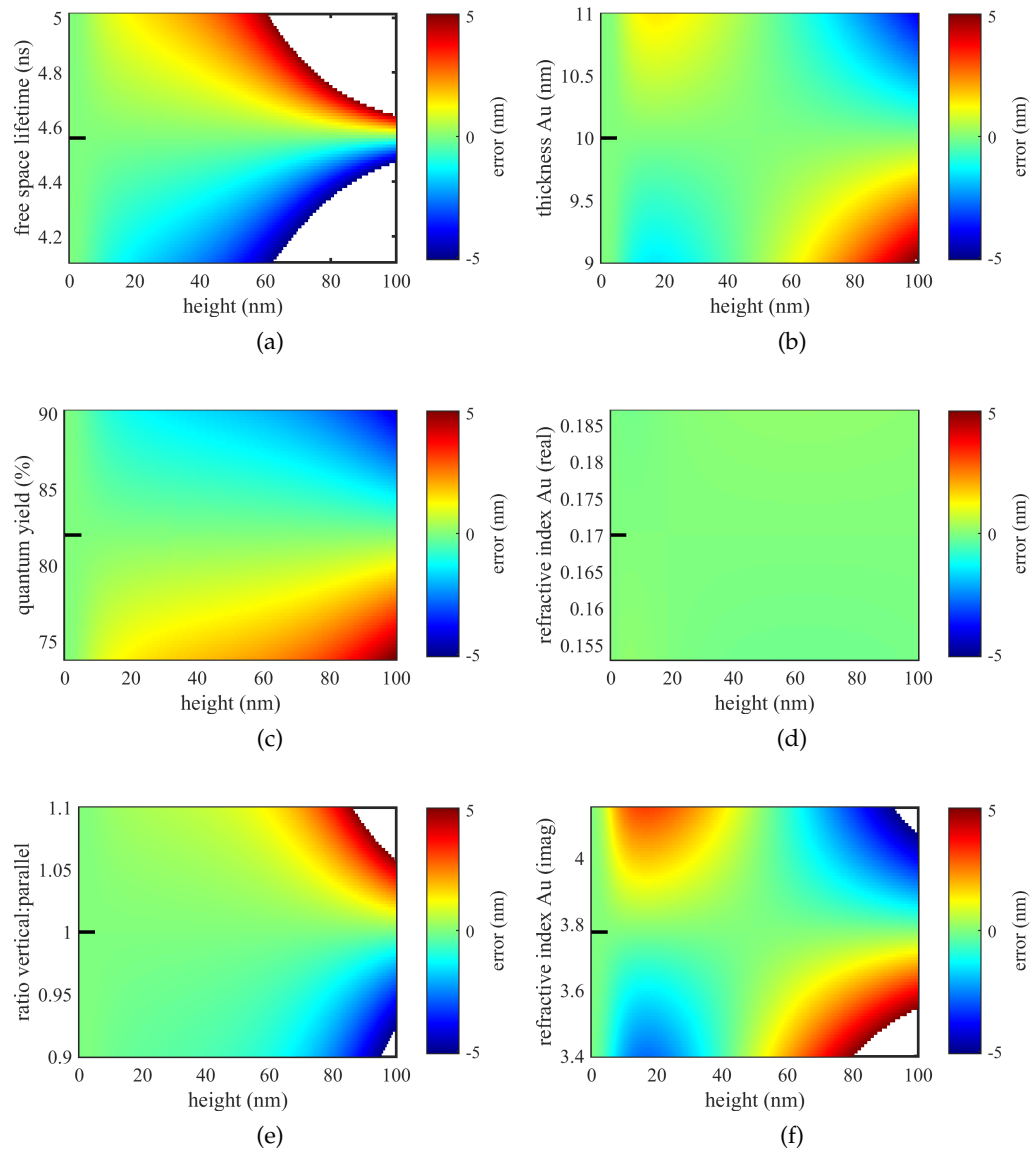


Figure 4.9: Theoretical calculation of the height error when a parameter of the MIET curve calculation varies up to 10%. The black line indicates the “true” value of the parameter that was used for the smMIET co-localization experiments. On the left side, we show the influence of some parameters of the dye: a) free space lifetime, c) free space quantum yield, and e) emitter orientation. On the right side, the influence of the metal thin film is shown: b) gold thickness, d) real part of the refractive index of gold, and f) imaginary part of the refractive index of gold. In the white parts of the plots, the absolute error is larger than 5 nm.

solution has a low background and is not limited by photobleaching, so a large number of photons can be collected which allows to determine the lifetime with arbitrary precision. In the ideal case (Eq. (2.5)), already 10^4 photons suffice for a precision of 1%. The free space lifetime was used furthermore to estimate the quantum yield according to Eq. (2.11) where $QY_0 \propto \tau_{\text{free}}$. But as we saw above, the errors of the quantum yield and the free space lifetime have opposite signs, and thus, a small error in the free space lifetime would be compensated by the quantum yield. Wrong estimation of the orientation lead to an error below 1 nm within a range of up to 70 nm, and thus was small within the range of our DNA origami pillar. The parameters for the gold film have been used in other studies using MIET [50, 104, 105], including various control experiments, and we therefore regard the parameters as sufficiently accurate. Also, the influence of the refractive index of the medium was found to be small [55].

In summary, the free space lifetime was found to have the highest influence on the MIET curve, but can be measured with high precision. The errors introduced by other parameters were small compared to the statistical variation of 5 nm in our experiments. Based on these observations, we assume that errors for determining the parameters of the MIET curve had a negligible influence on the accuracy of our experiments. For our measurements this means that we were able to accurately measure the distance of a single emitter from the surface with a precision of about 5 nm using both gold and silver. The localization precision is not to be confused with the resolution of the method, i.e. how well we can distinguish two emitters close to each other. To investigate this further, we performed experiments on DNA origami structures labeled with two emitters and show the results in the next section.

4.3.2 Co-localization of Two Emitters

In this section, we study a DNA origami structure that is labeled with two dyes with a designed axial distance of 32 nm (cf. Fig. 4.2a). To be able to distinguish between the two emitters, we chose a step-wise bleaching approach. Therefore, we will start with an analysis of the bleaching behavior of the sample. Afterwards, we will show how the two-dimensional histogram of the lifetimes can be used to effectively filter the data to obtain a high localization and co-localization precision. We will test the data analysis on simulated data to exclude any kind of bias introduced by the lifetime fitting or further analysis. Then, we will combine the results from the bleaching analysis and the lifetime analysis to discuss how MIET can protect the fluorophore from photobleaching.

As before, we have one sample that is immobilized on gold directly via thiol groups and a biotinylated pillar for which we will use the following abbreviations:

T2: DNA origami pillar immobilized via thiol groups on 10 nm gold

B2: DNA origami pillar immobilized via biotin on 10 nm silica on 10 nm gold

As we have seen in the previous section that the immobilization via biotin leads to a tilt of the structure, we will first analyze the T2 sample in detail as the results are easier to interpret, and discuss the results of B2 afterwards.

4.3.2.1 Step-wise Bleaching

With two emitters on a structure, we expect to see up to two bleaching steps such as in Fig. 4.5a. For each trace, the number of states n_s , their intensity I_j , and their on-times T_j are obtained from a step transition algorithm as described in Section 4.2.4. The states that showed similar fluorescent lifetimes were averaged by summing up the on-times and calculating an average intensity weighted by the T_j . The distribution of the on-times can be seen in Figure 4.10, roughly following an exponential distribution. We observed that the emitter with the high intensity usually bleaches first. The reason for this observation is probably that photobleaching is related to the fluorescence lifetime of the emitter. Photobleaching is a photo-chemical reaction and usually occurs when the molecule is in the excited state. So one expects that the on-time of the molecule should be inversely proportional to the time it spends in the excited state, i.e. its fluorescence lifetime τ . Indeed we find that the ratio of the on-times is $T_1/T_2 = 2.8 \pm 1.2$ which compares well with the lifetime ratio of $\tau_2/\tau_1 \approx 2.5$, cf. Fig. 4.10b. The different on-times create bleaching steps that are well separated in time which simplifies the data analysis. The effect of the fluorescence lifetime quenching by MIET on the bleaching time are further discussed in Section 4.3.2.6.

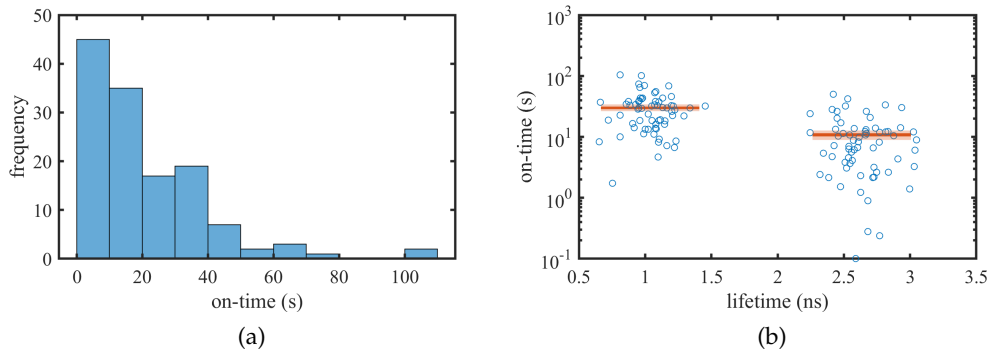


Figure 4.10: On-times of the filtered T2 data. a) The on-time distribution. b) The on-times with their corresponding lifetimes. The red line shows the mean value with a $3\sigma_{\text{SEM}}$ error region (shaded area). The average on-times were $T_{\text{on}}(\tau < 1.7) = 30 \pm 8 \text{ s}$ and $T_{\text{on}}(\tau < 1.7) = 11 \pm 4 \text{ s}$.

4.3.2.2 Lifetime Filtering

From each state in the time trace, a TCSPC histogram was extracted and fitted as described in Section 4.2.4. In Fig. 4.5 we have already seen a typical time trace with the corresponding TCSPC histogram. In total, 481 point measurements were taken from two sample preparations, of which 348 were fitted with a lifetime curve. Point measurements were excluded if the lowest intensity level exceeded a predefined threshold (usually 30% above the background level) to avoid that the last emitter was not bleached at the end of the measurement. The majority of time traces were excluded because the step-finding algorithm found less than 3 intensity levels (two emitters and background). The fitted lifetimes were further filtered by including an upper limit for the lifetime of 5 ns and a lower limit for the amplitude of 5%. Finally, fits with $\chi_{\text{red}}^2 < 2$ were also excluded from further analysis.

Up to 4 different lifetimes were fitted. As can be seen in Fig. 4.11a, the first and second emitter fits make up the majority of the fits. These two lifetimes are shown in Fig. 4.11b in a two dimensional histogram. There is a clear peak visible, which was fitted with a 2D Gaussian (as shown by the contour). The 3σ region around the center position ($\tau_c = (1.03 \text{ ns}, 2.61 \text{ ns})$), shown by the black square) contained 65 molecules and was used for additional filtering in the following sections.

4.3.2.3 Height

The fitted lifetimes were converted into heights via the MIET curve (see Section 4.2.4). Two populations can be distinguished in Fig. 4.12. We associated these two populations with the two emitters at different heights and found the average position by fitting a sum of two Gaussians to the histogram. In Table 4.4, we compare the fitted heights with the reference heights which were computed from the de-

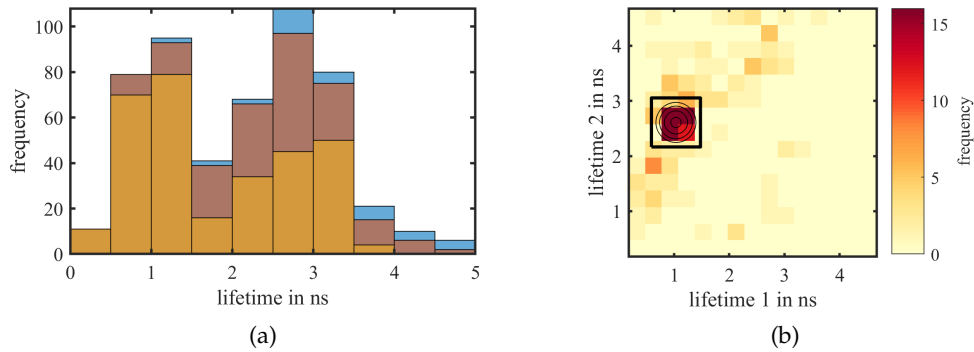


Figure 4.11: Lifetime Histograms of T2. a) The lifetime histogram of the last bleached emitter is shown in yellow, the next in red, and all later emitters in blue. b) Lifetime histogram of the last bleached emitter (lifetime 1) and the second emitter (lifetime 2). The contours in black show a two-dimensional Gaussian fit to the peak and the black square shows the 3σ area used for filtering.

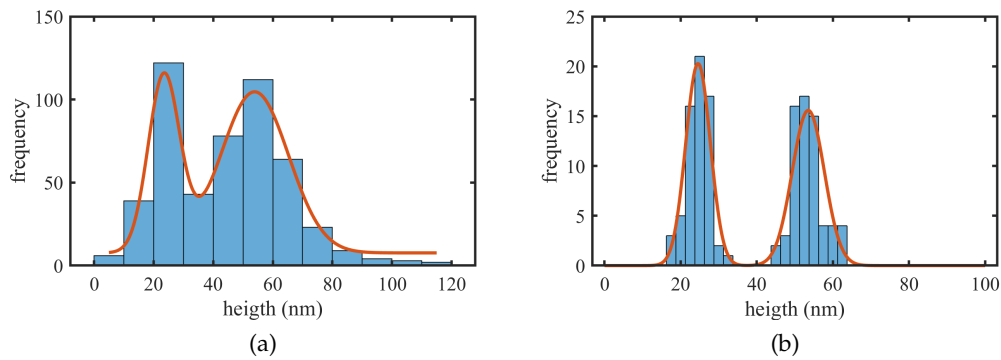


Figure 4.12: Height histograms of T2. a) All data with peaks at (54 ± 11) nm and (23.5 ± 5.4) nm, $N = 137$. b) Filtered data with peaks at (53.1 ± 4.5) nm and (23.6 ± 3.5) nm, $N = 65$. Both histograms were fitted with a double Gaussian fit.

sign heights by assuming a shrinkage of the whole structure that was found by 3D DNA-PAINT (cf. Section 4.3.1). By using the 2D lifetime histogram filtered data only as described in Section 4.3.2.2, we find that the width of the distribution is dramatically decreased, i.e. from 11 nm to 4.5 nm and from 5.4 nm to 3.5 nm. Within their errors, the measured heights agree with the reference values. As an additional check, we also compute the distance between the two emitters in the next section.

| design height (nm) | reference height (nm) | measured height (nm) | sample | filtered |
|--------------------|-----------------------|----------------------|--------|----------|
| 90 | 84* | 84 ± 10 | B | |
| 58 | 54.1 | 54 ± 11 | T2 | no |
| 26 | 24.3 | 23.5 ± 5.4 | T2 | no |
| 58 | 54.1 | 53.1 ± 4.5 | T2 | yes |
| 26 | 24.3 | 23.6 ± 3.5 | T2 | yes |
| 58 | 54.1 | 59.0 ± 4.7 | B2 | yes |
| 26 | 24.3 | 34.9 ± 4.0 | B2 | yes |

Table 4.4: Heights of dual labeled pillars. The last column indicates if the 2D filtered data were used as described in Section 4.3.2.2.

*) This value from the 3D DNA-PAINT experiments was used to compute the reference value from the other design heights. Results for B2 were added for comparison, see Section 4.3.2.7 for the analysis.

4.3.2.4 Distance

With the two localized positions, we estimate the height difference between the two emitters simply from the difference of the heights in Table 4.4. Alternatively, we can estimate the height difference from each DNA origami structure individually and thus from the co-localization. In other words, the first estimator corresponds to a difference of average heights, whereas the co-localization corresponds to the average of height differences. The distribution of those co-localized height differences is shown in Fig. 4.13. For the heights we assumed a Gaussian distribution. For the height difference, it is not a priori clear what the distribution will be since it must go to zero as there are no negative distances. We use the distribution derived by Churchman et al. which was introduced in Section 4.2.4.3. Fitting the data in Fig. 4.13 with this model, we obtain comparable distances as from the localization, but with a smaller error (cf. Table 4.5). For the filtered data, we even obtain a localization precision of less than 5 nm.

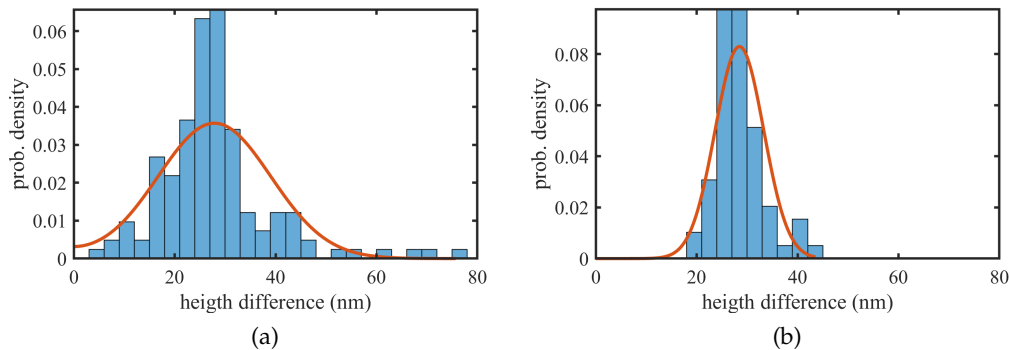


Figure 4.13: Distance histograms of the sample T2. In a) all heights as shown in Fig. 4.12 give a distance of (28 ± 11) nm. If only the 2D filtered data are used (see Fig. 4.11b), we obtain a distance of (28.5 ± 4.8) nm. While the average distance stays approximately the same, the precision of the filtered data has doubled. The histogram is shown as a probability density together with a fit of Eq. (4.8).

| design | reference | measured | method | filtered |
|----------------|---------------|----------------|---------|----------|
| distance (nm) | distance (nm) | distance (nm) | | |
| $58 - 26 = 32$ | 29.8 | 30 ± 13 | loc. | no |
| $58 - 26 = 32$ | 29.8 | 29.5 ± 5.7 | loc. | yes |
| $58 - 26 = 32$ | 29.8 | 28 ± 11 | co-loc. | no |
| $58 - 26 = 32$ | 29.8 | 28.5 ± 4.8 | co-loc. | yes |

Table 4.5: Height differences of the T2 sample. The reference values are computed from the 3D DNA-PAINT experiments and the design heights. The method column refers to the method to calculate the height difference: Either the mean values of the localized heights were subtracted (loc.), or the mean value of the difference of all co-localized heights was computed (co-loc.).

4.3.2.5 Simulation

We tested our data analysis on simulated data to estimate the influence of the fitting accuracy on the measured heights and distances. The simulated sample was the DNA origami structures with two dyes immobilized on gold via thiol bonds. We took the reference heights from Table 4.4 and calculated the lifetimes from the MIET curve as described in Section 4.2.4. For each emitter, the time until photobleaching was drawn from an exponential distribution with an average bleaching time inversely proportional to the lifetime (cf. Section 4.3.2.6). We used an experimental IRF to simulate the decay curve according to Eq. (4.6). The amplitudes of the lifetime components were proportional to the brightness (Eq. (2.27)) and the bleaching time, assuming that an emitter in free space on average emits

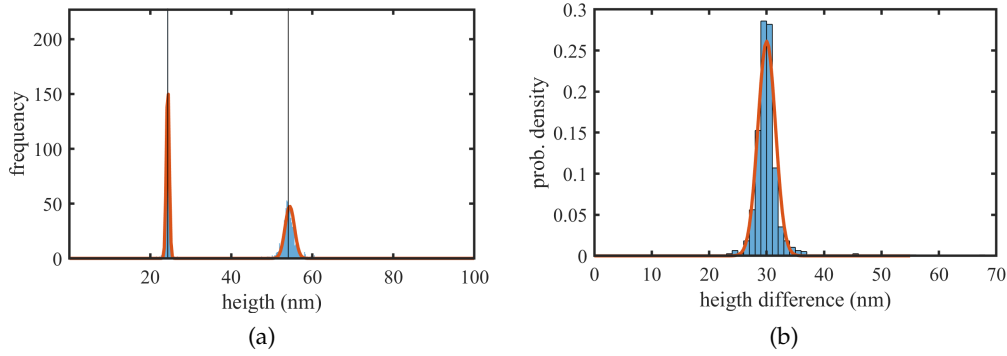


Figure 4.14: Simulation of the T2 pillar lifetime fitting. a) Height histogram with a fit of two Gaussians (red) and the reference value (vertical black line) for 1000 simulation runs. b) Height difference histogram of the data in a) with a fit to Eq. (4.8).

$3 \cdot 10^4$ photons before photobleaching. For the background as well as the scattering amplitude we assumed a constant rate of 10% of the emitter's emission rate in free space. Two decay curves were constructed: one with a single lifetime component corresponding to the emitter that bleached later, and the other with both lifetime components. Then, the TCSPC histograms were generated by drawing a Poisson random number, using the simulated decay curve as parameter. The two TCSPC histograms were then passed to the same function for lifetime fitting as the experimental data, using the same settings. The analysis also used the same filter criteria as before, yielding 766 pairs of fitted lifetimes out of 1000. In contrast to the experimental data, the 2D histogram showed a single peak and no outliers so that the 2D filtering was not necessary. The estimated heights were histogrammed as before and are shown in Fig. 4.14. From a Gaussian fit we obtained the heights of (24.3 ± 0.4) nm and (54.4 ± 1.2) nm which agree with the simulated values. In the ideal case, we would expect a precision of $\Delta h \approx h/\sqrt{N}$ (using Eq. (2.1) and assuming $h \propto \tau$). We estimate the number of photons from the fit amplitudes and obtain $(15.1 \pm 0.4) \cdot 10^3$ photons for the low lifetime emitter and $(9.8 \pm 0.3) \cdot 10^3$ for the long lifetime emitter. With these numbers we find that the precision of the height estimation is roughly a factor two larger than the ideal case. However, looking more closely at the distributions, they appear to have a larger tail than a Gaussian. We find that the standard deviation is about a factor two larger than the width of the Gaussian (mean and standard deviation of the two heights are (24.3 ± 0.8) nm and (54.3 ± 2.5) nm) which is consistent with the observation of a long tail.

In Fig. 4.14b the height distance of the two simulated emitters is shown together with a fit of Eq. (4.8). The fit result of (30.1 ± 1.3) nm reproduces the distance of 29.9 nm. Again, the distribution appears

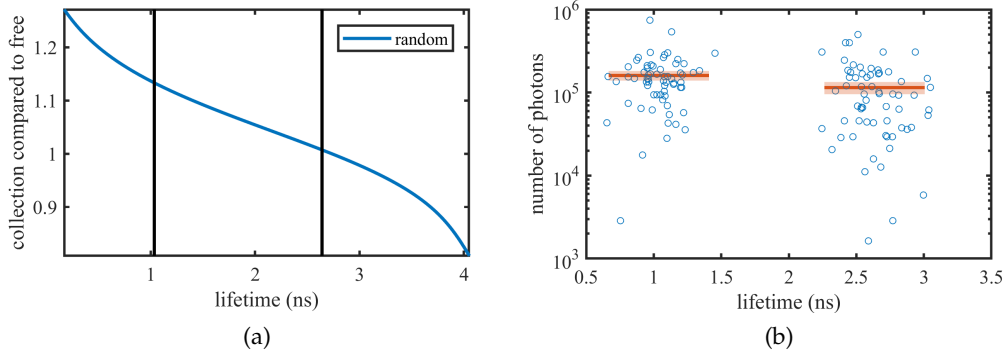


Figure 4.15: Protection from photobleaching by MIET. From emitters with a shorter lifetime, more photons can be collected on average. a) Theoretical calculations of the number of photons collected for the T2 sample. b) Fitted number of photons of the filtered T2 data. The average number of photons collected are $N(\tau < 1.7 \text{ ns}) = (1.60 \pm 0.14) \cdot 10^5$ (SEM) and $N(\tau > 1.7 \text{ ns}) = (1.15 \pm 0.13) \cdot 10^5$ (SEM).

to have a larger tail (the mean and standard deviation are $(30.0 \pm 2.5) \text{ nm}$).

4.3.2.6 Protection from Photobleaching

Photobleaching is a non-reversible process, often a chemical reaction of some part of the fluorophore with another molecule in the solvent [24]. These reactions often are photo-induced and occur when the molecule is in the excited state. We can assume the fluorophore bleaches after some total time T in the excited state, for example by a chemical reaction with a molecule in the solvent where the collision probability is constant over time. The total number of photons emitted by that molecule before photobleaching is then $N = T/\tau$, where τ is the excited state lifetime. On one hand, the quenching of the fluorophore by MIET reduces the lifetime and should lead to a higher photon budget according to this model. On the other hand, one has to consider the (radiationless) energy transfer to the metal which leads to a reduction in collected photons. Taking into account the collection efficiency and the relative quantum yield, we find

$$N(\tau) \propto \frac{\eta_r(\tau) \text{QY}_r(\tau)}{\tau}, \quad (4.12)$$

where η_r is the collection efficiency and QY_r is the local quantum yield for a randomly oriented emitter as described in Section 2.4.3.

In Figure 4.15a the ratio $N(\tau)/N(\tau_{\text{free}})$ is plotted. From the curve we can see that for low lifetimes (i.e. a high energy transfer), more photons can be collected from a molecule before photobleaching than in free space. The theoretical prediction for T2 is that 13% more photons should be collected from dye with lifetime around 1.0 ns than from the dye with 2.6 ns. The estimated number of photons from the

amplitudes of the lifetime fits of the T2 sample is shown in Fig. 4.15b. The mean values $N(\tau < 1.7 \text{ ns}) = (1.60 \pm 0.14) \cdot 10^5$ (SEM) and $N(\tau > 1.7 \text{ ns}) = (1.15 \pm 0.13) \cdot 10^5$ (SEM) show an increase of the low lifetime photons by 40%. Alternatively, the the number of photons can be estimated from the intensity time trace. The number of photons obtained from both methods show a good correlation (Pearson's $r = 0.92$), but the mean values differ: The average number of photons estimated from the intensity is $N(\tau < 1.7 \text{ ns}) = (1.41 \pm 0.12) \cdot 10^5$ for the short lifetime and $N(\tau > 1.7 \text{ ns}) = (1.30 \pm 0.15) \cdot 10^5$ for the long lifetime which corresponds to an increase of 9%. Because the number of photons is roughly exponentially distributed, the standard deviation of the data is quite large (i.e. of the same order as the mean value). Combined with the low number of data points ($N = 65$) this makes a reliable estimation of the ratio impossible. But whether we estimate the number of photons from fits or from the intensity levels, the trend is confirmed: more photons can be collected from emitters with low lifetime before bleaching as predicted by our simple model.

4.3.2.7 Results for B2

After the comprehensive analysis of the thiol immobilized pillar above, we will briefly state the results for the biotinylated sample. The flow of analysis was the same as above.

From 231 point measurements with fitted lifetimes, our filter criteria excluded 70 from further analysis. In the 2D lifetime histogram, we observed again a main peak and fitted it by a 2D Gaussian. In the 3σ surrounding we found 132 points that were used for further analysis. We observed that the width of the lifetime distribution is increased compared to T2. Furthermore, we found a correlation between the short and long lifetimes with a Pearson coefficient of $r = 0.51$. With $r = 0.79$, the correlation is even higher for the unfiltered data.

From the height histogram shown in Fig. 4.16b we obtain two heights of $(59.0 \pm 4.7) \text{ nm}$ and $(34.9 \pm 4.0) \text{ nm}$ which are larger than the heights obtained for the thiol immobilized pillar. The increased height can be attributed to the different immobilization method: while the thiol groups bind directly to the gold surface, the biotinylated pillars need an additional layer on the surface. The silica spacer is coated with biotinylated BSA and incubated with NeutrAvidin to which the pillars can bind. If the only difference between the T2 and B2 sample is the immobilization layer, we could estimate its thickness from our data. However, in Section 4.3.1 we found that the biotinylated pillars are tilted, which should result in a reduced height. The above mentioned correlation between lifetimes is an indicator for a tilt distribution, because the tilt would affect both heights and therefore lifetimes. The correlation is much larger than in simulations, so the fitting error does not explain the high correlation we observe here. It is also larger

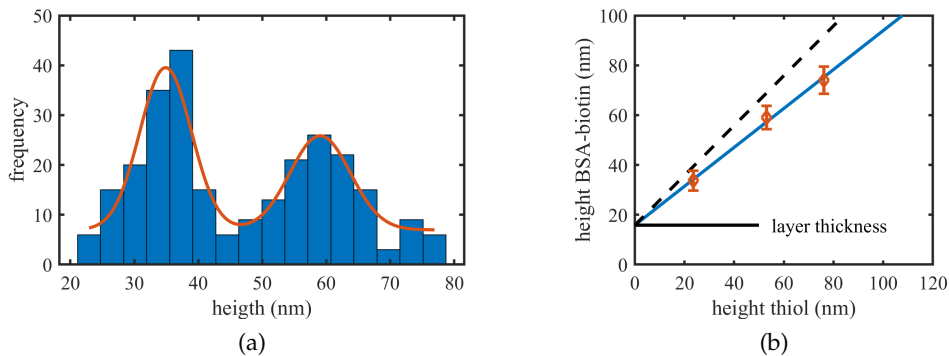


Figure 4.16: a) Height histogram of the biotinylated pillar. The heights obtained by the Gaussian fit are (59.0 ± 4.7) nm and (34.9 ± 4.0) nm. b) Estimation of the BSA-biotin-NeutrAvidin layer thickness and tilt angle. The weighted regression of the heights of B1 and B2 versus T1 and T2 gives a thickness of 15.8 nm and a tilt angle of 39° (blue line). The dashed line represents the case of no tilt.

than in the thiol sample, consistent with the hypothesis of tilt in the biotinylated sample but none (or less) in the thiol sample.

The distance distribution from co-localized emitters yields a distance of (25.0 ± 7.7) nm. Although the expected distance of 29.8 nm is within the error of the measurement, it shows a tendency to be underestimated. If we take the average tilt angle of 35° measured by 3D DNA-PAINT into account, the expected distance becomes 24.5 nm and is close to the measured value. In the next section we will combine the data with our results from the thiol immobilized pillar to estimate the BSA layer thickness and the tilt.

4.3.2.8 Estimation of Immobilization Layer Thickness and Tilt

The measured heights of the B2 sample are significantly higher than for T2 (cf. Table 4.4). On the one hand, we would expect an increase in height because we do not know the height of the BSA-NeutrAvidin layer below the pillar. On the other hand, we expect the biotin pillars to be tilted as measured by 3D DNA-PAINT, which would again reduce the observed height. Assuming the heights measured for T1 and T2 as ground truth and comparing them to the heights of the biotin sample, we obtained an estimate of the shift and the tilt. A weighted regression gave a layer thickness of 15.8 nm and a tilt angle of 39° (see Fig. 4.16a). If using the reference values calculated from the 3D DNA-PAINT experiment as ground truth instead, the values changed only slightly (15.1 nm and 38°). These estimates are comparable to literature values for BSA ($14 \times 4 \times 4$ nm³ for the dimer [117]) and NeutrAvidin (5.8 ± 1.8 nm [49]) and the average tilt angle of 35° measured by 3D DNA-PAINT. Ellipsometric measurements found that the layer thickness of BSA depends on the surface density as this will determine the orientation of the prolate BSA molecule in a mono-

layer. For dry films, Scarangella et al. reports a thickness of 4.5 nm after 1 h incubation with 0.5 mg/ml [118]. The thickness was found to vary between 3.1 nm (0.01 mg/ml) and 9.3 nm (2.5 mg/ml). Adding the size of the NeutrAvidin molecules of 5.8 nm gives a thickness of about 10.3 nm. For alternating layers of BSA and (poly)streptavidin in aqueous solution, a layer thickness of 18.75 nm was found by Spaeth, Brecht, and Gauglitz [119]. While the measurement on dry films by Scarangella et al. probably underestimates the film thickness compared to BSA in aqueous solution, the use of polystreptavidin by Spaeth, Brecht, and Gauglitz likely increases the thickness compared to NeutrAvidin.

About the origin of the tilt we can only speculate: One possibility is that the surface roughness leads to the tilt. However, our AFM measurement of a BSA-biotin coated surface suggest that the surface roughness is below 2 nm (see Section 4.2.1) which would be too small to explain the tilt angle of 35°. Another possibility is that not all of the eight biotin groups bind to the surface which could result in a tilt of the whole structure. The thiol immobilization binds to the gold surface directly, so it is reasonable to assume that enough binding partners are available for the thiol groups. Since this results in upright pillars, we speculate that the surface density of NeutrAvidin is so low that not enough biotin groups find a binding partner.

4.3.2.9 Discussion

In this section, we evaluated the results of pillars labeled with two emitters. With the step-wise bleaching approach, two emitters could be readily distinguished. We found that the bleaching time is inversely proportional to the lifetime, thereby facilitating the separation of the bleaching steps. With this assumption we created a simple theoretical model which showed that MIET protects the fluorophore from photobleaching. This means that a high energy transfer to the metal leads to later photobleaching of the emitter and also to an increased number of detectable photons before photobleaching. The T₂ data supported the model and showed an increase of detected photons of the low lifetime emitters of 9% or 40%, depending on how the number was estimated. This finding shows that MIET can facilitate techniques using step-wise photobleaching, and in turn makes step-wise photobleaching a good strategy for axial co-localization with smMIET.

The co-localization of two emitters could be demonstrated in the two-dimensional lifetime histogram which showed a single peak corresponding to the two emitter heights. The measured heights did not agree with the design values, but with the reference values calculated from the 3D DNA-PAINT experiment. This is consistent with the results for the single labeled pillars. The localization precision for the T₂ sample was below 5 nm which is comparable to the result for the single labeled pillar in spite of the more complex data analysis. Further-

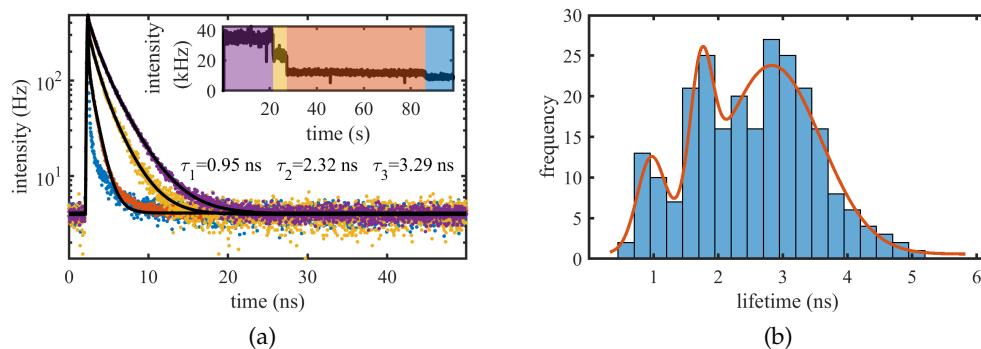


Figure 4.17: Measurement of the T₃ sample. a) TCSPC histograms of the background (blue) and the three bleaching steps as shown in the time trace in the inset. The TCSPC histograms of one emitter (red), two emitters (yellow), and three emitters (purple) are shown with their corresponding lifetime fits (black lines). b) Histogram of all fitted lifetimes before filtering.

more, we could resolve the intramolecular distance of about 30 nm on the single molecule level, again with a precision of 5 nm.

Furthermore, we checked the validity of the fitting and the analysis in a simulation. The fitting results indeed reproduced the simulated heights and distance. The precision of the fitting was about a factor 4 lower than the ideal case – comparing to the experiment, this would translate into a fitting uncertainty of about 0.1 nm. This is much smaller than the experimentally obtained uncertainty of about 4 nm, so other factors must be responsible for this. Not included in the simulations was the recognition of bleaching steps, the healing of blinking events, or the merging of states with similar lifetimes. All of these can contribute to the uncertainty in the analysis. Furthermore, the IRF was assumed to be known exactly, which is not the case for the experiment. Additional uncertainty is introduced by the sample variance, for example due to slight tilt, and is probably the main contributing factor.

In summary, we can localize two molecules with a precision of 5 nm and are not limited by our analysis, but probably mainly by the variance in the sample. In the next section, we go one step further and study multi-emitter co-localization of three emitters.

4.3.3 Multi-Emitter Co-localization of Three Emitters

A DNA origami pillar with three emitters with thiol immobilization (T₃) was designed to test the possibility for multi emitter localization. The sample was prepared and measured as described above. The designed heights correspond to the single labeled (82 nm) and double labeled samples (58 nm and 26 nm) discussed in the previous sections. Now we expect three bleaching steps and need to fit three lifetimes. An example can be seen in Fig. 4.17a.

279 point measurements were taken in total and 239 were used for lifetime fitting. A similar filtering procedure as before was employed: we exclude lifetimes that have the same value as the fitting parameter, where the lifetime is larger than 6 ns, the amplitude is smaller 5%, or the χ_{red}^2 value is larger than 2. By this procedure we excluded 172 lifetimes of the 554 in total. The resulting lifetime histogram is shown in Fig. 4.17b and feature three peaks as expected. The peaks seem to have very different amplitudes, especially the short lifetime peak at around 1 ns seems to be underrepresented. To be able to colocalize all three emitters simultaneously, we selected only molecules with three lifetimes. This reduced the number of molecules used for further analysis to 19.

To convert the lifetimes to heights, the MIET curve was calculated until 120 nm and heights are interpolated based on this curve. The heights were then sorted and the smallest, intermediate, and largest height of a pillar were separately histogrammed. A Gaussian distribution with offset was fitted to each histogram and the result is shown in Fig. 4.18a. Height estimates correspond to the mean and standard deviation of the Gaussian fits and are summarized in Table 4.6. The reference height was calculated as before from the 3D DNA-PAINT measurement. Within their errors, the measured values agree with the reference values. These heights can be used to calculate the height difference between the emitters and can be found in the upper part of Table 4.7 (method: loc.). This corresponds to the height difference of the ensemble rather than a single structure.

Intramolecular distances are measured within a single structure. Here, they are calculated by subtracting the sorted heights. These are histogrammed in Fig. 4.18b and fitted with Eq. (4.8). The estimated intramolecular axial distances are shown in the lower panel of Table 4.7 (method: co-loc.).

Compared to the T2 measurement, the errors of the estimates are much larger. This is probably due to the increased complexity of the fitting due to the higher number of fit parameters. The high correlation between the three heights (Pearson’s correlation coefficient of > 0.55 for all three) can be an indicator for errors due to the lifetime fitting or due to tilt of the sample.

| design height (nm) | reference height (nm) | measured height (nm) |
|-----------------------|--------------------------|-------------------------|
| 82 | 76.5 | 77.5 ± 8.1 |
| 58 | 54.1 | 55 ± 12 |
| 26 | 24.3 | 28.8 ± 4.7 |

Table 4.6: Heights of T3 pillars. The reference heights are computed from the design heights and the result of the 3D DNA-PAINT experiments.

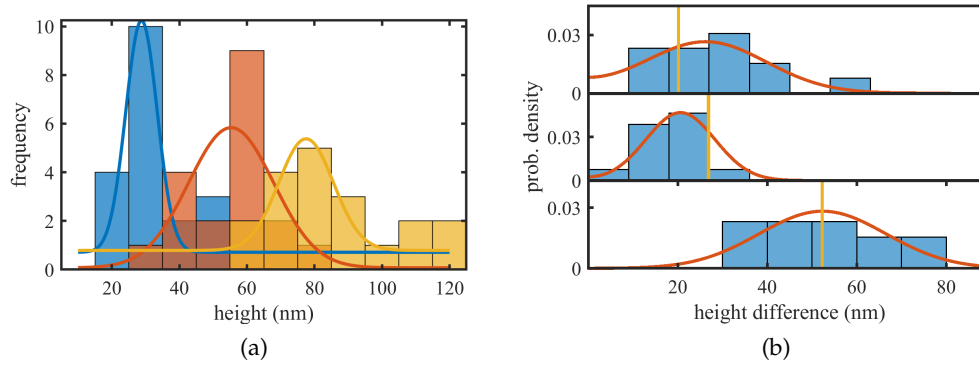


Figure 4.18: Localization of three emitters. a) Height histogram of the sorted height values of 19 molecules that showed three lifetimes. The smallest height is shown in blue, the second largest in red, and the largest height in yellow. Corresponding Gaussian fits are shown in the same color. b) Height difference histograms for the design distances of 24 nm (upper panel), 32 nm (middle panel), and 58 nm (lower panel). The reference distance is shown in yellow and a fit to Eq. (4.8) of the data in red. The fit results can be found in Tables 4.6 and 4.7.

4.3.3.1 Simulation

The simulation was carried out as described in Section 4.3.2.5 for two heights, but adding the additional height at 76.5 nm. From 1000 simulated experiments, 548 fulfilled the filter criteria as used in the experimental section and were subsequently used for the analysis. The height distribution was fitted by the sum of three Gaussian functions, yielding heights of (24.3 ± 0.4) nm, (54.3 ± 1.2) nm, and (75.8 ± 3.3) nm. These values agree with the simulated heights and the errors of the two lower heights agree with the results of the simulation for two emitters in Section 4.3.2.5. The standard deviations for the three heights were 1.7 nm, 3.9 nm, and 9.2 nm, respectively. These values were again higher than the Gaussian fits, and interestingly, they were even higher than in the previous simulation and thus probably due to the increased complexity of the fitting function. To test whether the three components of the fit influence each other, we calculated Pearson's correlation coefficient for all the possible pairs of estimated height. We found that the coefficient was lower than 0.2 in all cases. We speculate that only a subset is correlated, producing the long tails we observed in the simulated height distribution.

4.3.3.2 Discussion

In this section we studied a DNA origami pillar labeled with three emitters at different heights. The three heights of the sample could be well resolved and the height recovered within the error. Furthermore, the distance along the optical axis of the three emitters could be recovered using both localization and co-localization. However, the error

| design distance (nm) | reference distance (nm) | measured distance (nm) | method |
|-------------------------|----------------------------|---------------------------|---------|
| $82 - 58 = 24$ | 22.4 | 22 ± 15 | loc. |
| $58 - 26 = 32$ | 29.8 | 27 ± 13 | loc. |
| $82 - 26 = 58$ | 52.2 | 48.7 ± 9.3 | loc. |
| $82 - 58 = 24$ | 22.4 | 29 ± 15 | co-loc. |
| $58 - 26 = 32$ | 29.8 | 23 ± 9 | co-loc. |
| $82 - 26 = 58$ | 52.2 | 52 ± 14 | co-loc. |

Table 4.7: Summary of measured height differences for the T₃ sample. In the upper panel, the estimated heights (Table 4.6) were used to estimate the distance. The lower panel shows the result of the fit of Eq. (4.8) to the histograms in Fig. 4.18b. The reference values are computed from the design values and the 3D DNA-PAINT experiments.

is relatively large (about 10 to 15 nm) and the number of 19 analyzed molecules is small.

The simulation showed that the increased complexity leads to less usable data, i.e. while about 25% for the two dyes simulation were filtered, for three dyes the number of filtered fits was larger than 50%. A similar trend holds for the experimental data and is probably due to the decreased probability to find three well separated bleaching steps with enough photons. Furthermore, the average bleaching times are more similar than before. Assuming that the average bleaching time is proportional to the lifetime, we find that the average bleaching times of the two highest emitters only differ by about 50% whereas it is more than a factor of 2 for the two lower heights. Again, this reduces the chance to find a molecule with well separated bleaching steps. Additionally, the fit errors became larger, especially for the highest emitter. This is probably on one hand due to its short time until photobleaching, resulting in a low average photon number of about 5500 photons, and on the other hand because the fit error additionally depends on the two previously fixed lifetimes. This increased fit complexity however did not lead to a significantly higher correlation between the estimated heights in the simulation. Only in the experiment, the correlation was found to be much larger (0.55 compared to < 0.2). This might indicate some variability in the sample such as tilt, independent of the fitting errors.

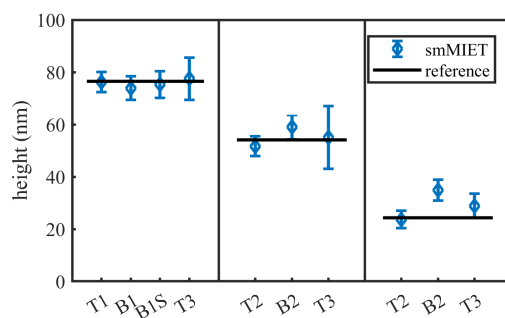


Figure 4.19: Summary of the smMIET experiments on the DNA origami pillar. The mean values of the emitter height is shown with the 1σ error for different samples (T/B: pillar immobilized via thiol groups or biotin-avidin; 1/2/3: number of dyes on the pillar; S: on silver, all other on gold). The black lines indicate the reference heights computed from an independent 3D DNA-PAINT experiment.

4.4 DISCUSSION

In this chapter, we explored how single molecule MIET can be used to measure distances on the nanometer scale along the optical axis. We used DNA origami nanostructures that were labeled with dyes at designed heights to perform the first single molecule MIET experiments in aqueous solution. The obtained heights agree with the reference values from an independent 3D DNA-PAINT measurement and reach a localization precision of about 5 nm. A similar precision was obtained for the samples with two dyes, also for the co-localized intramolecular distances. A summary of the axial localizations is shown in Fig. 4.19. The measured heights of the biotinylated pillars are larger due to the additional immobilization layer of BSA-biotin and NeutrAvidin for which we estimated a height of about 15 nm from our measurements, comparable to literature values as discussed in Section 4.3.2.8.

We applied our data analysis to simulated data and verified that the lifetime fitting is unbiased to ensure that the heights are accurate. Furthermore, we found that the parameters of the MIET curve calculation have a minor influence on the accuracy of our method compared to the statistical variation. However, the observed lifetime distributions were broader than the simulations suggested. Several factors could be responsible for the additional broadening:

- The dye Atto 647N introduced some complications by its photophysics. Its blinking events have to be distinguished from bleaching events, and different states of the emitter might even influence the lifetime. It is known that the dye Atto 647N exhibits different states due to isomerization that have a different lifetime [120]. In principle, these states will have different quantum yields as well which would require a separate analysis. From the raw data we are not able to distinguish between

the states, but since we know that the lifetime changes are small, we expect that this effect simply adds to the broadening of the measured lifetime distribution.

- A broadening is induced if the dipole of the emitter is not freely rotating. Atto 647N is not well water-soluble and thus might stick to the DNA origami or the surface. The influence of the orientation could be alleviated by combining the lifetime measurement with an orientation measurement. The orientation can be measured simultaneously to the lifetime either by defocused imaging [102] as proposed in Ref. [51] or by making use of the angular distribution of emission (cf. Section 2.4) and calculating the polar angle from the intensity of the high-angle and the low-angle emission as in Ref. [103]. The former method has the advantage that the emitter can be localized laterally as well and would allow localization in 3D. Alternatively, the orientation can be incorporated via modeling: It has been shown that a combination of FRET measurements with molecular dynamics simulation allows a direct comparison of the raw data with the simulation and improves the accuracy of the FRET distance distribution due to orientation effects [121]. This could also be applied to MIET experiments to increase the accuracy since it accounts also for restricted rotation which is difficult to measure.
- Additional broadening probably stems from tilt of the DNA origami structure which was also found in the 3D DNA-PAINT experiment. Because MIET measures the distance with respect to the surface, the orientation of the structure with respect to the surface normal is important. If the structure is immobilized on the surface in a specific orientation (as our DNA origami structure via thiol bonds), the interpretation of the heights directly relates to the axial distance on the structure. However, if the sample is randomly oriented on the surface, the measured heights will vary from molecule to molecule because MIET measures the projection of the 3D distance on the optical axis. It might be possible to reconstruct the 3D distance by back-projection which is commonly used in electron microscopy and tomography [122].

MIET exploits the distance-dependent energy transfer to a metal and is thus similar to FRET. However, MIET has some advantages in comparison to FRET: First, the orientation of the dyes plays a crucial role for the accuracy of FRET and it is not possible to measure the orientation factor independently of the FRET distance. In contrast to this, the orientation for MIET can be measured simultaneously as discussed above. Second, multi-distance measurements are possible with multi-pair FRET [123, 124], but are challenging due to the specific labeling of multiple positions with different dyes and the complex instru-

mentation and data analysis. For MIET, only a single type of label is needed and the setup can be a standard confocal microscope with the capability to measure fluorescence lifetime. We have demonstrated this by the co-localization of three emitters on the DNA origami pillar. In comparison to other near-field methods such as vaTIRF or SAF which are based on intensity measurements, MIET does not need instrument-specific corrections for cross-talk or background intensities. Furthermore, these methods are not able to resolve two emitters at the same time, limiting their applicability for intra-molecular distance measurements.

MIET can measure intra-molecular distances in a range of 100 nm with a precision of 5 nm. This bridges the gap between conventional 3D superresolution methods with an axial resolution on the order of 50 nm, and FRET with a sub-nanometer resolution but a limited range of 10 nm. The combination of MIET with lateral superresolution techniques would enable the measurement of 3D distances. With a beam splitter and a camera in the emission path, one could localize the emitter laterally. This can be combined with defocused imaging to measure the orientation of the dipole as discussed above, or with a superresolution technique such as STORM, PALM, or DNA-PAINT. As these methods multiplex the localization of several emitters in time, this would also reduce the complexity of the lifetime fitting when localizing many emitters. Alternatively, a method based on scanning could be used: A fluorescence lifetime scan image was recently used to localize single molecules in 3D using MIET [125]. For resolving intra-molecular distances, one could use a maximum-likelihood approach as in Ref. [126] to co-localize two emitters with different fluorescent lifetimes in a fluorescence lifetime image. Another scanning-based method is MINFLUX, a recently developed concept for localizing emitters [127]. Here, the measured intensity at different positions with a donut-shaped excitation PSF allows triangulating the emitter position. The scanning-based methods have the advantage that all detected photons can be used for the lateral and the axial localization, whereas the fluorescence intensity needs to be split in a combined wide-field/fluorescence-lifetime imaging setup. The combination of MIET with one of these techniques would be a step towards 3D isotropic imaging.

In summary, our experiments demonstrate that smMIET is able to resolve two emitters at 30 nm distance with a localization accuracy of less than 5 nm on a single DNA origami structure. This opens up new possibilities for resolving structures or structural changes in biomolecular complexes.

4.5 OUTLOOK – MIET WITH DNA-PAINT

In the current approach for co-localization with smMIET we used step-wise photobleaching to distinguish between different emitters. The main limitations of this method are the limited photon number and the need to fit a multi-exponential decay. Similar limitations are encountered in conventional superresolution techniques based on the localization of single molecules such as STORM or PALM. There, the number of photons limits the localization precision in a single frame and multiple emitters in a diffraction limited spot are difficult to fit [128]. DNA-PAINT can avoid those problems by decoupling the fluorophore from the label: The label is replaced by a short piece of single stranded DNA (docking strand) and complementary strands that are labeled with a dye (imager strands) freely diffuse in the solution. The transient binding and unbinding mimics the blinking (STORM) or photo-activation and bleaching (PALM). The advantage is that the binding kinetics is well known and thus can be easily tailored to the experiment. The applications of DNA-PAINT range from model systems such as DNA origami [79, 129] to whole cells [130]. Usually, a TIRF illumination is used to avoid collection of light from the imager strands in solution, but also a spinning disk confocal microscope has been used successfully [130].

A combination of DNA-PAINT with smMIET offers the advantage that the fluorescence from different heights is multiplexed in time. The transient binding of the imager strand leads to sparse events on the target molecule that can be detected by any burst search method. In contrast to photobleaching, this allows to label any number of different positions on a single structure and in principle collect as many photons as desired. Additionally, it avoids fitting multi-exponential decays which should increase the accuracy of the method. In order to be able to resolve two label positions, the fitting precision needs to be high enough. Long on-times are therefore desirable which can be achieved by using a long sequence for the docking and imager strands.

For a combination with MIET, the techniques must be compatible. Since MIET is based on the fluorescence lifetime, it requires that the dye's fluorescence decay is mono-exponential. In STORM or PALM, only a few labels show the desired blinking behavior and can be used for those techniques which makes it difficult to find a dye that satisfies the condition of MIET at the same time. DNA-PAINT, in contrast, works with almost any organic dye, so a dye can be chosen that is bright and has a mono-exponential decay.

4.5.1 *Proof-of-Principle Experiments*

We performed preliminary experiments on DNA origami pillars. The pillars were modified with DNA docking strands instead of dyes at

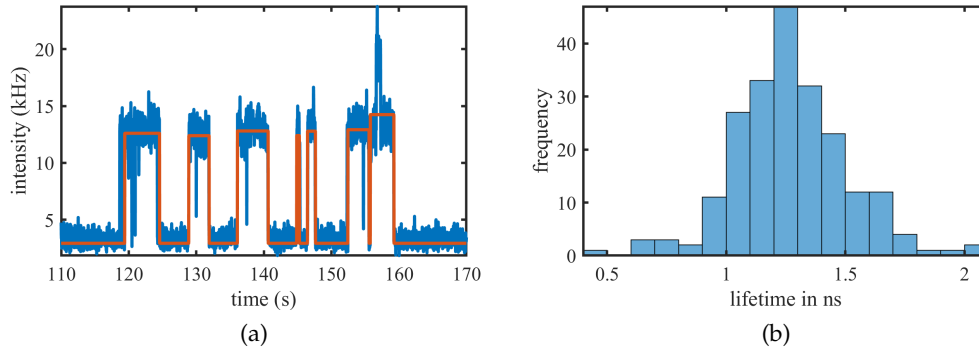


Figure 4.20: smMIET combined with DNA-PAINT. a) Time trace of binding events on a single pillar on a gold coated coverslip. The red curve shows the detected bursts. b) Lifetime histogram of 15 time traces combined containing 214 bursts in total.

the designed heights of 26 nm (three docking strands) and 36 nm (two docking strands). Multiple docking strands were used to increase the chance of binding. The complementary imager strand was modified with Atto 655. This dye was chosen as it does not stick to the surface and thus avoids events from unspecific binding and it is quenched by guanine in the imager strand sequence in solution which should reduce the background of the freely diffusing imager strands [131]. Additionally, Atto542 was attached to the pillar to be able to localize individual pillars independent of binding events. The pillars were immobilized on a gold coated coverslip with 10 nm silica spacer via biotin as before. The imaging buffer contained 10 – 20 nM of the imager strand. The sample was then scanned with 532 nm excitation to detect fluorescence from Atto542 labeled pillars. By bleaching the Atto542, aggregates could be identified as they would show multiple bleaching steps and thus could be avoided for the PAINT measurement. After confirming a single pillar, excitation was switched to 640 nm and a long point measurement was taken. We were able to observe single binding events to a single structure as shown in Fig. 4.20a. The imager strand concentration has to be chosen carefully as a low concentration decreases the binding rate, but a high concentration leads to increased background from diffusing imager strands and more frequent multiple binding events (which is also seen in Fig. 4.20a).

A time trace was calculated by binning the recorded photon events using a binwidth of 20 ms. In a histogram of the bins, the lowest peak was identified as background peak and fitted to a Poissonian with parameter λ_{bg} . The fitted value $\lambda_{bg} + 3\sqrt{\lambda_{bg}}$ was then used as a threshold to identify binding events in the time trace. For each of these bursts, the corresponding TCSPC histogram is fitted to obtain the fluorescence lifetime. We found that the background in addition to the well known two components (constant component and scattering component from gold luminescence) consisted of a third long

lifetime component (3 ns). This component stems from the freely diffusing imager strand in solution and roughly corresponds to the free space lifetime of Atto655 conjugated to DNA. For fitting the TCSPC histogram of a burst, this component was kept fixed and only its amplitude was fitted. We excluded fits that have less than 10^3 photons or a χ_{red}^2 value larger than 1.5. In this way, we obtained the lifetime histogram combining 15 time traces of single pillars shown in Fig. 4.20b. The distribution is relatively broad so that no clear peaks can be identified. It is most likely that the bad signal-to-background ratio of this measurement is responsible for this. While for the step-wise bleaching experiments the gold luminescence was the main background contribution, here it is the fluorescence of diffusing imager strands. The additional long lifetime component increases the uncertainty in the fit. Moreover, assuming that the lifetime is mono-exponential is a simplification. Although the MIET range of about 150 nm is small compared to half the extent of the confocal volume along z , about $0.5 \mu\text{m}$, diffusing dyes close to the surface will be quenched by the metal and contribute with a smaller lifetime.

The best strategy for improvement would thus be to minimize the contribution of imager strands by either decreasing the excitation volume or by chemically modifying the imager strand that it is completely quenched in solution. The former can be achieved by using a focused total internal reflection (TIR) illumination such as in Refs. [132–134] and the concept of the latter is also known as molecular beacons [135]. Both approaches will be the focus of further research.

In this chapter, a new method for dead-time correction of TCSPC systems is presented. Our method is based on asynchronous recording of photon arrival times as it is employed in modern TCSPC hardware. We developed a theoretical model for the TCSPC histogram distorted by the dead-time of the detector and the TCSPC electronics. Based on this model, we implemented an algorithm to correct dead-time artifacts in TCSPC histograms and verified the result by numerical simulations and experiments.

This chapter is based on the publication:

*Sebastian Isbaner*¹, *Narain Karedla*¹, *Daja Ruhlandt*, *Simon Christoph Stein*, *Anna Chizhik*, *Ingo Gregor*, and *Jörg Enderlein*. “Dead-time correction of fluorescence lifetime measurements and fluorescence lifetime imaging.” In: *Optics Express* 24.9 (May 2, 2016), pp. 9429–9445. DOI: [10.1364/OE.24.009429](https://doi.org/10.1364/OE.24.009429).

5.1 INTRODUCTION

Fluorescence microscopy has become a powerful tool in biology and bio-medical diagnostics [6, 7]. Fluorescence detection is highly sensitive and stands out due to its superior selectivity with which structures of interest can be labeled. In particular, multi-color fluorescence microscopy on differently labeled targets enables studying the relative structural organization and dynamics from organelles to molecules of living cells. The labels are often distinguished based on their spectral properties, i.e. their color or their excitation and emission wavelengths. A further means of disentangling different dyes in a fluorescence microscopy image is to use their fluorescence lifetime, see e.g. [136]. As with the spectral properties, which differ from dye to dye, also the fluorescence lifetime is different between different dyes and can be used to distinguish between them. Moreover, fluorescence lifetime measurements have become increasingly popular for the quantification of Förster Resonance Energy Transfer (FRET) measurements in bio-imaging [95, 137, 138], because they allow for accurate FRET rate estimates which are independent of intensity measurements that can be skewed by optical absorption, cross-talk, and scattering.

In this work, we consider a FLIM system which is based on a confocal scanning microscope [60] and uses TCSPC [33–35] for measuring the fluorescence decay at every scan position. In TCSPC, one determines the decay curve by exciting molecules with a periodic train of

¹ These authors contributed equally to this work.

short laser pulses, and then measuring the time delay between the recorded fluorescence photons and the exciting laser pulses. When building a histogram of these delay times, one obtains an estimate of the fluorescence decay curve which can be described with a single- or multi-exponential decay function. Modern TCSPC systems measure the arrival times of detected photons and the laser pulses independently from each other, thereby avoiding a preference for early photons which is known as the pile-up effect for classical TCSPC hardware [34]. Although TCSPC is a very efficient techniques, it only works at moderate count rates of a few percent of the laser repetition rate. This is due to the so-called dead-time of the electronics and the detector: After the successful detection (detector) or timing (electronics) of a photon, both detector and electronics need to recover and to return to an active state before being able to detect or record the next photon. These recovery times are typically on the order of tens of nanoseconds and limit the photon count rate at which the devices can operate. But even when the average time between photons is on the order of some percent of these dead-times, this leads to an increasing loss of detectable photons and to a distortion of the measured fluorescence decay curve.

The common rule-of-thumb is to operate a TCSPC system only at count rates below 1% of the laser repetition rate because then photon losses and distortions of dead-time effects are reduced. However, low count rates increase the time to obtain sufficient statistics for a fluorescence decay curve which in turn limits the image acquisition speed in scanning microscopy. In FLIM, at each scan position during the sample scan with a laser-scanning confocal microscope, one records a TCSPC curve from which not only the fluorescence intensity but also a lifetime value is extracted. For rapid FLIM image acquisition, one wants to maximize the count rate that should be limited only by photobleaching and phototoxicity, but not by potential dead-time effects in the TCSPC measurement. The demand for such fast FLIM systems has led to the development of dedicated TCSPC systems such as "FASTAC FLIM system" by the company Becker & Hickl or "rapid-FLIM" by PicoQuant which both are based on dedicated hardware with short dead-times. However, a data evaluation method that faithfully reproduces the correct fluorescence decay curve even at high count rates would also enable unbiased fast FLIM on existing setups without the need for dedicated hardware.

Here, we present a data evaluation method which provides dead-time corrected fluorescence decay estimates from TCSPC measurements at high count rates, and we demonstrate our method on FLIM of fluorescently labeled cells.

5.2 THEORY

5.2.1 *Distortion Effects in TCSPC Measurements*

In a TCSPC measurement, the arrival time of photons is measured with respect to an external sync source, usually provided by the pulsed excitation laser. For each detected photon, the detector produces a normed signal pulse which is timed by the TCSPC electronics. For the timing, different schemes exist that have been introduced in Section 2.3.2. Here, we will briefly recapitulate these schemes and discuss possible distortions at high count rates.

1. In (forward) start-stop TCSPC, the laser sync starts the timer and a photon detection event stops the timer. After the stop, there will be a certain dead-time of the timing electronics. The first laser sync after the dead time starts the timer again. This means that only the first photon in an excitation period can be recorded, so there is a preference to detect the “early” photons of the decay, also referred to as “classical pile-up” [31].
2. In reverse start-stop TCSPC, a photon detection event starts the timer and the next laser sync stops the timer. After the stop and the dead-time of the timing electronics, the next photon can start the timer anytime during the sync period. This leads to a lower detection probability in the beginning of the sync period, also referred to as “inter-pulse pile-up” [31]. An additional complication for such systems can be that the dead-time itself is variable: The timer in these systems usually works by charging a capacitor with a constant current so that the voltage is proportional to the elapsed time. Since the read-out involves discharging the capacitor, the duration of the dead-time depends on the start pulse and thus on the photon arrival time [31, 139].
3. A modern TCSPC system, such as described in Ref. [36], uses independent timers for the sync and detector pulses. Only when a photon is timed, the start-stop time is recorded as the difference of the detector timer and the sync timer. For sync periods longer than the dead-time it is thus possible to record more than one photon during one sync period.

In Fig. 5.1, the influence of the dead-time on these three systems is shown schematically. In this example, photons (circles) arriving at the TCSPC electronics which we assume has a constant dead-time after the stop. Although the arrival times of all photons is the same, the second photon recorded is different for the three TCSPC schemes.

The first two described TCSPC schemes have the limitation that they can detect only one photon per sync period. This leads to a preference to detect the early photons of the decay which results in the

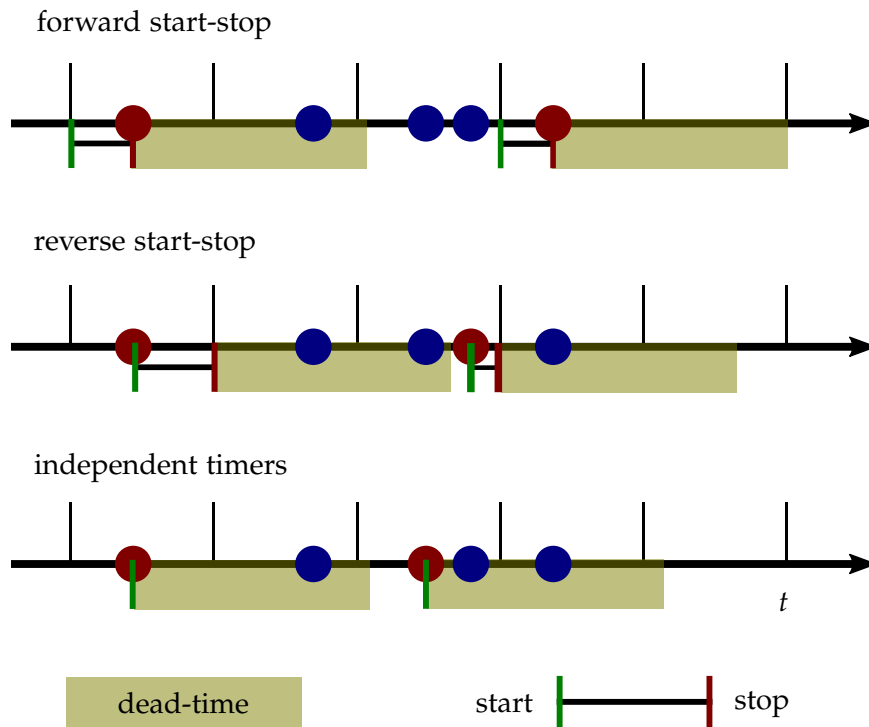


Figure 5.1: Dead-time effects in different TCSPC schemes. In forward start-stop TCSPC, the timer is started at each sync signal (black vertical bars) and stopped at the arrival of the first photon (red circles). Photons arriving during the dead-time or before the start of the timer (blue circles) are not recorded. In reverse start-stop TCSPC, the arrival of a photon starts the timer and the consecutive sync stops it. Photons arriving after the dead-time can immediately be recorded. Modern TCSPC hardware uses independent timers for the sync and the photons and has a constant dead-time. Note that the photon arrival times in all three cases are the same, but the second detected photon (red) is always different due to the different timing schemes.

pile-up effect [31]. Note that the pile-up effect is fundamentally different from dead-time distortions: Especially the classical pile-up of forward start-stop TCSPC does not depend on the dead-time and has been addressed in several publications, see for example Refs. [140, 141], and references therein. Reverse start-stop measurements suffer from pile-up as well as dead-time distortions [142]. An overview on different start-stop TCSPC architectures and their pile-up behavior is given in Ref. [143]. Note that the independent timing scheme avoids classical pile-up effects completely as the timing can be executed any-time during the excitation period as soon as the electronics is ready. However, dead-time effects still distort the recorded fluorescence decay curve as we will see in the next section. In the following, we will focus on TCSPC measurements with the recently developed new generation of counting electronics that use independent timers and have a constant dead-time [36].

Apart from the TCSPC electronics, also detectors have a dead-time (cf. Section 2.3.1). A general classification in the literature of detector dead-times are the two categories of paralyzable and non-paralyzable detectors [144]. In a non-paralyzable detector, any photons hitting the detector during the dead-time are simply discarded. The photon hit rate ϵ can be estimated from the count rate R of a non-paralyzable detector with dead-time D as $\epsilon = \frac{R_{\text{non-paralyzable}}}{1 - DR_{\text{non-paralyzable}}}$. This detector type reaches a constant count rate at saturation that is given as the inverse of the dead-time. The situation is more complicated in a paralyzable detector: There, each photon hitting the detector during the dead-time is not counted but restarts the dead-time. At high photon fluxes, a further increase in photons leads to a decreasing count rate until the detector is incapable to detect any photons at all. Assuming Poisson statistics for the number of photons hitting the detector, one finds $R_{\text{paralyzable}} = \epsilon \cdot e^{-\epsilon D}$. In contrast to the equation for non-paralyzable detectors, this equation can be solved for ϵ only implicitly, for example by iteration. A typical example for a paralyzable detector is a Geiger counter. Single-photon avalanche diodes (SPAD) that are actively quenched are an example of non-paralyzable detectors. After the detection of a photon by an electron avalanche, the bias voltage of the photo-diode is lowered so that no new avalanche can be produced (active quenching). When the bias is reset after the dead-time, the next photo-electron can again create a new avalanche which will trigger a new detection event. For TCSPC, SPADs are commonly employed as detectors. Because these detectors are most often actively quenched, we assume a constant, i.e. non-paralyzable dead-time.

In this section we have reviewed the dead-times of detectors and TCSPC electronics. Especially older TCSPC electronics has non-constant dead-times, but also detectors can have variable dead-times. Here, we will focus on the most recent generations of TCSPC electronics and detectors that both have a constant dead-time.

5.2.2 *Dead-time Effects on TCSPC Histograms*

After we have discussed dead-time effects on the recorded photons separately for the electronics and the detector in the last section, we focus now on the more realistic situation where the detector and the electronics are connected in series, so both dead-time can affect the measurement. The impact of both dead-times is schematically shown in Fig. 5.2. After each photon detection, the single-photon detector has to recover and is, during some dead-time D , unable to detect another photon. This detector dead-time of length D is symbolized by the small red rectangles in Fig. 5.2. In parallel, after timing a photon detection event, the timing electronics has also to recover, with dead-time E , before being able to record another photon detection event. This dead-time of duration E is symbolized by large green rectangles in Fig. 5.2. Typically, one has $E > D$, but in the case of $E < D$, the electronics recovers faster than the detector so that it will be always ready to time the next event from the detector. Then the problem reduces to a single dead-time problem which is a special case of the theory developed below.

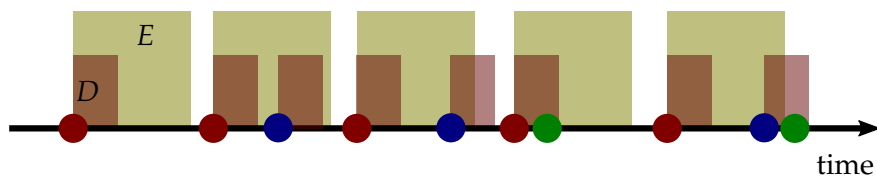


Figure 5.2: Schematic of possible effects of detector and electronics dead-time. A successfully detected and recorded photon (red circles) results in a dead-time of the detector (small red rectangles) and the electronics (large green rectangles). Photons detected during the electronics dead-time are not recorded (blue circles), and photons hitting the detector during the detector dead-time are discarded (green circles). Note that the detector dead-time occurs after successful detection of a photon (red and blue circles), while the electronics dead-time only occurs after successfully timing a photon (red circles).

Three scenarios for photons hitting the detector are now possible. In the best case, both detector and electronics are in their recovered resting state and can detect and record the photon (red balls in Fig. 5.2). Or, the detector has already recovered from the previous photon detection event, but the electronics is still in its recovery and not yet ready to record the detected photon (blue balls in Fig. 5.2). Or, in the worst case, the next photon hits the detector so closely to the previous one that the detector itself is still in its dead-time and cannot detect the photon (green balls in Fig. 5.2). It is important to notice that this can even happen while the electronics itself would be already capable to record another detection event (see the last event in Fig. 5.2 where the small rectangle, delimiting the detector dead-time, extends beyond the large rectangle, which delimits the electronics dead-time).

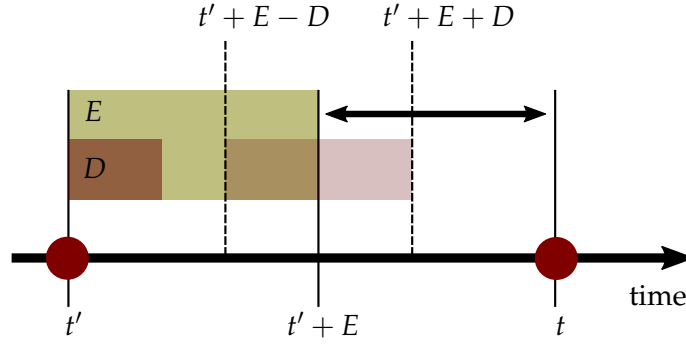


Figure 5.3: Schematic of two successive photon recording events. It shows the electronics dead-time (large green rectangle) and the detector dead-time (small red rectangle) after a successful photon detection at time t' . The double arrow is the time span between the end of the electronics dead-time by the last photon recording and the next photon recording at time t . The light red rectangle marks the region where no photon must be detected in order to record a photon between $t' + E$ and $t' + E + D$.

This is similar to the dead-time of a paralyzable detector as discussed in the previous Section 5.2.1. Although we assume the detector and the electronics to be non-paralyzable, their combination results in a semi-paralyzable system. As we have seen before, it is more difficult to estimate the count rate from paralyzable system. This is also the case for semi-paralyzable system as we will see later.

In the following, we give a probabilistic description of how these dead-times affect a recorded TCSPC histogram. We consider a TCSPC system which illuminates the sample with a train of short laser pulses with period P . Let us denote the resulting photon hit rate (number of photons per time hitting the detector) by $k(t)$. This function is periodic with period P , and its integral over one period is given by $\int_0^P dt' k(t') = \epsilon P$, where ϵ is the photon hit rate (which is equal to the average rate of detectable photons in one period if there would be no dead-time of neither detector nor electronics). However, due to the dead-time of both detector and electronics, the rate of actually recorded photons $h(t)$ is given by

$$h(t) = w(t)k(t) \quad (5.1)$$

where $w(t)$ is a weight function which accounts for the dead-time effects. To find this function, let us consult Fig. 5.3, assuming that there was a photon detection event at time t' . What is the chance to record the next photon at time t with no other photon recorded in between? If $t - t'$ is smaller than the electronics dead-time E , then this chance is zero. If $t - t'$ is larger than $E + D$ so that both electronics and detector have been fully recovered, then this chance is proportional to $\exp[-\int_{t'+E}^t d\tau k(\tau)]$, which is the probability that no photon hit the detector between the time of recovery of the electronics, $t' + E$, and the detection at time t . The situation is slightly more complicated if

$t' + E < t < t' + E + D$ because in that case, it is required that there was no photon hitting the detector for the full interval from $t - D$ till t , otherwise the detector would still be in its recovery phase when the next photon arrives at time t . Thus, for this case, the chance is proportional to $\exp[-\int_{t-D}^t d\tau k(\tau)]$. One has to multiply this factor by the probability density that there was indeed a photon recording at time t' , which is given by $h(t')$ itself. Thus, we arrive for the weight function $w(t)$ at the expression

$$w(t) = \int_{-\infty}^{t-E} dt' h(t') \exp \left[- \int_{\min(t'+E, t-D)}^t d\tau k(\tau) \right] \quad (5.2)$$

where we integrate over all possible recording times t' of the photon preceding the photon at time t . According to the lower bound of the inner integral, we break this into two parts and express the infinite integral as a sum over intervals of length P :

$$w(t) = \int_{t-E-D}^{t-E} dt' h(t') e^{-\int_{t-D}^t d\tau k(\tau)} + \sum_{l=0}^{\infty} \int_{t-E-D-(l+1)P}^{t-E-D-lP} dt' h(t') e^{-\int_{t'+E}^t d\tau k(\tau)}. \quad (5.3)$$

Taking into account the strict periodicity of all functions with period P , and that the integral $k(t)$ over one period is εP , a variable transformation $t' \rightarrow t' - lP$ for the inner integral of the second part leads to a geometric series, yielding

$$w(t) = e^{-\int_{t-D}^t d\tau k(\tau)} \int_{t-E-D}^{t-E} dt' h(t') + \frac{1}{1 - e^{-\varepsilon P}} \int_{t-E-D-P}^{t-E-D} dt' h(t') e^{-\int_{t'+E}^t d\tau k(\tau)}. \quad (5.4)$$

Equations (5.1) – (5.4) show a very intricate connection between the actual fluorescence decay curves, described by $k(t)$, and the recorded TCSPC curve, given by $h(t)$. These equations determine $h(t)$ via an integral equation involving the product of $h(t)$ and a kernel containing the unbiased decay function $k(t)$.

With Eqs. (5.1) and (5.4), one can now calculate the dead-time distorted curve $h(t)$ if the "true" decay curve $k(t)$ is known. One first sets $h(t) = k(t)$, then uses Eq. (5.4) for calculating $w(t)$, which can be used to update $h(t)$ via Eq. (5.1), which is then again used to calculate an updated $w(t)$ and so on. This iteration converges already after a few cycles, giving the correct shape of $h(t)$ up to some constant factor. However, the recursion cannot yield the absolute values of $h(t)$, because any re-scaling of $h(t)$ does not change Eq. (5.1). Figure 5.4 shows a Monte Carlo Simulation (MCS) of a TCSPC experiment with a single exponential decay (see Section 5.3), together with recursively

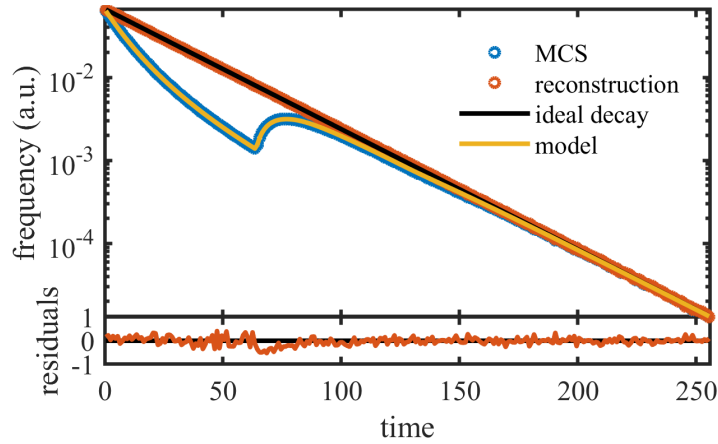


Figure 5.4: Monte Carlo Simulation (MCS, blue) of a TCSPC measurement with an excitation period $P = 256$, electronics dead-time $E = 64$, and detector dead-time $D = 16$. The photon hit rate ϵ was set to a value so that $\epsilon P = 2$, i.e. that, on average, two photons hit the detector per excitation cycle. The black line shows the underlying perfectly mono-exponential decay curve with a decay time of 30 time units. The yellow line is the computed $h(t)$ using Eq. (5.1) and (5.4) after 10 iterations. The dead-time corrected decay, as computed from the simulated $h(t)$, is shown in red. The lower panel shows the relative deviation of the reconstruction (red circles) from the ideal decay (black line), normalized by the square root of the ideal decay.

calculated $h(t)$ which is then linearly fitted against the simulated curve. The figure shows the perfect match between the *shape* of the MCS of $h(t)$ and that of its recursive computation using Eqs. (5.1) and (5.4). Furthermore, it can be seen that the dead-time effects considerably distort the recorded TCSPC curve, mimicking a much faster fluorescence decay at the high-intensity first part of the curve, much faster than the actual decay which underlies the measurement.

Unfortunately, Eqs. (5.1) and (5.4) cannot be used to recover $k(t)$ from a measured $h(t)$. The idea would be to first set $k(t)$ equal to $h(t)$, then to calculate $w(t)$ via Eq. (5.4), which can then be used to update $k(t)$ as $h(t)/w(t)$ following Eq. (5.1), and so on. However, as we have checked numerically, the result of this procedure depends sensitively on the value of ϵP which occurs in Eq. (5.4). If one tries to update this value via $\epsilon P = \int_0^P k(t) dt$, then the recursion does not converge. Only if this value is known *a priori*, then a recursion using Eqs. (5.1) and (5.4) converges to the correct curve $k(t)$. Thus, the next subsection focuses on how to independently determine ϵP from a measurement.

5.2.3 Determination of the Photon Hit Rate

As we have seen in the previous sub-section, the photon hit rate cannot be obtained from a measured TCSPC curve $h(t)$ and using

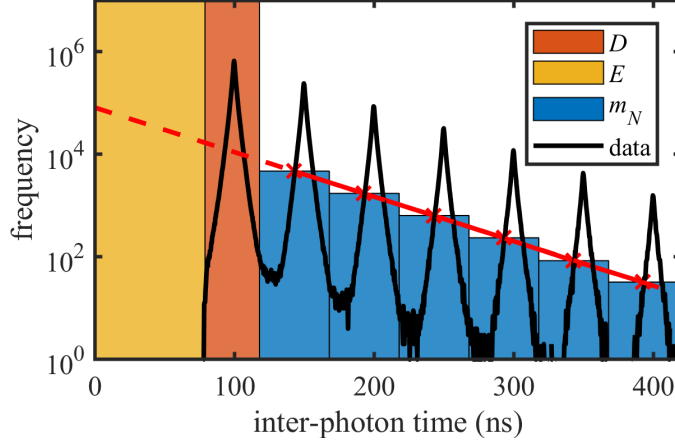


Figure 5.5: Measured histogram of the inter-photon time distribution (black solid line) extracted from a TCSPC measurement on a fluorescence dye solution. The yellow and red shaded regions on the left are the electronics and detector dead-time intervals, respectively. The cyan bars are the calculated values of m_N , Eq. (5.6), for $N = 0, \dots, 5$. The red dashed line shows the single-exponential decay of m_N . From this fit, we determined an average number of photon hits per excitation cycle of $\epsilon P = 1.0$.

Eqs. (5.1) and (5.4), even if the dead-time values E and D of both electronics and detector are known. However, by using the photon detection raw data, one cannot only calculate the TCSPC curve $h(t)$ by correlating photon detection times with the laser sync, but one can also calculate an Inter-Photon Time Distribution (IPTD) by building a histogram of the time differences of photon detection times between subsequent photons. An experimental example is shown in Fig. 5.5. Sure enough, the IPTD, which we will denote by $g(T)$, is zero if $T \leq E$, due to the electronics dead-time. If $T > E + D$, then the probability to detect a next photon at time $t + T$ if there was a detection event at time t is given by the probability of not detecting any photon between the end of the electronics dead-time, $t + E$, and the next photon detection at time $t + T$, times the probability density to see a photon at time $t + T$, i.e. $k(t + T)$. Due to the effect of the detector dead-time, if $E < T \leq E + D$, then this probability is given by the product of the probability of not detecting any photon between $t + T - D$ and $t + T$, and $k(t + T)$. Finally, for finding $g(T)$, one has to average the result over one excitation period with weight function $h(t)$. The result then reads

$$g(T) \propto \int_0^P dt h(t) \exp \left[- \int_{\min(E, T-D)}^T d\tau k(t + \tau) \right] k(t + T). \quad (5.5)$$

The important point now is that, if one sums $g(T)$ over subsequent time intervals $E + D + NP \leq T < E + D + (N + 1)P$ of width P , with N being any non-negative integer, i.e. by calculating

$$m_N = \int_{E+D+NP}^{E+D+(N+1)P} dT g(T) = C \exp(-N\epsilon P), \quad (5.6)$$

one finds that these integrals fall off as $\exp(-N\epsilon P)$, as also shown in Fig. 5.5. Thus, by fitting the m_N with an exponential function yields the average number of photon hits per excitation cycle, ϵP . Knowing this number, one can now use Eqs. (5.1) and (5.4) to recursively calculate the dead-time-corrected decay $k(t)$ from the measured decay $h(t)$.

5.2.4 Determination of Detector and Electronics Dead-times

For correctly recovering an unbiased decay curve from a measured TCSPC curve, one needs to know the electronics and detector dead-times, E and D . An elegant way to determine both values is to measure an autocorrelation function while illuminating the measurement system with a *continuous-wave constant-intensity* light source. This autocorrelation function $A(t - t')$ is proportional to the probability of recording a photon at some time t if there was a photon recording at time t' . If the light source has constant intensity (no time-dependence), the autocorrelation function depends only on the time difference $t - t'$.

For deriving a theoretical expression for the autocorrelation function, we will proceed in two steps. In a first step, we completely ignore the dead-time of the electronics and consider only the effect of the dead-time of the detector. Let us consider the probability density to record a photon at time t if there was a photon recording at time t' , but no photon recording in between. This probability density is zero if $t - t' \leq D$, and if $t > t' + D$, it will be proportional to $\exp[-\epsilon(t - t' - D)]$ which is the probability that no photon hits the detector between time $t' + D$ and time t . Here, ϵ is the constant average photon hit rate. Thus, the normalized probability density $f(t - t')$ for detecting a photon at time t if there was a detection event at time t' with no other photon detection in between is given by

$$f(t) = \begin{cases} 0 & \text{if } t \leq D \\ \epsilon \exp[-\epsilon(t - D)] & \text{if } t > D. \end{cases} \quad (5.7)$$

Next, let us consider the same probability density but now with exactly one intermediate photon recorded at any time t'' in between. This probability density is zero if $t - t' \leq 2D$, and is otherwise equal to the auto-convolution of $f(t)$, $\int_0^t dt'' f(t - t'')f(t'')$, computed

at time $t - t' - 2D > 0$. By repeating this argument for all possible numbers of intermediate photon recordings, one finds the following expression for the autocorrelation function $a(t)$ [145]:

$$a(t) = \sum_{j=1}^{\lfloor t/D \rfloor} f^{(j)}(t) \quad (5.8)$$

where $f^{(j)}(t)$ is the j -th auto-convolution of the function $f(t)$ which is recursively defined by

$$f^{(j)}(t) = \int_0^t dt' f(t') f^{(j-1)}(t - t') \quad (5.9)$$

and setting $f^{(1)}(t) = f(t)$. The upper limit in the summation (5.8) is the maximum possible number of photons which can be recorded within time t for a given detector dead-time D , where $\lfloor t/D \rfloor$ denotes the largest integer number smaller than t/D .

Now we are ready to consider the general case of both detector and electronics dead-time, assuming that $D \leq E$ (the case $D > E$ reduces to the just considered case of a system having only detector dead-time D). Analogously to the derivation of $a(t)$, we will again start by finding an expression for the normalized probability density $F(t - t')$ to detect a photon at time t if there was a photon detection at time t' but no other photon detection in between. Due to the electronics dead-time, this probability density is zero if $t - t' < E$. The interesting case now occurs if $t - t' > E$ but also $t - t' < E + D$. In that case, it can happen that a photon hits the detector shortly before the electronics recovers from its own dead-time so that no photon can be detected due to the detector dead-time although the electronics is again ready to process another detection event, see also Figs. 5.2 and 5.3. For this intermediate time interval, $E < t - t' < E + D$, the function $F(t - t')$ is proportional to the previously found autocorrelation $a(t - t')$ which is exactly the chance to be able to see another photon at t if there was one at time t' , when taking into account the detector dead-time alone. Finally, for time values t greater than $t' + E + D$, the probability density F will fall off exponentially as $\exp[-\epsilon(t - t' - D - E)]$, which is the probability that no photon hits the detector between time $t' + E + D$ and time t . In summary, we find

$$F(t) = \begin{cases} 0 & \text{if } t \leq E \\ Z^{-1}a(t) & \text{if } E < t \leq E + D \\ Z^{-1}a(E + D) \exp[-\epsilon(t - E - D)] & \text{if } t > E + D \end{cases} \quad (5.10)$$

where Z is a normalizing constant, and $a(t)$ is taken from Eq. (5.8). By a similar reasoning as before, the final autocorrelation function $A(t)$ is then found as

$$A(t) = \sum_{j=1}^{\lfloor t/E \rfloor} F^{(j)}(t) \quad (5.11)$$

where $F^{(j)}(t)$ is the j -th auto-convolution of the function $F(t)$, and the upper limit in the summation (5.11) is the maximum possible number of photons which can be recorded within time t when taking into account the electronics dead-time E .

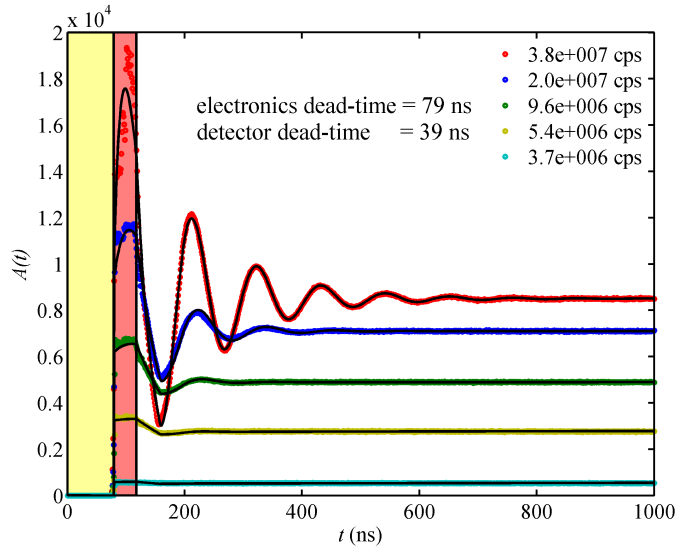


Figure 5.6: Autocorrelation functions for five different photon hit rates ϵ as indicated in the legend. Measured curves are represented by circles, solid lines show a global fit of Eq. (5.11) to all five measurements. The yellow and red shaded regions on the left mark the fitted electronics and detector dead-times, respectively. All autocorrelation functions were calculated at evenly spaced time points with 1 ns spacing. At very high count rates, fit quality starts to deteriorate due to increasing jitter of the detector dead-time. This figure was created by *Narain Karedla* and was reproduced from [146].

Thus, the calculation of the full autocorrelation function, Eq. (5.11) is as follows:

1. Calculate the function $f(t)$ according to Eq. (5.7) using known values of the detector dead-time D and the average photon hit rate ϵ .
2. Calculate $a(t)$, Eq. (5.8), via recursive convolutions of $f(t)$ according to Eq. (5.9).
3. Calculate $F(t)$, Eq. (5.10), using $a(t)$ and the known value of the electronics dead-time E .

4. Calculate the final autocorrelation functions $A(t)$, Eq. (5.11), via recursive convolutions of $F(t)$.

Although this may seem computationally expensive, it is not: The numerical calculation for one autocorrelation function with ca. 1000 sampling points along the time axis needs only a fraction of a second on a conventional PC and using a non-compiled *Matlab* script. Thus, it can be easily used for fitting measured autocorrelation curves and thus for extracting D , E and ϵ as fit parameters. An example for five different count rates is shown in Fig. 5.6, using our TCSPC system as described in Section 5.3.4 with the laser in continuous wave mode. The sample was a dye solution of Atto655 as described in Section 5.4.2. Autocorrelation curves of different count rates were fitted with a global model for E and D , but individual values for ϵP . From the fitted curves, we determined a detector dead-time of $D = (39.5 \pm 0.6)$ ns (red shaded region in Fig. 5.6), and an electronics dead-time of $E = (79.1 \pm 0.4)$ ns (yellow shaded region in Fig. 5.6). The errors were obtained by bootstrapping the data into 14 bunches of 10^6 photons each and calculating mean and standard deviation.

5.3 METHODS

5.3.1 *Monte Carlo Simulations*

Monte Carlo simulations of the TCSPC experiment were performed in the following way: First, for each excitation cycle, the number of hitting photons was randomly drawn from a Poissonian distribution with mean value ϵP . For each of these photons, the hit times with respect to the start of the corresponding excitation cycle were randomly drawn from an exponential distribution with decay time τ , where τ is the value of the mono-exponential fluorescence decay one wants to model. Knowing the excitation cycle and the hit time within this cycle for each photon, the global hit time is calculated for each photon, and then all these times are sorted in time. Then, the algorithm steps sequentially through these photon hit times and determines, for each photon, whether its hit time is still within the detector or electronics dead-time interval of the previous validated photon detection event. If this is the case, then the photon is eliminated from the photon stream, and the algorithm proceeds to the next photon. Finally, from the remaining photon stream, the TCSPC and the IPTD histograms are calculated.

5.3.2 *Software*

The software for the dead-time correction of fluorescence lifetime measurements used in this study is available for download¹. It is written in *Matlab* with core parts outsourced to C++ MEX files for performance acceleration, which can be compiled under Windows or Linux using the provided build scripts. The algorithm recovers the true photon hit rate $k(t)$ from the measured curve $h(t)$ in an iterative fashion, starting from the guess $k_0(t) = h(t)$. In a next step, $w_0[t|k_0(t)]$ is computed via Eq. (5.4), and is used to update $k(t)$ as $k_1(t) = h(t)/w_0[t|k_0(t)]$. This is repeated n times, until the relative change in $k_n(t)$ is smaller than a predefined threshold. It was observed that convergence is usually fast requiring only about 2 to 5 iterations.

5.3.3 *Setup for Cell Measurements*

For FLIM measurements, we used a setup based on a commercial confocal system (Microtime 200, PicoQuant, Berlin, Germany). Linearly polarized light from a 640 nm diode laser (LDH-D-C-640, PicoQuant, Berlin, Germany), equipped with a clean-up filter (Z640/10, Chroma Technology, Rockingham, VT, USA), was coupled into a polarization-maintaining single mode optical fiber. The laser driver (PDL 828 “Sepia

¹ at <https://projects.gwdg.de/projects/deadtimecorrectiontcspc>

II", PicoQuant, Berlin, Germany) allows for continuous wave (cw) or pulsed excitation mode of the laser (pulse width of 100 ps FWHM). For all lifetime measurements, we used the pulsed excitation mode with a repetition rate of 20 MHz. The light at the fiber output was re-collimated and reflected by a dichroic mirror (FITC/TRITC Chroma Technology, Rockingham, VT, USA) into the side port of an inverted microscope (IX71, Olympus Deutschland, Hamburg, Germany). An internal mirror reflected the beam into the back aperture of the objective (UPLSAPO 100× Oil, 1.4 N.A., Olympus Deutschland, Hamburg, Germany), which also collected the fluorescence light. After a 50 μm pinhole, the light was collimated and focused onto a single-photon counting module (SPCM-CD 3516 H, Excelitas Technologies, Wiesbaden, Germany). Back-scattered excitation light was blocked with a long-pass filter (EdgeBasic BLP01-635R, Semrock, Rochester, NY, USA). A single-photon timing electronics (HydraHarp 400, PicoQuant, Berlin, Germany) was used to record the detected photons with an absolute temporal resolution of two picoseconds. The sample was mounted on a three-axis piezo stage (P-562.3CD with controller E-710.3CD, both Physik Instrumente, Berlin, Germany), and image acquisition was performed using the SymphoTime software (PicoQuant, Berlin, Germany) in time-tagged, time-resolved (TTTR) mode. See Fig. 5.7 for a schematic of the setup.

5.3.4 *Setup for Solution Measurements*

For the solution measurements, the same setup as described in the previous section was used, but with a few modifications: We used a water immersion objective (UPLSAPO 60×W, 1.2 N.A., Olympus Deutschland, Hamburg, Germany) and a 150 μm pinhole and a band-pass filter (BrightLine HC 692/40, Semrock, Rochester, NY, USA). For data acquisition, the output of the detector was connected to an inverter (SIA 400, PicoQuant, Berlin, Germany) followed by the timing electronics (HydraHarp 400, PicoQuant, Berlin, Germany). There, events were recorded with 32 ps resolution with respect to the 20 MHz sync signal provided by the laser driver. The timing data was recorded with the original HydraHarp 400 software (version 3.0) in TTTR mode. For the measurement of the autocorrelation function, the laser was used in cw mode.

5.3.5 *Cell Culture and Staining*

Adult human mesenchymal stem cells from bone marrow (hMSCs, P4, Lonza, PT-2501), have been cultivated in T75 cell culture flasks (Corning, 43061) in DMEM (Gibco, A18967-01), 10% fetal bovine serum (Sigma-Aldrich, F2442-500ML) and 1% antibiotics (Penicillin/Streptomycin, life technologies, 15140-122) at 37°C and 5% CO₂ and split every 2–3 days (P₂→P₄). Then the cells were seeded on glass cover

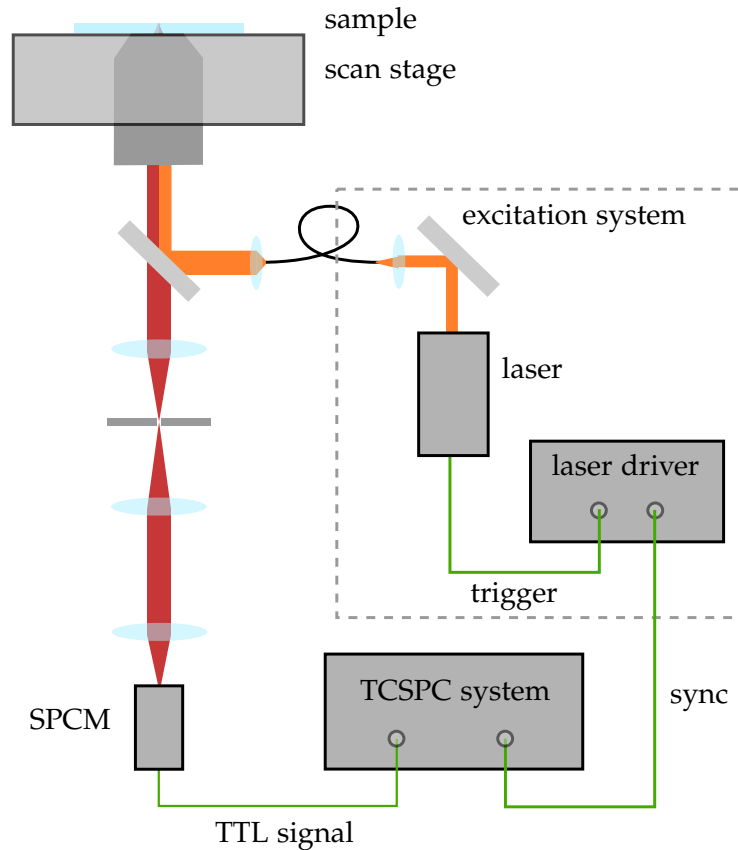


Figure 5.7: Setup for FLIM and solution measurements. The light of a pulsed laser (orange) is coupled into a fiber. The light is recollimated and reflected into the microscope by a dichroic mirror. The emission light is passed by the dichroic mirror and focused on a confocal pinhole, then recollimated and focused on a single-photon counting modules (SPCM). The detector is connected to the TCSPC system for recording the arrival times of photons. The laser driver which triggers the laser pulses provides the “sync” signal to the TCSPC hardware. This setup enables the measurement of the fluorescence lifetime. With the scan stage, the sample can be moved relative to the objective to record fluorescent lifetime images.

slides in a density of 10,000 hMSCs per glass in 6-well plates (Sarstedt, 83.3920). They were supplied with 2 ml medium per well at 37°C and 5% CO₂. The cells have been fixed 24 h after seeding using 10% formaldehyde in PBS for 5 min. The cells were permeabilised using 0.5% Triton X-100 in PBS for 10 min, blocked with 3% BSA in PBS for 30 min, incubated in Triton X for 5 min and washed with PBS. All antibodies were kept in 3% BSA in PBS. Fluorescent staining was performed with Phalloidin Atto 647N (Atto-Tec, AD647N-82) [1:250] for 1.5 h. The samples were mounted on microscope slides (VWR, 631-1550) using Fluoroshield mounting medium (F6182-20ML).

5.4 RESULTS

5.4.1 Numerical Simulation of Dead-time Correction

To check the performance of our algorithm of reconstructing an unbiased TCSPC curve from one with dead-time effects, we performed Monte Carlo simulations. All simulations were done with the same electronics and detector dead-time values as used for Fig. 5.4, and by assuming again a perfectly mono-exponential decay with a decay time value of 30 time units. It should be emphasized that the particular shape of the decay curve is irrelevant for the correction, because our algorithm will reconstruct an unbiased TCSPC curve whatever the underlying decay curve is, and it is independent of the particular nature of this decay. In the simulations, we assumed that the number of photons per sufficiently small time interval Δt centered at time t is described by a Poissonian probability distribution with mean value $k(t)\Delta t$. Simulations were performed for two values of total photon hits of 200 and 1000 photons, respectively, and for a range of average photon hits per excitation, ϵP , between zero and two. It should be mentioned that the actual number of *counted* photons, $\epsilon'P = \int_0^P dt h(t)$, becomes increasingly smaller, with increasing value of ϵP , than the number of total photon hits due to dead-time effects.

For each simulated experiment, we calculated the “measured” decay curve, $h(t)$, and the IPTD, $g(T)$, from which the values m_N were calculated, see Eq. (5.6). From these values, an estimate of ϵP was derived by fitting the m_N to an exponential function in N . This estimate was then used in the reconstruction of the dead-time corrected decay $k(t)$ from $h(t)$, using Eqs. (5.1) and (5.4). Finally, both $h(t)$ and $k(t)$ were fitted with a mono-exponential decay function for determining the decay time. For each pair of values of total photon hits and ϵP , we performed 10^4 simulations, and we then fitted the resulting decay-time distributions by Gaussians, for obtaining the mean value and variance of the decay-time estimation. The final result of these simulations is summarized in Fig. 5.8. It shows for both the raw and dead-time corrected decay curves the mean value and variance of the extracted decay-time value as a function of the average number of photon hits ϵP per excitation cycle. With an increasing value of ϵP , the dead-time distortion of the “measured” decay curve $h(t)$ leads to increasingly shorter apparent decay times. However, when fitting the dead-time corrected decay-curves, one finds perfect agreement, on average, between the fitted and the actual decay-time. Remarkably, the dead-time correction even works well for as few as only 100 to 200 photons per measured decay curve. Only the variance of the fitted decay-times becomes wider for smaller numbers of total photon counts, but no systematic bias in the decay-time estimate is showing up.

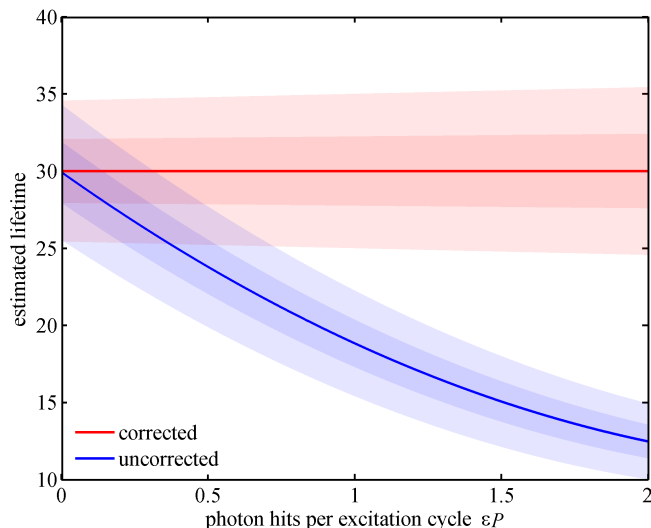


Figure 5.8: Results of Monte Carlo simulations of the performance of the recovery algorithm for dead-time corrected decay curves from measured TCSPC. Shown are the mean values (solid lines) and variances (shaded regions) of mono-exponential decay time values which are obtained from fitting the simulated decay curves. Simulations were performed for the same dead-time values as used in Fig. 5.4, for a range of photon hit values per excitation period, ϵP , from zero to 2, and for two different values of total number of photon hits, i.e. ϵP times number of excitation cycles, of 200 (light shaded region) and 1000 (dark shaded region). The corresponding decay curves have smaller number of photons, due to the dead-times of both electronics and detector. The figure was reproduced from [146].

5.4.2 Fluorescence Decay Measurements on Dye Solution

As a first experimental proof of principle of the validity and performance of our reconstruction algorithm, we recorded TCSPC data on a sample of a pure dye solution, where we changed, from measurement to measurement, the excitation intensity and thus the impact of dead-time effects. A thick dye solution (10 μM) of Atto 655 (ATTO-TEC, Siegen, Germany) in combination with a variable laser power was used to generate different photon hit rates ϵ . For very high photon hit rates ($\epsilon P \gtrsim 1$), buffer overruns were encountered after a few seconds, but during that time, a sufficiently large number of photons could be recorded. TCSPC histograms were constructed from the photon arrival times, examples are shown in Fig. 5.9a. For all histograms, we used bunches of 10^6 photons, and for the dead-time correction we used the *a priori* determined dead-time values $E = 79\text{ ns}$ and $D = 39\text{ ns}$. For each measurement, the parameter ϵP was estimated from the IPTD of photon arrival times, separately for each bunch. An example of a corrected TCSPC histogram is shown in Fig. 5.9b. Lifetimes were determined by tail-fitting, starting 1 ns after the peak of the decay curve, and using a mono-exponential fit function and

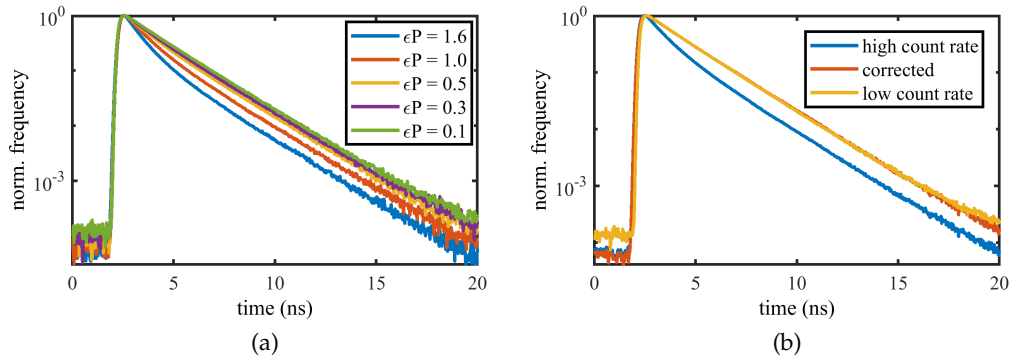


Figure 5.9: Measured TCSPC histograms of Atto 655 dye solution. a) Example TCSPC histograms measured at different count rates. The fluorescence intensity is given as photon hits per excitation cycle, ϵP , in the legend. At high values of ϵP , dead-time artifacts distort the decay curve. b) TCSPC histograms of a measurement at high count rate (blue), the same histogram after dead-time correction (red), and a different measurement of the same sample at a low count rate (yellow). All histograms were normalized to their maximum. The first 20 ns of the 50 ns repetition period are shown.

a simplex fitting routine. This procedure was repeated for ten consecutive bunches of 10^6 photons each, yielding an average ϵP and an average lifetime with standard deviation for each measurement, which are plotted in Fig. 5.10. As can be seen from this plot, the dead-time distortion effect leads to a decrease in fitted lifetime of the uncorrected histograms with increasing excitation rate, i.e. increasing number of photon hits per excitation cycle ϵ . The figure also shows that the dead-time correction results in fitted lifetime values which are unbiased and independent of ϵP , with an unbiased lifetime value of $\tau_{fl} = (1.902 \pm 0.005)$ ns (dashed line), in excellent agreement with published lifetime values of Atto 655.

5.4.3 Fluorescence Lifetime Imaging

We performed FLIM measurements of fixed human mesenchymal stem cells with actin filaments labeled with the dye Atto 647N. The sample was imaged with a sample-scanning confocal microscope using a 640 nm excitation laser and a long-pass filter before the detector. Results are shown in Figs. 5.11 and 5.12. Both the intensity and lifetime images are shown, with and without dead-time correction. In the image in Fig. 5.11, the uncorrected image shows a lower lifetime on average than the dead-time corrected image. The variation of the lifetime values in the uncorrected image is higher, with low lifetime values especially common in areas with a high number of photons. This correlation is expected for strong dead-time distortions as we have seen in Section 5.4.2. In the dead-time corrected image, the lifetimes show much less variation. The intensity image shows

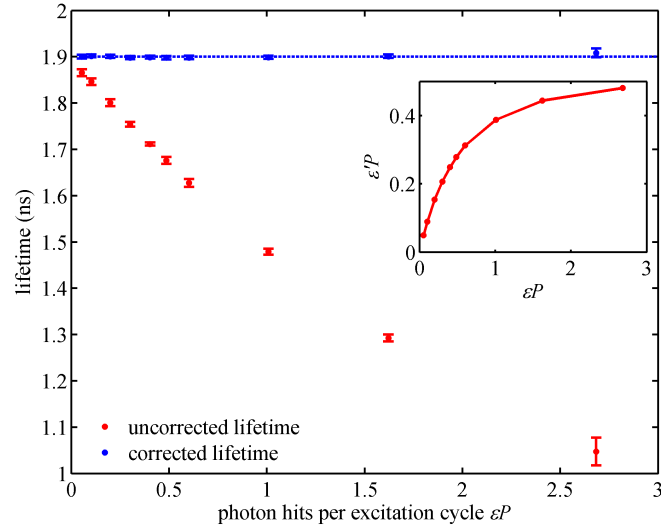


Figure 5.10: TCSPC measurements on Atto655 dye solution at varying excitation power and thus fluorescence intensity. The fluorescence intensity is given here as dead-time corrected values of average number of photon hits per excitation cycle, ϵP . The inset shows also the relation between the actual average number of detected photons per excitation cycle, $\epsilon'P$, and ϵP , showing the increasing dead-time related saturation of the measurement system with increasing intensity. Red symbols show determined lifetime values from uncorrected TCSPC curves, and blue symbols show lifetime values determined from dead-time corrected TCSPC curves. The dashed line shows the average over all lifetime values for all dead-time corrected measurements.

an increase in contrast with an increase in signal strength in areas with a high photon count in the uncorrected image. This can again be explained as the loss of photons due to dead-time at high count rates.

We verified the dead-time correction by recording an additional image at a six times lower laser power, leading to a lower count rate. The image in Fig. 5.12 was recorded with the maximum number of photon hits per excitation cycle well below 0.1. The image shows very little variation in the fluorescence lifetime and is similar to the dead-time corrected lifetime image recorded at a high count rate (Fig. 5.11). The dead-time corrected images of the low intensity measurement show only small changes compared to the uncorrected as we would expect for a low photon hit rate.

In the top row of Fig. 5.13, we show a line plot through the brightest pixel of Fig. 5.11. The pixels with highest intensity (top left) show a substantially lower lifetime in the uncorrected lifetime data (top right) due to dead-time distortion. This trend is not visible after the correction: the lifetime stays constant within the statistical error. This agrees with the results at low laser power (yellow curves in Fig. 5.13). Note that the variation in the lifetime is higher at low laser power

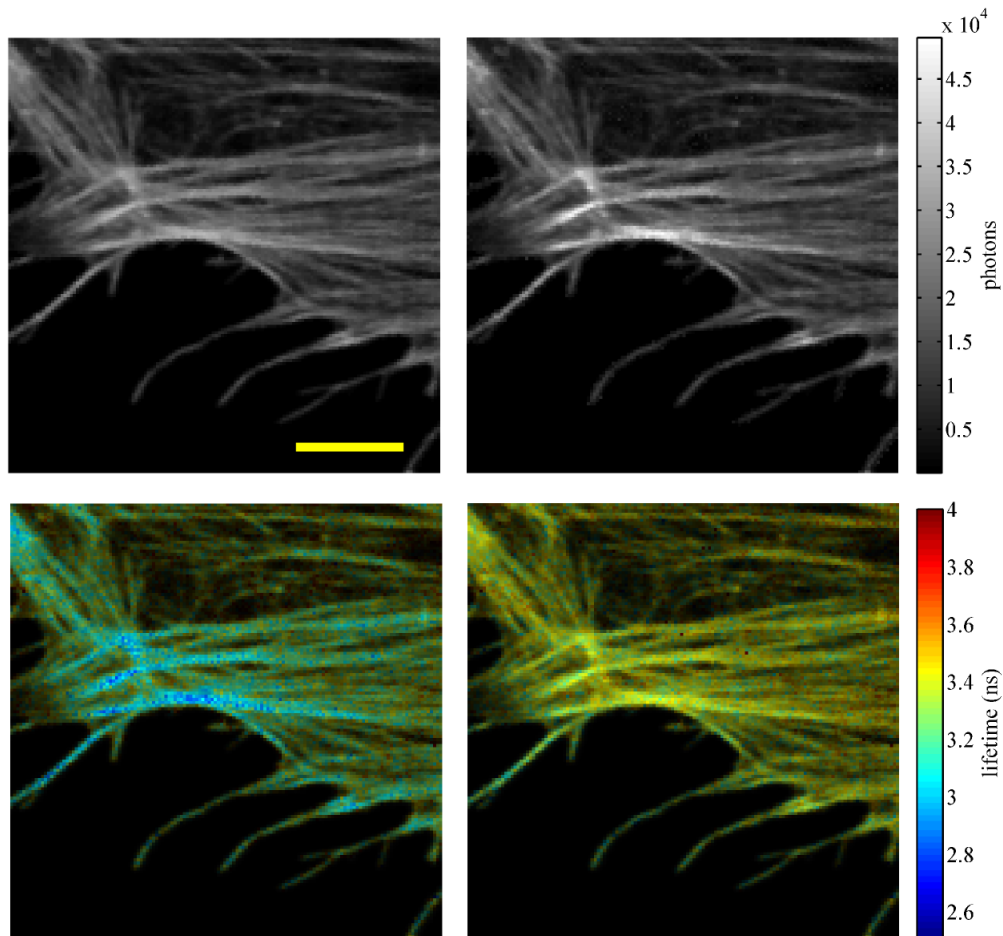


Figure 5.11: Human mesenchymal stem cell with actin filaments labeled by Atto 647N, and imaged with a confocal scanning TCSPC microscope. The top row shows the intensity image before (left) and after (right) dead-time correction, where the counts were determined using the calculated hit rates (ϵ) for each pixel. Regions with high fluorescence intensity show an increase in signal strength after the dead-time correction. The bottom row shows the lifetime images before (left) and after the dead-time correction (right). In regions of high intensity, the lifetime values in the left bottom image show a lower value than in low intensity regions. In the dead-time corrected image (bottom right), the lifetime values are higher on average and more homogeneous. The images are $20 \times 20 \mu\text{m}^2$ with a pixel size of 140 nm and a dwell time of 5 ms per pixel, the yellow scale bar is 5 μm . The highest number of photon hits per excitation cycle in this image is 0.5. This figure was created by *Narain Karedla* and was reproduced from [146].

compared to the corrected lifetime at high laser power because the number of recorded photons is smaller by about a factor of 5. If the lifetime was used, for example, to report on the FRET value, the dip in the lifetime curve (top right) can easily be misinterpreted as a significant change. In the bottom row of Fig. 5.13 we show the TCSPC histograms of the brightest pixel at high (bottom left, $\epsilon P = 0.50$) and low laser power (bottom right, $\epsilon P = 0.09$). The uncorrected and corrected TCSPC curves show a negligible difference for the lower photon hit rate which is not the case for the curves shown for the high ϵP value. The fitted lifetime values of the corrected curves agree within their errors, whereas the values differ substantially for the uncorrected curves.

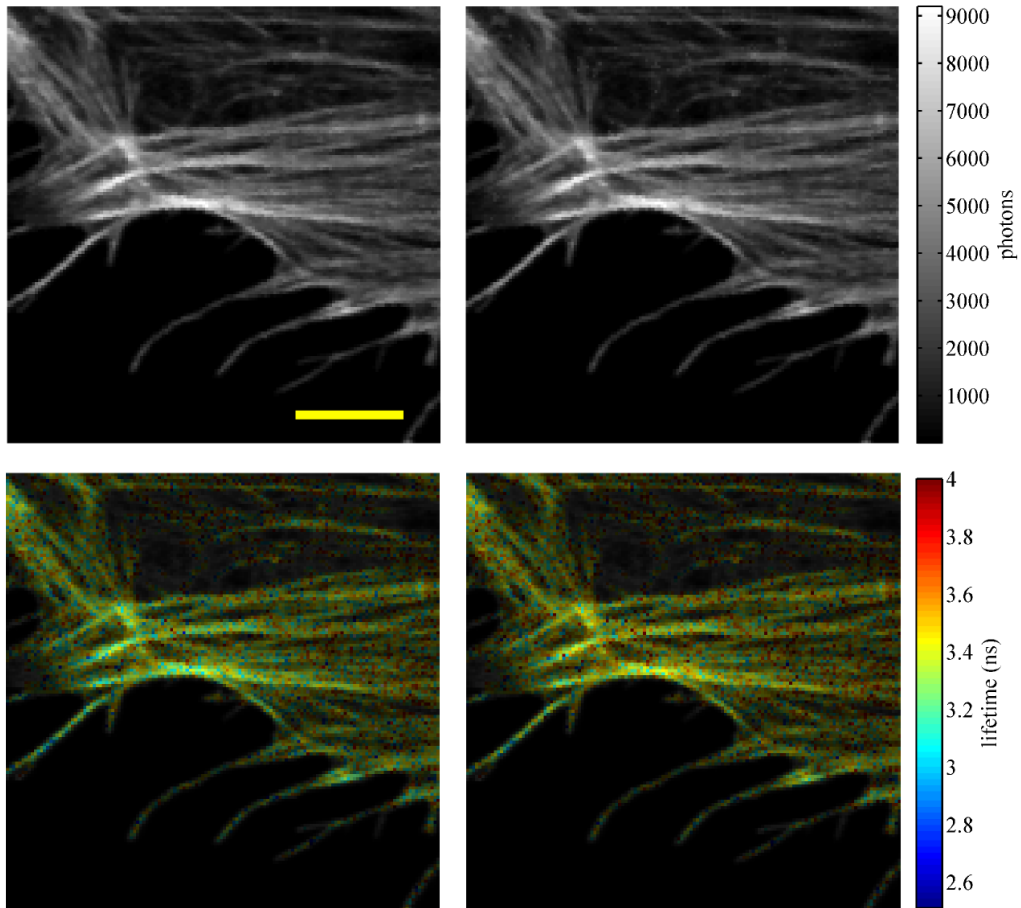


Figure 5.12: Image of the same sample as in Fig. 5.11, but using a six times lower excitation intensity. Now, the difference between the the dead-time corrected and the uncorrected images is small for both the intensity and the lifetime images. The lifetime images are close to the dead-time corrected lifetime image of Fig. 5.11. However, due to the lower fluorescence signal strength, the lifetime image is noisier than the dead-time corrected lifetime image in Fig. 5.11. This figure was created by *Narain Karedla* and was reproduced from [146].

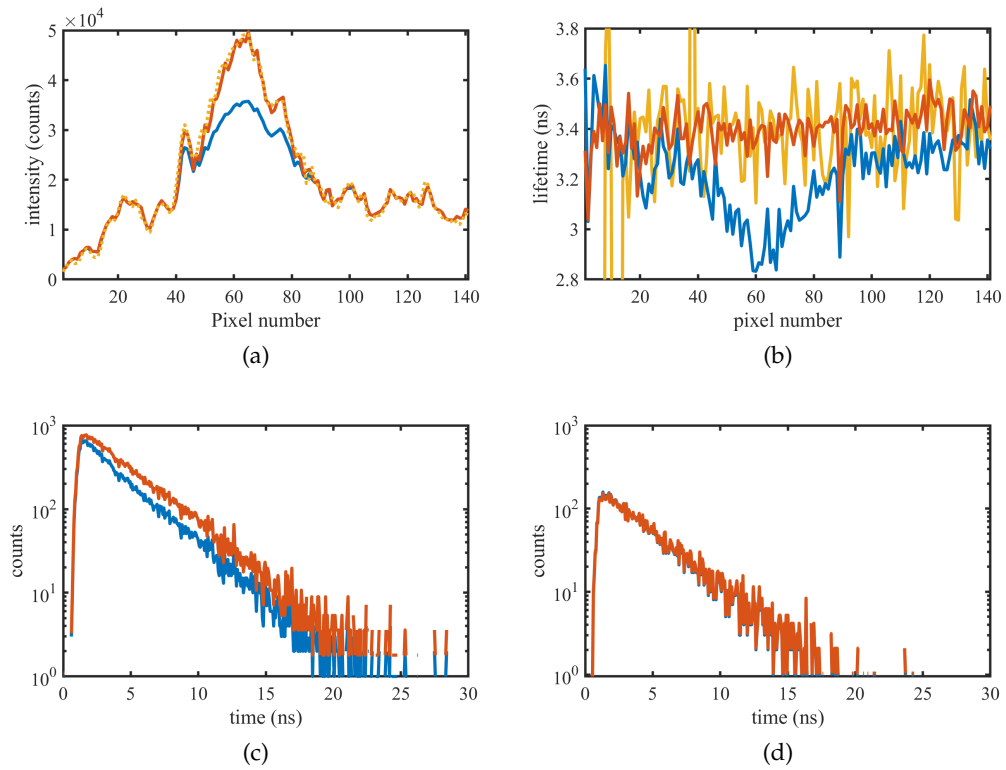


Figure 5.13: a) Line plot of the uncorrected (blue) and corrected (red) intensity through the brightest pixel of the cell measured at high laser power (Fig. 5.11). The dashed yellow line shows the intensity at low laser power multiplied by a factor 5.35. b) Lifetime plot of the same line as in a), showing the uncorrected (blue) and corrected (red) lifetime at high laser power, and the uncorrected lifetime at low laser power. c) The TCSPC curves of the brightest pixel ($\epsilon P = 0.50$) at high laser power with fitted lifetimes of $\tau_{\text{uncorrected}} = (2.87 \pm 0.02)$ ns and $\tau_{\text{corrected}} = (3.42 \pm 0.02)$ ns. d) TCSPC curve of the same pixel at low laser power (Fig. 5.12, $\epsilon P = 0.09$), yielding $\tau_{\text{uncorrected}} = (3.36 \pm 0.04)$ ns and $\tau_{\text{corrected}} = (3.47 \pm 0.04)$ ns. The blue lines represent always the uncorrected curves and the red lines the corrected curves.

5.5 DISCUSSION

In this chapter, we have investigated how dead-time effects distort a TCSPC histogram at high count rates and presented an algorithm that corrects these effects in measurements. We developed a theoretical model that describes the effects of constant detector and electronics dead-times and have verified the model with simulations and measurements of fluorescence lifetimes. The model was furthermore used to correct dead-time distorted TCSPC histograms of fluorescence decay and to estimate the actual photon hit rate from the data.

We measured the fluorescence lifetime of a dye in solution and of labeled cells to verify the correction algorithm and test its performance in lifetime measurements and FLIM. With the correction, the fluorescence lifetime of a dye solution was accurately reproduced up to a photon hit rate of more than 2 photons per excitation cycle ($\epsilon P = 2$). In the uncorrected measurement, the lifetime was underestimated by more than 50 % and the fluorescence intensity by a factor of 4. In the FLIM images recorded at high laser power, we found similar distortions that affected the lifetime accuracy and the image contrast. This can have serious consequences on the interpretation of the data: In FRET measurements in cells for example, a region with lower lifetimes could be wrongly interpreted as increased FRET although the real reason was dead-time distortions because the particular region had a higher labeling density than its surrounding. With the correction, the measurement can be performed at a high count rate without compromising the data accuracy.

Dead-time distortions in FLIM images are usually avoided by keeping the count rate low. A typical rule of thumb is that the count rate should not exceed 1 % of the laser repetition rate [34]. However, this reduces the measurement speed as more time is needed to acquire a sufficient number of photons. Because the dead-time correction allows imaging at a much higher count rate, it allows to speed up the image acquisition. We have successfully performed measurements at $\epsilon P = 2$, which increases the photon hit rate by a factor of 200 compared to the rule of thumb of $\epsilon P = 0.01$. However, this does not translate in a speed up of $200\times$, because most of the photons are lost and do not contribute to the photon statistics of the measurement. For a realistic speed up for FLIM we need to consider the real count rate $\epsilon'P$ instead of ϵP , so that the number of photons that can be used for the lifetime estimation is the same. We achieved a realistic count rate of about $\epsilon'P = 0.4$, i.e. a realistic speed-up of $40\times$. This enables fast FLIM measurements which, for example, can be used to increase the frame rate of FLIM. Further, the speed-up makes it feasible to scan a vast number of samples for high-throughput applications.

The dead-time correction can be useful also for other measurement techniques apart from FLIM. The algorithm does not depend, in any way, on the particular nature of the underlying fluorescence decay.

This enables the correction of multi-exponential decays as well as time-of-flight measurements which are employed for lidar [28] or in particle physics [144]. In addition to restoring the shape of the decay curve, also the intensity can be recovered. This increases the contrast of FLIM, but could be beneficial also for time-resolved fluorescence anisotropy measurements [24]. The algorithm is furthermore not restricted to TCSPC measurements, but applicable to any single-event counting or timing measurement of two devices with constant dead-time connected in series.

We have shown that our dead-time correction algorithm recovers the fluorescence lifetime and intensity from measurements at high count rates. It can be applied to any event counting technique with detector and electronics dead-time, and, thus, enable accurate measurements at high count rates. This allows faster data acquisition for high-throughput applications or for a better time resolution of consecutive measurements.

CONCLUSION

In this work, we investigated three methods that extend the resolution of a fluorescence microscope in different directions.

In Chapter 3, we showed how image scanning microscopy (ISM) can be used to increase the lateral resolution of a confocal spinning disk setup. To this end, no modifications on the optical path of the microscope were necessary. We developed a μ Manager plugin to control the synchronization of the spinning disk rotation with the illumination which will be freely available. The CSDISM resolution improvement is comparable to other ISM based methods in the literature [65, 67–69], while maintaining a low complexity of the setup. In fact, it is easily possible to upgrade existing confocal spinning disk systems to a CSDISM system.

In Chapter 4, we used metal-induced energy transfer (MIET) to colocalize single emitters on a DNA origami structure along the optical axis. The axial resolution of most fluorescence microscopy methods is lower than the lateral resolution. This is especially true for conventional superresolution methods like STED, STORM, or PALM which achieve a lateral resolution below 20 nm. With MIET, we resolved two emitters 30 nm apart from each other and measured their intramolecular axial distance with 5 nm precision. MIET offers a range of more than 100 nm which is an order of magnitude larger than the distances accessible by FRET. Thus, MIET can be used to study the structure of large biomolecular complexes that are too large for FRET yet too small for conventional (lateral) superresolution microscopy. Furthermore, the range and sensitivity of MIET can be tuned by choosing different materials such as indium tin oxide, enabling measurements with sub-nanometer accuracy [147]. The combination with a lateral superresolution technique can enable 3D imaging with an isotropic resolution of a few nanometers. This would allow to measure intramolecular distances with unprecedented resolution and open a new chapter in the field of structure determination of biomolecular complexes.

In Chapter 5, we developed a dead-time correction that can be used for fast FLIM imaging. We estimated that a speed-up of $40\times$ is possible which drastically increases the data acquisition speed. This allows high-throughput applications of FLIM [148] or to increase the frame rates to follow fast processes in cells. Apart from FLIM, the correction algorithm is applicable to other TCSPC based techniques such as lidar or fluorescence anisotropy. In fact, the model of dead-time effects can be applied to all single event counting devices with a constant electronic and detector dead-time. Apart from correcting the TCSPC

CONCLUSION

histogram, also the intensity is estimated. This might be interesting for counting based method to measure radiation in particle and high-energy physics.

In conclusion, we have presented the increase of the lateral resolution of a fluorescence microscope by CSDISM, the increase of the axial resolution by MIET, and the possibility to increase the time resolution (in terms of the frame rate) of a FLIM microscope by correcting dead-time distortions that limit the frame rate. In addition to the resolution improvement, the three methods have the advantage that they require standard instruments with little to no additional hardware, making them accessible for many researchers: For the dead-time correction, any TCSPC-based FLIM microscope can be used. MIET requires a standard FLIM microscope as well and metal-coated cover slips on the sample side. For the CSDISM, an existing CSD setup can be upgraded with an FPGA card and then used with our software. We hope that this accessibility enables many researchers to make use of these techniques and facilitate new discoveries.



OTHER CONTRIBUTIONS

Apart from the work presented in this thesis, I have contributed to three other publications during the course of my PhD:

Thilo Baronsky, Daja Ruhlandt, Bastian Rouven Brückner, Jonas Schäfer, Narain Karedla, *Sebastian Isbaner*, Dirk Hähnel, Ingo Gregor, Jörg Enderlein, Andreas Janshoff, and Alexey I. Chizhik. “Cell–Substrate Dynamics of the Epithelial-to-Mesenchymal Transition.” In: *Nano Letters* 17.5 (May 10, 2017), pp. 3320–3326. DOI: [10.1021/acs.nanolett.7b01558](https://doi.org/10.1021/acs.nanolett.7b01558),

Arindam Ghosh, *Sebastian Isbaner*, Manoel Veiga-Gutiérrez, Ingo Gregor, Jörg Enderlein, and Narain Karedla. “Quantifying Microsecond Transition Times Using Fluorescence Lifetime Correlation Spectroscopy.” In: *The Journal of Physical Chemistry Letters* 8.24 (Dec. 21, 2017), pp. 6022–6028. DOI: [10.1021/acs.jpcllett.7b02707](https://doi.org/10.1021/acs.jpcllett.7b02707),

and

Shama Sograte-Idrissi, Nazar Oleksiievets, *Sebastian Isbaner*, Mariana Eggert-Martinez, Jörg Enderlein, Roman Tsukanov, and Felipe Opazo. “Nanobody Detection of Standard Fluorescent Proteins Enables Multi-Target DNA-PAINT with High Resolution and Minimal Displacement Errors.” In: *Cells* 8.1 (Jan. 10, 2019), p. 48. DOI: [10.3390/cells8010048](https://doi.org/10.3390/cells8010048).

On the following pages, I will give a short summary of each of these projects.

A.1 CELL-SUBSTRATE DYNAMICS OF THE EPITHELIAL-TO-MESENCHYMAL TRANSITION

In this work, we studied the dynamics of the cell-substrate distance during the epithelial-to-mesenchymal transition. Epithelial cells are highly polar cells and connect to each other to form epithelial sheets. These cells can become migratory mesenchymal stem cells which can differentiate into a variety of other cell types. This process of changing the phenotype is called the epithelial-to-mesenchymal transition (EMT) and is important in embryogenesis, fibrosis, wound healing, and cancer progression. In contrast to the epithelial cells, mesenchymal stem cells lack polarization and are usually widely dispersed. Therefore, the EMT is accompanied by changes of the dynamics of cell-cell and cell-substrate interactions. Two phases of the EMT have been described: During the *transitional state I*, cells show an increase in cell-substrate dynamics for 4-9 h. In the following *transitional state II*, cell adhesion leads to an increase and suppression of the fluctuations due to the complete loss of cell-cell contacts. However, a precise picture of the process on a cellular or even subcellular level is lacking due to limited spatial resolution especially along the optical axis.

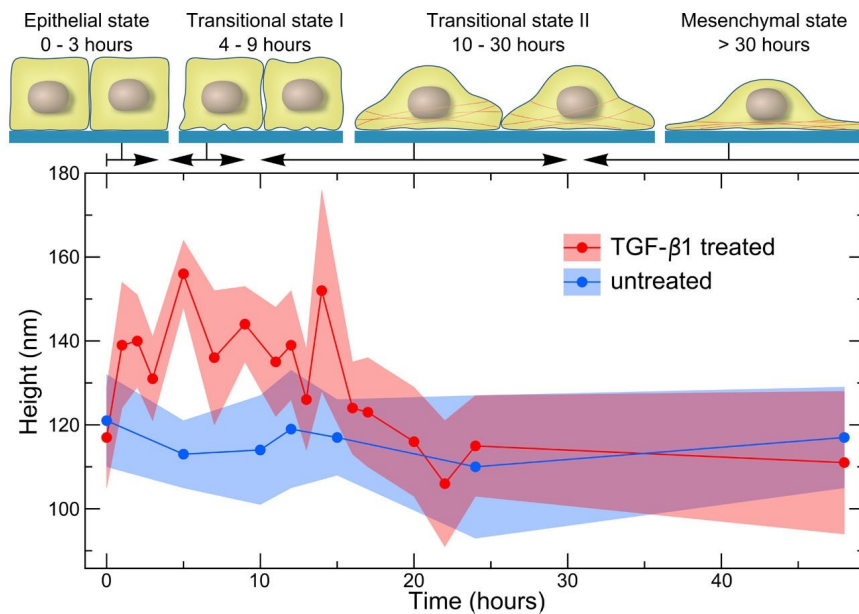


Figure A.1: Cell-Substrate Dynamics of the Epithelial-to-Mesenchymal Transition. In the graph, the average cell-substrate distance is shown for untreated (blue) and TGF- β 1 treated cells (red). The height initially increases by more than 20 nm when EMT is induced by TGF- β 1. The height is restored about 20 h after the treatment. Above, schematic drawings of cells show the ordered epithelial state, the transitional state I with dissolution of cell-cell contacts, the transitional state II where cells adhere to the substrate by forming actin stressfibers (red lines), and the mesenchymal state where cells are fully spread. The figure was reproduced from Ref. [149].

Here, we used metal-induced energy transfer (MIET) to follow the dynamics of the cell-surface distance. MIET allows to measure the distance of the basal membrane to the surface with about 3 nm accuracy. We used the transforming growth factor- β 1 (TGF- β 1) to induce the EMT in NMuMG cells, and then measured the height of the basal membrane above the surface at different stages of the EMT. Our results show that the cell-substrate distance increases during the initial stage of the EMT (see Fig. A.1). We found that this is accompanied by a reduction in the number of focal adhesion points which enables the cells to lift-off from the surface. Then, the cell-substrate distance decreases again until the initial distance is restored. We propose that during EMT, the cells enter a state of increased vertical motility due to dynamic remodeling of adhesion sites. This state is transient and the mesenchymal cells eventually become quiescent again, assuming the smaller cell-substrate distance is an indicator of higher adhesion forces.

In conclusion, the MIET measurements enabled us to follow the cell-substrate dynamics of NMuMG cells undergoing EMT with unprecedented resolution. Our findings will help to better understand cellular remodeling processes associated with wound healing, embryonic development, cancer progression, or tissue regeneration.

A.2 QUANTIFYING MICROSECOND TRANSITION TIMES USING FLUORESCENCE LIFETIME CORRELATION SPECTROSCOPY

In this work, we measure fast photophysical transitions within a fluorescent protein which allows new insights into its complex photophysical dynamics. Many fluorescent proteins are complex emitters and have more than one emission state. These states are often attributed to local charge density fluctuations in the vicinity of the chromophore, for example via the interaction of hydrogen bonds or amino-acids with the chromophore. Conformational changes such as amino-acid rotations or rearrangements have been also observed in X-ray crystal structures. Although these states differ in their excitation and emission spectra, they are difficult to resolve because the differences are small compared to the thermal broadening of the spectra at room temperature. The excited state lifetime provides an alternative means to probe the different states. Rapid switching between emitting states leads to fluctuations in the excited state lifetime. However, the ability to measure lifetime fluctuations with TCSPC are severely limited by the count rate of a single emitter which are on the order of $10^3 - 10^4$ Hz. Here, we used a correlation-based analysis to study the lifetime fluctuations: Fluorescence lifetime correlation spectroscopy (FLCS) enables the calculation of intensity correlation functions for a specific lifetime. This is achieved by statistically unmixing the intensity contributions of a mixture of emitters with different fluorescence lifetimes.

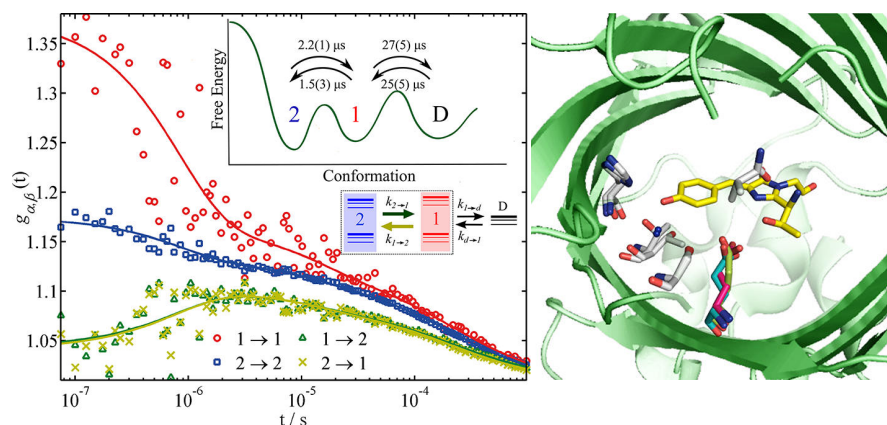


Figure A.2: Quantifying Microsecond Transition Times Using FLCS. Auto- and cross-correlation functions for the two EGFP states **1** and **2** are shown together with their fits (solid lines). The measurement was performed in solution at pH 6.0. The inset shows the proposed model of switching between the two states and a dark state **D** together with the measured switching times. On the right, the crystal structure of the inside of the β -barrel of EGFP with the chromophore in the center is shown. The interaction of the chromophore with a neighboring amino-acid residue that undergoes rotational isomerization induces the microsecond fast switching. The figures were reproduced from Ref. [150].

Here, we studied the emission states of the enhanced green fluorescent protein (EGFP). This protein is widely employed in fluorescence microscopy to label biological structures of interest and is known to exhibit two bright states and a dark state. From the FLCS measurement, we extracted the transition rates between the three states as shown in Fig. A.2. The switching between the bright states was on the order of microseconds, whereas the transition to the dark state was an order of magnitude slower. The transition rate to the dark state has been measured by ordinary fluorescence correlation spectroscopy (FCS) before, but we showed that the transition rate estimated from an FCS measurement is biased if there is an additional, fast switching between bright states as for EGFP. Furthermore, we measured the emission and excitation spectra of EGFP based on the two distinct fluorescence lifetimes of the protein. The spectra were highly overlapping which emphasizes the benefit of using the fluorescence lifetime to distinguish between the states. Moreover, we investigated the origin of the observed states: The origin of the dark state is known from literature and is attributed to the protonation-deprotonation dynamics of the chromophore. We related the observed two bright states to two conformers of the amino-acid E222 inside the β -barrel. These conformers were reported by X-ray studies of EGFP and differ mainly by a rotation of the E222 residue which changes the interaction with the chromophore.

Our experiment is the first to quantify fast photophysical transitions within a complex emitter using FLCS. We found a microsecond fast switching between the two fluorescent states of EGFP which we attribute to the rotational isomerization of an amino-acid close to the chromophore. Our experiment demonstrated the power of FLCS to study fast transition dynamics of a complex photophysical system and we hope that the method will be applied to a broad range of emitters and allow new insights into complex photophysical dynamics.

A.3 NANOBODY DETECTION OF STANDARD FLUORESCENT PROTEINS ENABLES MULTI-TARGET DNA-PAINT WITH HIGH RESOLUTION AND MINIMAL DISPLACEMENT ERRORS

In this work, we demonstrate superresolution imaging of cellular organelles with nanobodies that minimizes the displacement error to the structure of interest. Superresolution fluorescence microscopy allows cell biologists to study cellular structures and proteins of interest at the nanoscale. DNA-PAINT is a superresolution techniques that is neither affected by fluorophore bleaching nor limited by the number of spectrally distinguishable fluorophores for multi-target imaging. It is based on the transient binding and unbinding of short fluorescently labeled oligonucleotides to complementary docking strands, labeling the structure of interest. Because the binding of the oligonucleotide to the docking strand is sequence-specific, sequential imaging of different targets can be realized (Exchange-PAINT). A resolution below 10 nm for more than ten targets has been demonstrated on DNA origami structures. However, if the protein of interest is labeled by conventional antibody immunostaining, the pure size of a primary-secondary antibody complex introduces a displacement of up to 25 nm between the target and the fluorophore. This is also known as the linkage error and seriously limits the imaging resolution of superresolution microscopy. Several small probes have been developed to overcome this problem, among them aptamers and single-domain antibodies (nanobodies). But of these, only few probes for different targets are available, limiting the applicability of these probes.

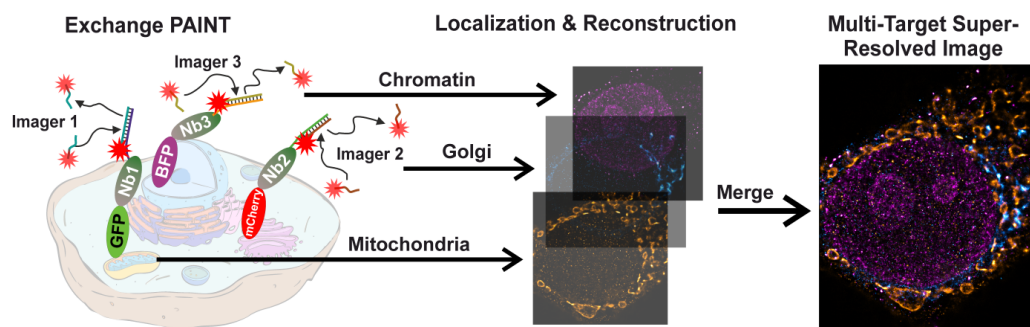


Figure A.3: Multi-Target Exchange-PAINT with Nanobodies. Fluorescent proteins were fused to the protein of interest and expressed in cells. Nanobodies modified with a short oligonucleotide for DNA-PAINT bound specifically to one of the fluorescent proteins (mTagBFP, EGFP, and mCherry). DNA-PAINT imaging was performed with an imager specific to the docking strand on the nanobody. By sequentially introducing the different imager strands, a multi-target superresolution image was obtained. This figure was created by *Roman Tsukanov*.

Here, we used small camelid nanobodies with a size of 2 to 3 nm which effectively minimize the fluorophore-target distance. The nanobodies against three different standard fluorescent proteins were modified with a docking strand for DNA-PAINT imaging. Cells were transfected with plasmids expressing the fluorescent proteins fused to a protein of interest to label the chromatin, the mitochondria, and the golgi-apparatus, respectively. We performed Exchange-PAINT experiments for three targets on a custom-built widefield setup with a programmable microfluidic setup. We achieved a resolution of 20 nm within 35 minutes of acquisition per target. Superresolution images of the mitochondria, the golgi-apparatus, and the chromatin distribution were obtained, see Fig. A.3. The structures in the superresolved images were in agreement with the direct observation of the fluorescent proteins.

In summary, we demonstrated multi-target superresolution imaging of cellular organelles with Exchange-PAINT and nanobodies. Since we used readily available nanobodies against standard fluorescent proteins, our method enables researchers who use conventional fluorescent proteins to obtain superresolved images of at least three common proteins with minimal fluorophore-target displacement error.

BIBLIOGRAPHY

- [6] Ulrich Kubitscheck. *Fluorescence Microscopy: From Principles to Biological Applications*. John Wiley & Sons, June 19, 2017. 504 pp.
- [7] Partha Pratim Mondal and Alberto Diaspro. *Fundamentals of Fluorescence Microscopy: Exploring Life with Light*. Springer Science & Business Media, Dec. 12, 2013. 219 pp.
- [8] M. Orrit and J. Bernard. "Single pentacene molecules detected by fluorescence excitation in a p-terphenyl crystal." In: *Physical Review Letters* 65.21 (Nov. 19, 1990), pp. 2716–2719. DOI: [10.1103/PhysRevLett.65.2716](https://doi.org/10.1103/PhysRevLett.65.2716).
- [9] W. E. Moerner. "A Dozen Years of Single-Molecule Spectroscopy in Physics, Chemistry, and Biophysics." In: *The Journal of Physical Chemistry B* 106.5 (Feb. 1, 2002), pp. 910–927. DOI: [10.1021/jp012992g](https://doi.org/10.1021/jp012992g).
- [10] Stefan W. Hell and Jan Wichmann. "Breaking the diffraction resolution limit by stimulated emission: stimulated-emission-depletion fluorescence microscopy." In: *Optics Letters* 19.11 (June 1, 1994), pp. 780–782. DOI: [10.1364/OL.19.000780](https://doi.org/10.1364/OL.19.000780).
- [11] Eric Betzig, George H. Patterson, Rachid Sougrat, O. Wolf Lindwasser, Scott Olenych, Juan S. Bonifacino, Michael W. Davidson, Jennifer Lippincott-Schwartz, and Harald F. Hess. "Imaging Intracellular Fluorescent Proteins at Nanometer Resolution." In: *Science* 313.5793 (Sept. 15, 2006), pp. 1642–1645. DOI: [10.1126/science.1127344](https://doi.org/10.1126/science.1127344).
- [12] Samuel T. Hess, Thanu P. K. Girirajan, and Michael D. Mason. "Ultra-High Resolution Imaging by Fluorescence Photoactivation Localization Microscopy." In: *Biophysical Journal* 91.11 (Dec. 1, 2006), pp. 4258–4272. DOI: [10.1529/biophysj.106.091116](https://doi.org/10.1529/biophysj.106.091116).
- [13] Michael J. Rust, Mark Bates, and Xiaowei Zhuang. "Sub-diffraction-limit imaging by stochastic optical reconstruction microscopy (STORM)." In: *Nature Methods* 3.10 (Oct. 2006), pp. 793–796. DOI: [10.1038/nmeth929](https://doi.org/10.1038/nmeth929).
- [14] Andreas Gahlmann and W. E. Moerner. "Exploring bacterial cell biology with single-molecule tracking and super-resolution imaging." In: *Nature Reviews Microbiology* 12.1 (Jan. 2014), pp. 9–22. DOI: [10.1038/nrmicro3154](https://doi.org/10.1038/nrmicro3154).
- [15] Lothar Schermelleh, Peter M. Carlton, Sebastian Haase, Lin Shao, Lukman Winoto, Peter Kner, Brian Burke, M. Cristina Cardoso, David A. Agard, Mats G. L. Gustafsson, Heinrich Leonhardt, and John W. Sedat. "Sub-diffraction Multicolor Imaging of the Nuclear Periphery with 3D Structured Illumination Microscopy." In: *Science* 320.5881 (June 6, 2008), pp. 1332–1336. DOI: [10.1126/science.1156947](https://doi.org/10.1126/science.1156947).

- [16] Anna Löschberger, Sebastian van de Linde, Marie-Christine Dabauvalle, Bernd Rieger, Mike Heilemann, Georg Krohne, and Markus Sauer. "Super-resolution imaging visualizes the eightfold symmetry of gp210 proteins around the nuclear pore complex and resolves the central channel with nanometer resolution." In: *J Cell Sci* 125.3 (Feb. 1, 2012), pp. 570–575. DOI: [10.1242/jcs.098822](https://doi.org/10.1242/jcs.098822).
- [17] Sebastian van de Linde, Mike Heilemann, and Markus Sauer. "Live-Cell Super-Resolution Imaging with Synthetic Fluorophores." In: *Annual Review of Physical Chemistry* 63.1 (2012). PMID: 22404589, pp. 519–540. DOI: [10.1146/annurev-physchem-032811-112012](https://doi.org/10.1146/annurev-physchem-032811-112012).
- [18] T. Ha, T. Enderle, D. F. Ogletree, D. S. Chemla, P. R. Selvin, and S. Weiss. "Probing the interaction between two single molecules: fluorescence resonance energy transfer between a single donor and a single acceptor." In: *Proceedings of the National Academy of Sciences* 93.13 (June 25, 1996), pp. 6264–6268. DOI: [10.1073/pnas.93.13.6264](https://doi.org/10.1073/pnas.93.13.6264).
- [19] Mykola Dimura, Thomas O Peulen, Christian A Hanke, Aiswaria Prakash, Holger Gohlke, and Claus AM Seidel. "Quantitative FRET studies and integrative modeling unravel the structure and dynamics of biomolecular systems." In: *Current Opinion in Structural Biology. Carbohydrate–protein interactions and glycosylation • Biophysical and molecular biological methods* 40 (Oct. 1, 2016), pp. 163–185. DOI: [10.1016/j.sbi.2016.11.012](https://doi.org/10.1016/j.sbi.2016.11.012).
- [20] Robert P Hertzberg and Andrew J Pope. "High-throughput screening: new technology for the 21st century." In: *Current Opinion in Chemical Biology* 4.4 (Aug. 1, 2000), pp. 445–451. DOI: [10.1016/S1367-5931\(00\)00110-1](https://doi.org/10.1016/S1367-5931(00)00110-1).
- [21] Rainer Pepperkok and Jan Ellenberg. "High-throughput fluorescence microscopy for systems biology." In: *Nature Reviews Molecular Cell Biology* 7.9 (Sept. 2006), pp. 690–696. DOI: [10.1038/nrm1979](https://doi.org/10.1038/nrm1979).
- [22] Manuel A. Robbins. *The Collector's Book of Fluorescent Minerals*. Springer US, 1983. XIII, 289.
- [23] C. E. Mills. *Bioluminescence of Aequorea*. Bioluminescence of Aequorea, a hydromedusa. Jan. 11, 2009. URL: <http://faculty.washington.edu/cemills/Aequorea.html> (visited on 09/18/2018).
- [24] J.R. Lakowicz. *Principles of Fluorescence Spectroscopy*. Springer US, 2013.
- [25] Lothar Schermelleh, Rainer Heintzmann, and Heinrich Leonhardt. "A guide to super-resolution fluorescence microscopy." In: *The Journal of Cell Biology* 190.2 (July 26, 2010), pp. 165–175. DOI: [10.1083/jcb.201002018](https://doi.org/10.1083/jcb.201002018).
- [26] Stefan W. Hell. "Far-Field Optical Nanoscopy." In: *Science* 316.5828 (May 25, 2007), pp. 1153–1158. DOI: [10.1126/science.1137395](https://doi.org/10.1126/science.1137395).
- [27] Bo Huang, Mark Bates, and Xiaowei Zhuang. "Super-Resolution Fluorescence Microscopy." In: *Annual Review of Biochemistry* 78.1 (June 1, 2009), pp. 993–1016. DOI: [10.1146/annurev.biochem.77.061906.092014](https://doi.org/10.1146/annurev.biochem.77.061906.092014).

- [28] Aongus McCarthy, Robert J. Collins, Nils J. Krichel, Verónica Fernández, Andrew M. Wallace, and Gerald S. Buller. “Long-range time-of-flight scanning sensor based on high-speed time-correlated single-photon counting.” In: *Applied Optics* 48.32 (Nov. 10, 2009), p. 6241. DOI: [10.1364/AO.48.006241](https://doi.org/10.1364/AO.48.006241).
- [29] John J. Degnan. “Photon-counting multikilohertz microlaser altimeters for airborne and spaceborne topographic measurements.” In: *Journal of Geodynamics* 34.3 (Oct. 1, 2002), pp. 503–549. DOI: [10.1016/S0264-3707\(02\)00045-5](https://doi.org/10.1016/S0264-3707(02)00045-5).
- [30] Brent Schwarz. “LIDAR: Mapping the world in 3D.” In: *Nature Photonics* 4 (July 1, 2010), pp. 429–430. DOI: [10.1038/nphoton.2010.148](https://doi.org/10.1038/nphoton.2010.148).
- [31] Wolfgang Becker. *Advanced Time-Correlated Single Photon Counting Techniques*. Ed. by A. W. Castleman, J.P. Toennies, and W. Zinth. Vol. 81. Springer Series in Chemical Physics. Berlin, Heidelberg: Springer Berlin Heidelberg, 2005.
- [32] M. D. Eisaman, J. Fan, A. Migdall, and S. V. Polyakov. “Invited Review Article: Single-photon sources and detectors.” In: *Review of Scientific Instruments* 82.7 (July 1, 2011), p. 071101. DOI: [10.1063/1.3610677](https://doi.org/10.1063/1.3610677).
- [33] Wolfgang Becker. *The bh TCSPC handbook*. Becker & Hickl, 2014.
- [34] Michael Wahl. *Time-Correlated Single Photon Counting*. 2014. URL: https://www.picoquant.com/images/uploads/page/files/7253/technote_tcspc.pdf (visited on 11/05/2018).
- [35] Desmond O’Connor. *Time-correlated single photon counting*. Academic Press, 1984. 299 pp.
- [36] Michael Wahl, Hans-Jürgen Rahn, Ingo Gregor, Rainer Erdmann, and Jörg Enderlein. “Dead-time optimized time-correlated photon counting instrument with synchronized, independent timing channels.” In: *Review of Scientific Instruments* 78.3 (Mar. 1, 2007), p. 033106. DOI: [10.1063/1.2715948](https://doi.org/10.1063/1.2715948).
- [37] Michael Wahl, Hans-Jürgen Rahn, Tino Röhlicke, Gerald Kell, Daniel Nettels, Frank Hillger, Ben Schuler, and Rainer Erdmann. “Scalable time-correlated photon counting system with multiple independent input channels.” In: *Review of Scientific Instruments* 79.12 (Dec. 1, 2008), p. 123113. DOI: [10.1063/1.3055912](https://doi.org/10.1063/1.3055912).
- [38] Michael Wahl, Ingo Gregor, Mattias Patting, and Jörg Enderlein. “Fast calculation of fluorescence correlation data with asynchronous time-correlated single-photon counting.” In: *Optics Express* 11.26 (Dec. 29, 2003), p. 3583. DOI: [10.1364/OE.11.003583](https://doi.org/10.1364/OE.11.003583).
- [39] Martin Böhmer, Michael Wahl, Hans-Jürgen Rahn, Rainer Erdmann, and Jörg Enderlein. “Time-resolved fluorescence correlation spectroscopy.” In: *Chemical Physics Letters* 353.5 (Feb. 26, 2002), pp. 439–445. DOI: [10.1016/S0009-2614\(02\)00044-1](https://doi.org/10.1016/S0009-2614(02)00044-1).
- [40] Peter Kapusta, Michael Wahl, Aleš Benda, Martin Hof, and Jörg Enderlein. “Fluorescence Lifetime Correlation Spectroscopy.” In: *Journal of Fluorescence* 17.1 (Dec. 27, 2006), pp. 43–48. DOI: [10.1007/s10895-006-0145-1](https://doi.org/10.1007/s10895-006-0145-1).

- [41] Ted A. Laurence, Achillefs N. Kapanidis, Xiangxu Kong, Daniel S. Chemla, and Shimon Weiss. "Photon Arrival-Time Interval Distribution (PAID): A Novel Tool for Analyzing Molecular Interactions." In: *The Journal of Physical Chemistry B* 108.9 (Mar. 1, 2004), pp. 3051–3067. DOI: [10.1021/jp036499b](https://doi.org/10.1021/jp036499b).
- [42] Xavier Michalet, Shimon Weiss, and Marcus Jäger. "Single-Molecule Fluorescence Studies of Protein Folding and Conformational Dynamics." In: *Chemical Reviews* 106.5 (May 1, 2006), pp. 1785–1813. DOI: [10.1021/cr0404343](https://doi.org/10.1021/cr0404343).
- [43] Valéry Zwiller, Hans Blom, Per Jonsson, Nikolay Panev, Sören Jeppesen, Tedros Tsegaye, Edgard Goobar, Mats-Erik Pistol, Lars Samuelson, and Gunnar Björk. "Single quantum dots emit single photons at a time: Antibunching experiments." In: *Applied Physics Letters* 78.17 (Apr. 13, 2001), pp. 2476–2478. DOI: [10.1063/1.1366367](https://doi.org/10.1063/1.1366367).
- [44] K. H. Drexhage, H. Kuhn, and F. P. Schäfer. "Variation of the Fluorescence Decay Time of a Molecule in Front of a Mirror." In: *Berichte der Bunsengesellschaft für physikalische Chemie* 72.2 (Mar. 1, 1968), pp. 329–329. DOI: [10.1002/bbpc.19680720261](https://doi.org/10.1002/bbpc.19680720261).
- [45] Hans Kuhn. "Classical Aspects of Energy Transfer in Molecular Systems." In: *The Journal of Chemical Physics* 53.1 (July 1970), pp. 101–108. DOI: [10.1063/1.1673749](https://doi.org/10.1063/1.1673749).
- [46] R. R. Chance, A. Prock, and R. Silbey. "Molecular fluorescence and energy transfer near interfaces." In: *Adv. Chem. Phys* 37.1 (1978), p. 65.
- [47] R. M. Amos and W. L. Barnes. "Modification of the spontaneous emission rate of Eu^{3+} ions close to a thin metal mirror." In: *Physical Review B* 55.11 (Mar. 15, 1997), pp. 7249–7254. DOI: [10.1103/PhysRevB.55.7249](https://doi.org/10.1103/PhysRevB.55.7249).
- [48] F. D. Stefani, K. Vasilev, N. Bocchio, N. Stoyanova, and M. Kreiter. "Surface-Plasmon-Mediated Single-Molecule Fluorescence Through a Thin Metallic Film." In: *Physical Review Letters* 94.2 (Jan. 19, 2005), p. 023005. DOI: [10.1103/PhysRevLett.94.023005](https://doi.org/10.1103/PhysRevLett.94.023005).
- [49] Michael Berndt, Mike Lorenz, Jörg Enderlein, and Stefan Diez. "Axial Nanometer Distances Measured by Fluorescence Lifetime Imaging Microscopy." In: *Nano Letters* 10.4 (Apr. 14, 2010), pp. 1497–1500. DOI: [10.1021/nl100593x](https://doi.org/10.1021/nl100593x).
- [50] Narain Karedla, Alexey I. Chizhik, Ingo Gregor, Anna M. Chizhik, Olaf Schulz, and Jörg Enderlein. "Single-Molecule Metal-Induced Energy Transfer (smMIET): Resolving Nanometer Distances at the Single-Molecule Level." In: *ChemPhysChem* 15.4 (Jan. 29, 2014), pp. 705–711. DOI: [10.1002/cphc.201300760](https://doi.org/10.1002/cphc.201300760).
- [51] Narain Karedla. "Single-Molecule Metal-Induced Energy Transfer: From Basics to Applications." PhD thesis. Göttingen: Universität Göttingen, Dec. 16, 2016.
- [52] John David Jackson. *Classical electrodynamics*. John Wiley & Sons, 2012.

- [53] Jörg Enderlein. "A Theoretical Investigation of Single-Molecule Fluorescence Detection on Thin Metallic Layers." In: *Biophysical Journal* 78.4 (Apr. 2000), pp. 2151–2158. DOI: [10.1016/S0006-3495\(00\)76761-0](https://doi.org/10.1016/S0006-3495(00)76761-0).
- [54] Jörg Enderlein. "Single-molecule fluorescence near a metal layer." In: *Chemical Physics* 247.1 (1999), pp. 1–9.
- [55] Daja Ruhlandt. "Modeling electrodynamics in the vicinity of metal nanostructures." PhD thesis. Göttingen: Universität Göttingen, 2018.
- [56] Olaf Schulz, Christoph Pieper, Michaela Clever, Janine Pfaff, Aike Ruhlandt, Ralph H. Kehlenbach, Fred S. Wouters, Jörg Grosshans, Gertrude Bunt, and Jörg Enderlein. "Resolution doubling in fluorescence microscopy with confocal spinning-disk image scanning microscopy." In: *Proceedings of the National Academy of Sciences* 110.52 (Dec. 24, 2013), pp. 21000–21005. DOI: [10.1073/pnas.1315858110](https://doi.org/10.1073/pnas.1315858110).
- [57] Arthur Edelstein, Nenad Amodaj, Karl Hoover, Ron Vale, and Nico Stuurman. "Computer Control of Microscopes Using μ Manager." In: *Current Protocols in Molecular Biology* 92.1 (Oct. 1, 2010), pp. 14.20.1–14.20.17. DOI: [10.1002/0471142727.mb1420s92](https://doi.org/10.1002/0471142727.mb1420s92).
- [58] Arthur D. Edelstein, Mark A. Tsuchida, Nenad Amodaj, Henry Pinkard, Ronald D. Vale, and Nico Stuurman. "Advanced methods of microscope control using μ Manager software." In: *Journal of Biological Methods* 1.2 (Nov. 7, 2014), e10. DOI: [10.14440/jbm.2014.36](https://doi.org/10.14440/jbm.2014.36).
- [59] Takeo Tanaami, Shinya Otsuki, Nobuhiro Tomosada, Yasuhito Kosugi, Mizuho Shimizu, and Hideyuki Ishida. "High-speed 1-frame/ms scanning confocal microscope with a microlens and Nipkow disks." In: *Applied Optics* 41.22 (Aug. 1, 2002), pp. 4704–4708. DOI: [10.1364/AO.41.004704](https://doi.org/10.1364/AO.41.004704).
- [60] James Pawley. *Handbook of Biological Confocal Microscopy*. 3rd ed. 2006. New York, NY: Springer, Aug. 10, 2006. 985 pp.
- [61] Shinya Inoue and Ted Inoue. "Direct-view high-speed confocal scanner: the CSU-10." In: *Collected Works Of Shinya Inoue: Microscopes, Living Cells, and Dynamic Molecules*. World Scientific, 2008, pp. 903–946.
- [62] Colin JR Sheppard. "Super-resolution in confocal imaging." In: *Optik* 80.2 (1988), pp. 53–54.
- [63] M. Bertero, P. Brianzi, and E. R. Pike. "Super-resolution in confocal scanning microscopy." In: *Inverse Problems* 3.2 (1987), p. 195.
- [64] Claus B. Müller and Jörg Enderlein. "Image Scanning Microscopy." In: *Physical Review Letters* 104.19 (May 10, 2010). DOI: [10.1103/PhysRevLett.104.198101](https://doi.org/10.1103/PhysRevLett.104.198101).
- [65] Andrew G. York, Sapun H. Parekh, Damian Dalle Nogare, Robert S. Fischer, Kelsey Temprine, Marina Mione, Ajay B. Chitnis, Christian A. Combs, and Hari Shroff. "Resolution doubling in live, multicellular organisms via multifocal structured illumination microscopy." In: *Nature Methods* 9.7 (July 2012), pp. 749–754. DOI: [10.1038/nmeth.2025](https://doi.org/10.1038/nmeth.2025).

- [66] M. G. L. Gustafsson. "Surpassing the lateral resolution limit by a factor of two using structured illumination microscopy." In: *Journal of Microscopy* 198.2 (May 1, 2000), pp. 82–87. DOI: [10.1046/j.1365-2818.2000.00710.x](https://doi.org/10.1046/j.1365-2818.2000.00710.x).
- [67] Andrew G. York, Panagiotis Chandris, Damian Dalle Nogare, Jeffrey Head, Peter Wawrzusin, Robert S. Fischer, Ajay Chitnis, and Hari Shroff. "Instant super-resolution imaging in live cells and embryos via analog image processing." In: *Nature Methods* 10.11 (Nov. 2013), pp. 1122–1126. DOI: [10.1038/nmeth.2687](https://doi.org/10.1038/nmeth.2687).
- [68] Stephan Roth, Colin JR Sheppard, Kai Wicker, and Rainer Heintzmann. "Optical photon reassignment microscopy (OPRA)." In: *Optical Nanoscopy* 2.1 (Oct. 18, 2013), p. 5. DOI: [10.1186/2192-2853-2-5](https://doi.org/10.1186/2192-2853-2-5).
- [69] Giulia M. R. De Luca, Ronald M. P. Breedijk, Rick A. J. Brandt, Christiaan H. C. Zeelenberg, Babette E. de Jong, Wendy Timmermans, Leila Nahidi Azar, Ron A. Hoebe, Sjoerd Stallinga, and Erik M. M. Manders. "Re-scan confocal microscopy: scanning twice for better resolution." In: *Biomedical Optics Express* 4.11 (Nov. 1, 2013), pp. 2644–2656. DOI: [10.1364/BOE.4.002644](https://doi.org/10.1364/BOE.4.002644).
- [70] Ingo Gregor, Martin Spiecker, Roman Petrovsky, Jörg Großhans, Robert Ros, and Jörg Enderlein. "Rapid nonlinear image scanning microscopy." In: *Nature Methods* 14.11 (Nov. 2017), pp. 1087–1089. DOI: [10.1038/nmeth.4467](https://doi.org/10.1038/nmeth.4467).
- [71] Takuya Azuma and Takayuki Kei. "Super-resolution spinning-disk confocal microscopy using optical photon reassignment." In: *Optics Express* 23.11 (June 1, 2015), pp. 15003–15011. DOI: [10.1364/OE.23.015003](https://doi.org/10.1364/OE.23.015003).
- [72] Shinichi Hayashi. "Resolution doubling using confocal microscopy via analogy with structured illumination microscopy." In: *Japanese Journal of Applied Physics* 55.8 (June 30, 2016), p. 082501. DOI: [10.7567/JJAP.55.082501](https://doi.org/10.7567/JJAP.55.082501).
- [73] E. N. Ward and R. Pal. "Image scanning microscopy: an overview." In: *Journal of Microscopy* 266.2 (May 1, 2017), pp. 221–228. DOI: [10.1111/jmi.12534](https://doi.org/10.1111/jmi.12534).
- [74] Colin J. R. Sheppard, Shalin B. Mehta, and Rainer Heintzmann. "Super-resolution by image scanning microscopy using pixel reassignment." In: *Optics Letters* 38.15 (Aug. 1, 2013), p. 2889. DOI: [10.1364/OL.38.002889](https://doi.org/10.1364/OL.38.002889).
- [75] E. Abbe. "Beiträge zur Theorie des Mikroskops und der mikroskopischen Wahrnehmung." In: *Archiv für mikroskopische Anatomie* 9.1 (Dec. 1, 1873), pp. 456–468. DOI: [10.1007/BF02956176](https://doi.org/10.1007/BF02956176).
- [76] George Patterson, Michael Davidson, Suliana Manley, and Jennifer Lippincott-Schwartz. "Superresolution Imaging using Single-Molecule Localization." In: *Annual Review of Physical Chemistry* 61.1 (2010), pp. 345–367. DOI: [10.1146/annurev.physchem.012809.103444](https://doi.org/10.1146/annurev.physchem.012809.103444).

- [77] J. Vangindertael, R. Camacho, W. Sempels, H. Mizuno, P. Dedecker, and K. P. F. Janssen. "An introduction to optical super-resolution microscopy for the adventurous biologist." In: *Methods and Applications in Fluorescence* 6.2 (2018), p. 022003. DOI: [10.1088/2050-6120/aaae0c](https://doi.org/10.1088/2050-6120/aaae0c).
- [78] Mike Heilemann, Sebastian van de Linde, Mark Schüttpelz, Robert Kasper, Britta Seefeldt, Anindita Mukherjee, Philip Tinnefeld, and Markus Sauer. "Subdiffraction-Resolution Fluorescence Imaging with Conventional Fluorescent Probes." In: *Angewandte Chemie International Edition* 47:33 (Aug. 4, 2008), pp. 6172–6176. DOI: [10.1002/anie.200802376](https://doi.org/10.1002/anie.200802376).
- [79] Ralf Jungmann, Christian Steinhauer, Max Scheible, Anton Kuzyk, Philip Tinnefeld, and Friedrich C. Simmel. "Single-Molecule Kinetics and Super-Resolution Microscopy by Fluorescence Imaging of Transient Binding on DNA Origami." In: *Nano Letters* 10.11 (Nov. 10, 2010), pp. 4756–4761. DOI: [10.1021/nl103427w](https://doi.org/10.1021/nl103427w).
- [80] Manuel F. Juetten, Travis J. Gould, Mark D. Lessard, Michael J. Mlodzianoski, Bhupendra S. Nagpure, Brian T. Bennett, Samuel T. Hess, and Joerg Bewersdorf. "Three-dimensional sub-100 nm resolution fluorescence microscopy of thick samples." In: *Nature Methods* 5.6 (June 2008), pp. 527–529. DOI: [10.1038/nmeth.1211](https://doi.org/10.1038/nmeth.1211).
- [81] Gleb Shtengel, James A. Galbraith, Catherine G. Galbraith, Jennifer Lippincott-Schwartz, Jennifer M. Gillette, Suliana Manley, Rachid Sougrat, Clare M. Waterman, Pakorn Kanchanawong, Michael W. Davidson, Richard D. Fetter, and Harald F. Hess. "Interferometric fluorescent super-resolution microscopy resolves 3D cellular ultrastructure." In: *Proceedings of the National Academy of Sciences* 106.9 (Mar. 3, 2009), pp. 3125–3130. DOI: [10.1073/pnas.0813131106](https://doi.org/10.1073/pnas.0813131106).
- [82] Reto Fiolka, Lin Shao, E. Hesper Rego, Michael W. Davidson, and Mats G. L. Gustafsson. "Time-lapse two-color 3D imaging of live cells with doubled resolution using structured illumination." In: *Proceedings of the National Academy of Sciences* 109.14 (Apr. 3, 2012), pp. 5311–5315. DOI: [10.1073/pnas.1119262109](https://doi.org/10.1073/pnas.1119262109).
- [83] Benjamin Harke, Chaitanya K. Ullal, Jan Keller, and Stefan W. Hell. "Three-Dimensional Nanoscopy of Colloidal Crystals." In: *Nano Letters* 8.5 (May 1, 2008), pp. 1309–1313. DOI: [10.1021/nl073164n](https://doi.org/10.1021/nl073164n).
- [84] Bo Huang, Wenqin Wang, Mark Bates, and Xiaowei Zhuang. "Three-Dimensional Super-Resolution Imaging by Stochastic Optical Reconstruction Microscopy." In: *Science* 319.5864 (Feb. 8, 2008), pp. 810–813. DOI: [10.1126/science.1153529](https://doi.org/10.1126/science.1153529).
- [85] N. Bourg, C. Mayet, G. Dupuis, T. Barroca, P. Bon, S. Lécart, E. Fort, and S. Lévêque-Fort. "Direct optical nanoscopy with axially localized detection." In: *Nature Photonics* 9.9 (Sept. 2015), pp. 587–593. DOI: [10.1038/nphoton.2015.132](https://doi.org/10.1038/nphoton.2015.132).

- [86] B. P. Olveczky, N. Periasamy, and A. S. Verkman. "Mapping fluorophore distributions in three dimensions by quantitative multiple angle-total internal reflection fluorescence microscopy." In: *Biophysical Journal* 73.5 (Nov. 1, 1997), pp. 2836–2847. DOI: [10.1016/S0006-3495\(97\)78312-7](https://doi.org/10.1016/S0006-3495(97)78312-7).
- [87] Wenjie Liu, Kimani C. Toussaint, Chukwuemeka Okoro, Dazhao Zhu, Youhua Chen, Cuifang Kuang, and Xu Liu. "Breaking the Axial Diffraction Limit: A Guide to Axial Super-Resolution Fluorescence Microscopy." In: *Laser & Photonics Reviews* 12.8 (Aug. 1, 2018), p. 1700333. DOI: [10.1002/lpor.201700333](https://doi.org/10.1002/lpor.201700333).
- [88] Andrea L. Stout and Daniel Axelrod. "Evanescent field excitation of fluorescence by epi-illumination microscopy." In: *Applied Optics* 28.24 (Dec. 15, 1989), pp. 5237–5242. DOI: [10.1364/AO.28.005237](https://doi.org/10.1364/AO.28.005237).
- [89] J. S. Burmeister, G. A. Truskey, and W. M. Reichert. "Quantitative analysis of variable-angle total internal reflection fluorescence microscopy (VA-TIRFM) of cell/substrate contacts." In: *Journal of Microscopy* 173.1 (Jan. 1, 1994), pp. 39–51. DOI: [10.1111/j.1365-2818.1994.tb03426.x](https://doi.org/10.1111/j.1365-2818.1994.tb03426.x).
- [90] K. Stock, R. Sailer, W. S. L. Strauss, M. Lyttek, R. Steiner, and H. Schneckenburger. "Variable-angle total internal reflection fluorescence microscopy (VA-TIRFM): realization and application of a compact illumination device." In: *Journal of Microscopy* 211.1 (July 1, 2003), pp. 19–29. DOI: [10.1046/j.1365-2818.2003.01200.x](https://doi.org/10.1046/j.1365-2818.2003.01200.x).
- [91] Daniel R. Stabley, Thomas Oh, Sanford M. Simon, Alexa L. Mattheyses, and Khalid Salaita. "Real-time fluorescence imaging with 20 nm axial resolution." In: *Nature Communications* 6 (Sept. 22, 2015), p. 8307. DOI: [10.1038/ncomms9307](https://doi.org/10.1038/ncomms9307).
- [92] Thomas Ruckstuhl and Dorinel Verdes. "Supercritical angle fluorescence (SAF) microscopy." In: *Optics Express* 12.18 (Sept. 6, 2004), pp. 4246–4254. DOI: [10.1364/OPEX.12.004246](https://doi.org/10.1364/OPEX.12.004246).
- [93] Christian M. Winterflood, Thomas Ruckstuhl, Dorinel Verdes, and Stefan Seeger. "Nanometer Axial Resolution by Three-Dimensional Supercritical Angle Fluorescence Microscopy." In: *Physical Review Letters* 105.10 (Aug. 31, 2010), p. 108103. DOI: [10.1103/PhysRevLett.105.108103](https://doi.org/10.1103/PhysRevLett.105.108103).
- [94] Joran Deschamps, Markus Mund, and Jonas Ries. "3D superresolution microscopy by supercritical angle detection." In: *Optics Express* 22.23 (Nov. 17, 2014), pp. 29081–29091. DOI: [10.1364/OE.22.029081](https://doi.org/10.1364/OE.22.029081).
- [95] Th Förster. "Zwischenmolekulare Energiewanderung und Fluoreszenz." In: *Annalen der Physik* 437.1 (Jan. 1, 1948), pp. 55–75. DOI: [10.1002/andp.19484370105](https://doi.org/10.1002/andp.19484370105).
- [96] Daniel Nettels, Armin Hoffmann, and Benjamin Schuler. "Unfolded Protein and Peptide Dynamics Investigated with Single-Molecule FRET and Correlation Spectroscopy from Picoseconds to Seconds[†]." In: *The Journal of Physical Chemistry B* 112.19 (May 2008), pp. 6137–6146. DOI: [10.1021/jp076971j](https://doi.org/10.1021/jp076971j).

- [97] Rahul Roy, Sungchul Hohng, and Taekjip Ha. "A practical guide to single-molecule FRET." In: *Nature Methods* 5.6 (June 2008), pp. 507–516. DOI: [10.1038/nmeth.1208](https://doi.org/10.1038/nmeth.1208).
- [98] Benjamin Schuler, Andrea Soranno, Hagen Hofmann, and Daniel Nettels. "Single-Molecule FRET Spectroscopy and the Polymer Physics of Unfolded and Intrinsically Disordered Proteins." In: *Annual Review of Biophysics* 45.1 (July 5, 2016), pp. 207–231. DOI: [10.1146/annurev-biophys-062215-010915](https://doi.org/10.1146/annurev-biophys-062215-010915).
- [99] Achillefs N. Kapanidis, Nam Ki Lee, Ted A. Laurence, Sören Doose, Emmanuel Margeat, and Shimon Weiss. "Fluorescence-aided molecule sorting: Analysis of structure and interactions by alternating-laser excitation of single molecules." In: *Proceedings of the National Academy of Sciences* 101.24 (June 15, 2004), pp. 8936–8941. DOI: [10.1073/pnas.0401690101](https://doi.org/10.1073/pnas.0401690101).
- [100] Barbara K. Müller, Evgeny Zaychikov, Christoph Bräuchle, and Don C. Lamb. "Pulsed Interleaved Excitation." In: *Biophysical Journal* 89.5 (Nov. 1, 2005), pp. 3508–3522. DOI: [10.1529/biophysj.105.064766](https://doi.org/10.1529/biophysj.105.064766).
- [101] John T. Fourkas. "Rapid determination of the three-dimensional orientation of single molecules." In: *Optics letters* 26.4 (2001), pp. 211–213.
- [102] Martin Böhmer and Jörg Enderlein. "Orientation imaging of single molecules by wide-field epifluorescence microscopy." In: *JOSA B* 20.3 (Mar. 1, 2003), pp. 554–559. DOI: [10.1364/JOSAB.20.000554](https://doi.org/10.1364/JOSAB.20.000554).
- [103] Richard Börner, Danny Kowerko, Stefan Krause, Christian von Borczyskowski, and Christian G. Hübner. "Efficient simultaneous fluorescence orientation, spectrum, and lifetime detection for single molecule dynamics." In: *The Journal of Chemical Physics* 137.16 (Oct. 28, 2012), p. 164202. DOI: [10.1063/1.4759108](https://doi.org/10.1063/1.4759108).
- [104] Alexey I. Chizhik, Jan Rother, Ingo Gregor, Andreas Janshoff, and Jörg Enderlein. "Metal-induced energy transfer for live cell nanoscopy." In: *Nature Photonics* 8.2 (Feb. 2014), pp. 124–127. DOI: [10.1038/nphoton.2013.345](https://doi.org/10.1038/nphoton.2013.345).
- [105] Anna M. Chizhik, Carina Wollnik, Daja Ruhlandt, Narain Karedla, Alexey I. Chizhik, Lara Hauke, Dirk Hähnel, Ingo Gregor, Jörg Enderlein, Florian Rehfeldt, and Patricia Bassereau. "Dual-color metal-induced and Förster resonance energy transfer for cell nanoscopy." In: *Molecular Biology of the Cell* 29.7 (Apr. 1, 2018), pp. 846–851. DOI: [10.1091/mbc.E17-05-0314](https://doi.org/10.1091/mbc.E17-05-0314).
- [106] Matthew P. Gordon, Taekjip Ha, and Paul R. Selvin. "Single-molecule high-resolution imaging with photobleaching." In: *Proceedings of the National Academy of Sciences* 101.17 (Apr. 27, 2004), pp. 6462–6465. DOI: [10.1073/pnas.0401638101](https://doi.org/10.1073/pnas.0401638101).
- [107] Sarah R. Needham, Michael Hirsch, Daniel J. Rolfe, David T. Clarke, Laura C. Zanetti-Domingues, Richard Wareham, and Marisa L. Martin-Fernandez. "Measuring EGFR Separations on Cells with ~10 nm Resolution via Fluorophore Localization Imaging with Photobleaching." In: *PLOS ONE* 8.5 (May 1, 2013), e62331. DOI: [10.1371/journal.pone.0062331](https://doi.org/10.1371/journal.pone.0062331).

- [108] Mario Raab, Ija Jusuk, Julia Molle, Egbert Buhr, Bernd Bodermann, Detlef Bergmann, Harald Bosse, and Philip Tinnefeld. "Using DNA origami nanorulers as traceable distance measurement standards and nanoscopic benchmark structures." In: *Scientific Reports* 8.1 (Jan. 29, 2018), p. 1780. DOI: [10.1038/s41598-018-19905-x](https://doi.org/10.1038/s41598-018-19905-x).
- [109] Anastasiya Puchkova, Carolin Vietz, Enrico Pibiri, Bettina Wunsch, María Sanz Paz, Guillermo P. Acuna, and Philip Tinnefeld. "DNA Origami Nanoantennas with over 5000-fold Fluorescence Enhancement and Single-Molecule Detection at 25 μ M." In: *Nano Letters* 15.12 (Dec. 9, 2015), pp. 8354–8359. DOI: [10.1021/acs.nanolett.5b04045](https://doi.org/10.1021/acs.nanolett.5b04045).
- [110] Sebastian Isbaner, Narain Karedla, Izabela Kaminska, Daja Ruhlandt, Mario Raab, Johann Bohlen, Alexey Chizhik, Ingo Gregor, Philip Tinnefeld, Jörg Enderlein, and Roman Tsukanov. "Axial Colocalization of Single Molecules with Nanometer Accuracy Using Metal-Induced Energy Transfer." In: *Nano Letters* 18.4 (Apr. 11, 2018), pp. 2616–2622. DOI: [10.1021/acs.nanolett.8b00425](https://doi.org/10.1021/acs.nanolett.8b00425).
- [111] Bo Shuang, David Cooper, J. Nick Taylor, Lydia Kisley, Jixin Chen, Wenxiao Wang, Chun Biu Li, Tamiki Komatsuzaki, and Christy F. Landes. "Fast Step Transition and State Identification (STaSI) for Discrete Single-Molecule Data Analysis." In: *The Journal of Physical Chemistry Letters* 5.18 (Sept. 18, 2014), pp. 3157–3161. DOI: [10.1021/jz501435p](https://doi.org/10.1021/jz501435p).
- [112] A. Mooradian. "Photoluminescence of Metals." In: *Physical Review Letters* 22.5 (Feb. 3, 1969), pp. 185–187. DOI: [10.1103/PhysRevLett.22.185](https://doi.org/10.1103/PhysRevLett.22.185).
- [113] Clifford B. Talbot, Rakesh Patalay, Ian Munro, Sean Warren, Fulvio Ratto, Paolo Matteini, Roberto Pini, H. Georg Breunig, Karsten König, Antony C. Chu, Gordon W. Stamp, Mark A. A. Neil, Paul M. W. French, and Chris Dunsby. "Application of ultrafast gold luminescence to measuring the instrument response function for multispectral multiphoton fluorescence lifetime imaging." In: *Optics Express* 19.15 (July 18, 2011), pp. 13848–13861. DOI: [10.1364/OE.19.013848](https://doi.org/10.1364/OE.19.013848).
- [114] Aleksandar D. Rakić, Aleksandra B. Djurišić, Jovan M. Elazar, and Marian L. Majewski. "Optical properties of metallic films for vertical-cavity optoelectronic devices." In: *Applied Optics* 37.22 (Aug. 1, 1998), pp. 5271–5283. DOI: [10.1364/AO.37.005271](https://doi.org/10.1364/AO.37.005271).
- [115] L. Stirling Churchman, Henrik Flyvbjerg, and James A. Spudich. "A Non-Gaussian Distribution Quantifies Distances Measured with Fluorescence Localization Techniques." In: *Biophysical Journal* 90.2 (Jan. 2006), pp. 668–671. DOI: [10.1529/biophysj.105.065599](https://doi.org/10.1529/biophysj.105.065599).
- [116] Jürgen J. Schmied, Carsten Forthmann, Enrico Pibiri, Birka Lalkens, Philipp Nickels, Tim Liedl, and Philip Tinnefeld. "DNA Origami Nanopillars as Standards for Three-Dimensional Superresolution Microscopy." In: *Nano Letters* 13.2 (Feb. 13, 2013), pp. 781–785. DOI: [10.1021/nl304492y](https://doi.org/10.1021/nl304492y).
- [117] A. Bujacz. "Structures of bovine, equine and leporine serum albumin." In: *Acta Crystallographica Section D: Biological Crystallography* 68.10 (Oct. 1, 2012), pp. 1278–1289. DOI: [10.1107/S0907444912027047](https://doi.org/10.1107/S0907444912027047).

- [118] A Scarangella, M Soumbo, C Villeneuve-Faure, A Mlayah, C Bonafos, M-C Monje, C Roques, and K Makasheva. "Adsorption properties of BSA and DsRed proteins deposited on thin SiO₂ layers: optically non-absorbing versus absorbing proteins." In: *Nanotechnology* 29.11 (Mar. 16, 2018), p. 115101. DOI: [10.1088/1361-6528/aaa68b](https://doi.org/10.1088/1361-6528/aaa68b).
- [119] Karin Spaeth, Andreas Brecht, and Günter Gauglitz. "Studies on the Biotin–Avidin Multilayer Adsorption by Spectroscopic Ellipsometry." In: *Journal of Colloid and Interface Science* 196.2 (Dec. 1997), pp. 128–135. DOI: [10.1006/jcis.1997.5200](https://doi.org/10.1006/jcis.1997.5200).
- [120] Quan Wang and W. E. Moerner. "Lifetime and Spectrally Resolved Characterization of the Photodynamics of Single Fluorophores in Solution Using the Anti-Brownian Electrokinetic Trap." In: *The Journal of Physical Chemistry B* 117.16 (Apr. 25, 2013), pp. 4641–4648. DOI: [10.1021/jp308949d](https://doi.org/10.1021/jp308949d).
- [121] Martin Hoefling, Nicola Lima, Dominik Haenni, Claus A. M. Seidel, Benjamin Schuler, and Helmut Grubmüller. "Structural Heterogeneity and Quantitative FRET Efficiency Distributions of Polyprolines through a Hybrid Atomistic Simulation and Monte Carlo Approach." In: *PLOS ONE* 6.5 (May 24, 2011), e19791. DOI: [10.1371/journal.pone.0019791](https://doi.org/10.1371/journal.pone.0019791).
- [122] Joachim Frank. *Three-Dimensional Electron Microscopy of Macromolecular Assemblies: Visualization of Biological Molecules in Their Native State*. Oxford University Press, Feb. 2, 2006. 427 pp.
- [123] Sanghwa Lee, Jinwoo Lee, and Sungchul Hohng. "Single-Molecule Three-Color FRET with Both Negligible Spectral Overlap and Long Observation Time." In: *PLOS ONE* 5.8 (Aug. 19, 2010), e12270. DOI: [10.1371/journal.pone.0012270](https://doi.org/10.1371/journal.pone.0012270).
- [124] Ingo H. Stein, Christian Steinhauer, and Philip Tinnefeld. "Single-Molecule Four-Color FRET Visualizes Energy-Transfer Paths on DNA Origami." In: *Journal of the American Chemical Society* 133.12 (Mar. 30, 2011), pp. 4193–4195. DOI: [10.1021/ja1105464](https://doi.org/10.1021/ja1105464).
- [125] Narain Karedla, Anna M. Chizhik, Simon C. Stein, Daja Ruhlandt, Ingo Gregor, Alexey I. Chizhik, and Jörg Enderlein. "Three-dimensional single-molecule localization with nanometer accuracy using Metal-Induced Energy Transfer (MIET) imaging." In: *The Journal of Chemical Physics* 148.20 (May 24, 2018), p. 204201. DOI: [10.1063/1.5027074](https://doi.org/10.1063/1.5027074).
- [126] Mike Heilemann, Dirk P. Herten, Rainer Heintzmann, Christoph Cremer, Christian Müller, Philip Tinnefeld, Kenneth D. Weston, Jürgen Wolfrum, and Markus Sauer. "High-Resolution Colocalization of Single Dye Molecules by Fluorescence Lifetime Imaging Microscopy." In: *Analytical Chemistry* 74.14 (July 2002), pp. 3511–3517. DOI: [10.1021/ac025576g](https://doi.org/10.1021/ac025576g).
- [127] Francisco Balzarotti, Yvan Eilers, Klaus C. Gwosch, Arvid H. Gynnå, Volker Westphal, Fernando D. Stefani, Johan Elf, and Stefan W. Hell. "Nanometer resolution imaging and tracking of fluorescent molecules with minimal photon fluxes." In: *Science* (Dec. 22, 2016), aak9913. DOI: [10.1126/science.aak9913](https://doi.org/10.1126/science.aak9913).

- [128] Fang Huang, Samantha L. Schwartz, Jason M. Byars, and Keith A. Lidke. "Simultaneous multiple-emitter fitting for single molecule super-resolution imaging." In: *Biomedical Optics Express* 2.5 (May 1, 2011), pp. 1377–1393. DOI: [10.1364/B0E.2.001377](https://doi.org/10.1364/B0E.2.001377).
- [129] Joerg Schnitzbauer, Maximilian T Strauss, Thomas Schlichthaerle, Florian Schueder, and Ralf Jungmann. "Super-resolution microscopy with DNA-PAINT." In: *Nature Protocols* 12.6 (May 18, 2017), pp. 1198–1228. DOI: [10.1038/nprot.2017.024](https://doi.org/10.1038/nprot.2017.024).
- [130] Florian Schueder, Juanita Lara-Gutiérrez, Brian J. Beliveau, Sinem K. Saka, Hiroshi M. Sasaki, Johannes B. Woehrstein, Maximilian T. Strauss, Heinrich Grabmayr, Peng Yin, and Ralf Jungmann. "Multiplexed 3D super-resolution imaging of whole cells using spinning disk confocal microscopy and DNA-PAINT." In: *Nature Communications* 8.1 (Dec. 12, 2017), p. 2090. DOI: [10.1038/s41467-017-02028-8](https://doi.org/10.1038/s41467-017-02028-8).
- [131] Sören Doose, Hannes Neuweiler, and Markus Sauer. "Fluorescence Quenching by Photoinduced Electron Transfer: A Reporter for Conformational Dynamics of Macromolecules." In: *ChemPhysChem* 10.9 (July 13, 2009), pp. 1389–1398. DOI: [10.1002/cphc.200900238](https://doi.org/10.1002/cphc.200900238).
- [132] Thomas Ruckstuhl and Stefan Seeger. "Confocal total-internal-reflection fluorescence microscopy with a high-aperture parabolic mirror lens." In: *Applied Optics* 42.16 (June 1, 2003), pp. 3277–3283. DOI: [10.1364/AO.42.003277](https://doi.org/10.1364/AO.42.003277).
- [133] Kai Hassler, Marcel Leutenegger, Per Rigler, Ramachandra Rao, Rudolf Rigler, Michael Gösch, and Theo Lasser. "Total internal reflection fluorescence correlation spectroscopy (TIR-FCS) with low background and high count-rate per molecule." In: *Optics Express* 13.19 (Sept. 19, 2005), pp. 7415–7423. DOI: [10.1364/OPEX.13.007415](https://doi.org/10.1364/OPEX.13.007415).
- [134] Marcel Leutenegger, Christian Ringemann, Theo Lasser, Stefan W. Hell, and Christian Eggeling. "Fluorescence correlation spectroscopy with a total internal reflection fluorescence STED microscope (TIRF-STED-FCS)." In: *Optics Express* 20.5 (Feb. 27, 2012), pp. 5243–5263. DOI: [10.1364/OE.20.005243](https://doi.org/10.1364/OE.20.005243).
- [135] Sanjay Tyagi and Fred Russell Kramer. "Molecular Beacons: Probes that Fluoresce upon Hybridization." In: *Nature Biotechnology* 14.3 (Mar. 1996), pp. 303–308. DOI: [10.1038/nbt0396-303](https://doi.org/10.1038/nbt0396-303).
- [136] Thomas Niehörster, Anna Löscherger, Ingo Gregor, Benedikt Krämer, Hans-Jürgen Rahn, Matthias Patting, Felix Koberling, Jörg Enderlein, and Markus Sauer. "Multi-target spectrally resolved fluorescence lifetime imaging microscopy." In: *Nature Methods* 13.3 (Mar. 2016), pp. 257–262. DOI: [10.1038/nmeth.3740](https://doi.org/10.1038/nmeth.3740).
- [137] Robert M Clegg. "Fluorescence resonance energy transfer." In: *Current Opinion in Biotechnology* 6.1 (Jan. 1, 1995), pp. 103–110. DOI: [10.1016/0958-1669\(95\)80016-6](https://doi.org/10.1016/0958-1669(95)80016-6).

- [138] Robert M. Clegg. “Chapter 1 Förster resonance energy transfer—FRET what is it, why do it, and how it’s done.” In: *Fret and Flim Techniques*. Vol. 33. Laboratory Techniques in Biochemistry and Molecular Biology. Elsevier, 2009, pp. 1–57. DOI: [10.1016/S0075-7535\(08\)00001-6](https://doi.org/10.1016/S0075-7535(08)00001-6).
- [139] Lior Turgeman and Dror Fixler. “The influence of dead time related distortions on live cell fluorescence lifetime imaging (FLIM) experiments.” In: *Journal of Biophotonics* 7.6 (June 1, 2014), pp. 442–452. DOI: [10.1002/jbio.201300018](https://doi.org/10.1002/jbio.201300018).
- [140] C. C. Davis and T. A. King. “Correction methods for photon pile-up in lifetime determination by single-photon counting.” In: *Journal of Physics A: General Physics* 3.1 (1970), p. 101. DOI: [10.1088/0305-4470/3/1/013](https://doi.org/10.1088/0305-4470/3/1/013).
- [141] Christian Holzapfel. “On statistics of time-to-amplitude converter systems in photon counting devices.” In: *Review of Scientific Instruments* 45.7 (1974), pp. 894–896. DOI: [10.1063/1.1686762](https://doi.org/10.1063/1.1686762).
- [142] Matthias Patting, Michael Wahl, Peter Kapusta, and Rainer Erdmann. “Dead-time effects in TCSPC data analysis.” In: *Proc. SPIE 6583, Photon Counting Applications, Quantum Optics, and Quantum Cryptography*. Ed. by Ivan Prochazka, Alan L. Migdall, Alexandre Pauchard, Miloslav Dusek, Mark S. Hillery, and Wolfgang P. Schleich. May 4, 2007, pp. 658307–658307–10. DOI: [10.1117/12.722804](https://doi.org/10.1117/12.722804).
- [143] Jochen Arlt, David Tyndall, Bruce R. Rae, David D.-U. Li, Justin A. Richardson, and Robert K. Henderson. “A study of pile-up in integrated time-correlated single photon counting systems.” In: *Review of Scientific Instruments* 84.10 (Oct. 1, 2013), p. 103105. DOI: [10.1063/1.4824196](https://doi.org/10.1063/1.4824196).
- [144] Glenn F. Knoll. *Radiation Detection and Measurement*. John Wiley & Sons, Aug. 16, 2010. 857 pp.
- [145] L. Fleury, J.-M. Segura, G. Zumofen, B. Hecht, and U. P. Wild. “Nonclassical Photon Statistics in Single-Molecule Fluorescence at Room Temperature.” In: *Physical Review Letters* 84.6 (Feb. 7, 2000), pp. 1148–1151. DOI: [10.1103/PhysRevLett.84.1148](https://doi.org/10.1103/PhysRevLett.84.1148).
- [146] Sebastian Isbaner, Narain Karedla, Daja Ruhlandt, Simon Christoph Stein, Anna Chizhik, Ingo Gregor, and Jörg Enderlein. “Dead-time correction of fluorescence lifetime measurements and fluorescence lifetime imaging.” In: *Optics Express* 24.9 (May 2, 2016), pp. 9429–9445. DOI: [10.1364/OE.24.009429](https://doi.org/10.1364/OE.24.009429).
- [147] Robert J. Moerland and Jacob P. Hoogenboom. “Subnanometer-accuracy optical distance ruler based on fluorescence quenching by transparent conductors.” In: *Optica* 3.2 (Feb. 20, 2016), pp. 112–117. DOI: [10.1364/OPTICA.3.000112](https://doi.org/10.1364/OPTICA.3.000112).
- [148] Alessandro Esposito, Christoph P. Dohm, Matthias Bähr, and Fred S. Wouters. “Unsupervised Fluorescence Lifetime Imaging Microscopy for High Content and High Throughput Screening.” In: *Molecular & Cellular Proteomics* 6.8 (Aug. 1, 2007), pp. 1446–1454. DOI: [10.1074/mcp.T700006-MCP200](https://doi.org/10.1074/mcp.T700006-MCP200).

- [149] Thilo Baronsky, Daja Ruhlandt, Bastian Rouven Brückner, Jonas Schäfer, Narain Karedla, Sebastian Isbaner, Dirk Hähnel, Ingo Gregor, Jörg Enderlein, Andreas Janshoff, and Alexey I. Chizhik. "Cell–Substrate Dynamics of the Epithelial-to-Mesenchymal Transition." In: *Nano Letters* 17.5 (May 10, 2017), pp. 3320–3326. DOI: [10.1021/acs.nanolett.7b01558](https://doi.org/10.1021/acs.nanolett.7b01558).
- [150] Arindam Ghosh, Sebastian Isbaner, Manoel Veiga-Gutiérrez, Ingo Gregor, Jörg Enderlein, and Narain Karedla. "Quantifying Microsecond Transition Times Using Fluorescence Lifetime Correlation Spectroscopy." In: *The Journal of Physical Chemistry Letters* 8.24 (Dec. 21, 2017), pp. 6022–6028. DOI: [10.1021/acs.jpcllett.7b02707](https://doi.org/10.1021/acs.jpcllett.7b02707).

ACKNOWLEDGMENTS

This thesis would not have been possible without the help of many people.

I would like to thank my supervisor *Jörg Enderlein* for his guidance and his continuous support and motivation. I admire his insights and his inexhaustible pool of ideas. It was a valuable experience to have the freedom to try out many things in the lab or on the computer, and I learned a lot about single-molecule methods and imaging during this time. I could not have spent the last years better.

I thank Prof. *Helmut Grubmüller* and Prof. *Andreas Janshoff* for their input, their striking questions, and their time to discuss my work in the thesis committee meetings.

The whole Enderlein group has been very supportive. I want to thank in particular *Ingo Gregor* for sharing his expertise and for his invaluable help in the lab. My colleague *Narain Karedla* was an inspiring example for me. I thank him for sharing his motivation and lab experience, the stimulating discussions, and the good company. *Roman Tsukanov* and his expertise on DNA origami came at the right time. He has been an excellent project manager and an untiring motivator and I thank him for that. I thank *Anna & Alexey Chizhik* for sharing their experience on MIET and in the lab, for example the tutorial on the preparation of clean coverslips and how to find cells under a microscope. I thank *Daja Ruhlandt* for our many interesting discussions about MIET theory and lifetime fitting. I thank *Simon Stein* for sharing his Matlab expertise, and especially the memorable coding session for the implementation of the dead-time correction. I thank *Shun Qin* for his collaboration in the CSDISM project and his persistence to make it work. I thank my office mates *Narain, Jan, Sid, and Aditya* for the animating discussions and the good working atmosphere. I highly appreciate the professional and non-professional conversations and joint activities with my colleagues *Steffen, Arindam, Soheil, Christoph, and Akshita*.

At my workplace at the third institute of physics, I have received help from many colleagues. I thank *Dieter Hille* and his team from the mechanical workshop for realizing my ideas in aluminum and other materials, *Thomas Geiling* for his assistance with IT issues, and the secretaries *Elke Zech, Sabine Huhnold, Eva Ausmeier, and Nicole Rehbein* for their help with administration and making my life easier.

The Göttingen campus has been a stimulating environment, and I want to thank the SFB 937 for connecting us PhD students and for the funding of my work. I also thank *Antje Erdmann* from the IMPRS-PBCS office for always being approachable for questions and concerns, especially during my time as student representative.

For proof-reading this thesis and for many helpful comments I thank *Narain, Roman, Christoph, and especially Sarah*.

This document was typeset using L^AT_EX and the classicthesis template developed by André Miede and Ivo Pletikosić.

CURRICULUM VITAE

SEBASTIAN ISBANER

Place of birth: Bremerhaven

Nationality: German

ACADEMICAL BACKGROUND

| | |
|----------------|--|
| 2015 – present | Doctoral Dissertation Thesis: <i>Extending Resolution in All Directions: Image Scanning Microscopy and Metal-induced Energy Transfer</i> Georg-August-Universität Göttingen, Göttingen |
| 2011 – 2014 | Master of Science in Physics Thesis: <i>Single Molecule Spectroscopy with Alternating Laser Excitation</i> Ruprecht-Karls-Universität, Heidelberg |
| 2010 – 2011 | ERASMUS semester Uppsala University, Uppsala |
| 2008 – 2011 | Bachelor of Science in Physics Thesis: <i>On Mechanical Properties of Metaphase Chromosomes</i> Ruprecht-Karls-Universität, Heidelberg |
| 2005 – 2008 | Abitur Advanced courses in physics and biology HIGHSEA School Project at the Alfred-Wegener-Institut Bremerhaven Schulzentrum Geschwister Scholl, Bremerhaven |

SCHOLARSHIPS

| | |
|-------------|---|
| 2017 | DAAD Travel Grant |
| 2008 – 2014 | German National Academic Foundation (Studienstiftung des Deutschen Volkes) |

PUBLICATIONS

- 2019 Shama Sograte-Idrissi, Nazar Oleksiievets, *Sebastian Isbaner*, Mariana Eggert-Martinez, Jörg Enderlein, Roman Tsukanov, and Felipe Opazo. "Nanobody Detection of Standard Fluorescent Proteins Enables Multi-Target DNA-PAINT with High Resolution and Minimal Displacement Errors." In: *Cells* 8.1 (Jan. 10, 2019), p. 48. DOI: [10.3390/cells8010048](https://doi.org/10.3390/cells8010048)
- 2018 *Sebastian Isbaner*, Narain Karedla, Izabela Kaminska, Daja Ruhlandt, Mario Raab, Johann Bohlen, Alexey Chizhik, Ingo Gregor, Philip Tinnefeld, Jörg Enderlein, and Roman Tsukanov. "Axial Colocalization of Single Molecules with Nanometer Accuracy Using Metal-Induced Energy Transfer." In: *Nano Letters* 18.4 (Apr. 11, 2018), pp. 2616–2622. DOI: [10.1021/acs.nanolett.8b00425](https://doi.org/10.1021/acs.nanolett.8b00425)
- 2017 Arindam Ghosh, *Sebastian Isbaner*, Manoel Veiga-Gutiérrez, Ingo Gregor, Jörg Enderlein, and Narain Karedla. "Quantifying Microsecond Transition Times Using Fluorescence Lifetime Correlation Spectroscopy." In: *The Journal of Physical Chemistry Letters* 8.24 (Dec. 21, 2017), pp. 6022–6028. DOI: [10.1021/acs.jpcllett.7b02707](https://doi.org/10.1021/acs.jpcllett.7b02707)
- Thilo Baronsky, Daja Ruhlandt, Bastian Rouven Brückner, Jonas Schäfer, Narain Karedla, *Sebastian Isbaner*, Dirk Hähnel, Ingo Gregor, Jörg Enderlein, Andreas Janshoff, and Alexey I. Chizhik. "Cell–Substrate Dynamics of the Epithelial-to-Mesenchymal Transition." In: *Nano Letters* 17.5 (May 10, 2017), pp. 3320–3326. DOI: [10.1021/acs.nanolett.7b01558](https://doi.org/10.1021/acs.nanolett.7b01558)
- 2016 *Sebastian Isbaner*¹, Narain Karedla¹, Daja Ruhlandt, Simon Christoph Stein, Anna Chizhik, Ingo Gregor, and Jörg Enderlein. "Dead-time correction of fluorescence lifetime measurements and fluorescence lifetime imaging." In: *Optics Express* 24.9 (May 2, 2016), pp. 9429–9445. DOI: [10.1364/OE.24.009429](https://doi.org/10.1364/OE.24.009429)
- 2013 Yang Zhang, *Sebastian Isbaner*, and Dieter W. Heermann. "Mechanics of Sister Chromatids studied with a Polymer Model." In: *Frontiers in Physics* 1 (2013). DOI: [10.3389/fphy.2013.00016](https://doi.org/10.3389/fphy.2013.00016)

¹ These authors contributed equally to this work.

CONFERENCES

Talks

- 2018 | Biophysics by the Sea, Alcudia
Single Molecule Metal-Induced Energy Transfer for Axial Localization
Quantitative Bio-Imaging (QBI), Göttingen
Superresolution Upgrade for Confocal Spinning Disk Systems
- 2017 | Biophysics by the Sea, Alcudia
Superresolution Upgrade for Confocal Spinning Disk Systems using Image Scanning Microscopy
PicoQuant 23rd International Workshop on Single Molecule Spectroscopy and Super-resolution Microscopy in the Life Sciences, Berlin
Nanometer Axial Co-localization of Single Emitters Using Metal-induced Energy Transfer
SPIE Security and Defense: Commercial + Scientific Sensing and Imaging, Anaheim – *invited talk*
Dead-time Correction for TCSPC Systems
SPIE Photonics West BIOS, San Francisco
Superresolution Upgrade for Confocal Spinning Disk Systems using Image Scanning Microscopy
- 2016 | PicoQuant 22nd International Workshop on Single Molecule Spectroscopy and Super-resolution Microscopy in the Life Sciences, Berlin
Dead-time Correction of Fluorescence Lifetime Measurements and Fluorescence Lifetime Imaging
Biophysics by the Sea, Alcudia
Dead-time Correction of Fluorescence Lifetime Measurements and Fluorescence Lifetime Imaging
- 2015 | Novel Probes for Fluorescence Microscopy, Göttingen
Application of Metal-induced Energy Transfer to Study the Dynamics of Lipid Bilayers

Posters

- | | |
|------|---|
| 2018 | PicoQuant 24th International Workshop on Single Molecule Spectroscopy and Super-resolution Microscopy in the Life Sciences, Berlin <i>Superresolution Upgrade for Confocal Spinning Disk Systems</i> |
| 2016 | International Discussion Meeting – FRET in Life Sciences II, Göttingen <i>Simultaneous Measurements of Thickness and Diffusion of Lipid Bilayers using MIET and 2f-FLCS</i> |
| 2015 | Third Infinity, Göttingen <i>Simultaneous Measurements of Thickness and Diffusion of Lipid Bilayers using MIET and 2f-FLCS</i> |

TEACHING

- | | |
|------|--|
| 2017 | Methods Course: Basics of Fluorescence Microscopy and Spectroscopy in Biophysics Göttingen University |
| 2016 | Tutor for Experimental Physics III: Oscillations and Waves Göttingen University |
| 2015 | Tutor for Introduction into Biophysics Göttingen University |
| 2012 | Tutor for Theoretical Physics II: Analytical Mechanics and Thermodynamics Heidelberg University |
| 2012 | Tutor for physics lab course Heidelberg University |

OTHER PROFESSIONAL ACTIVITIES

- | | |
|-------------|--|
| 2016 – 2018 | Student representative and board member of the IMPRS-PBCS graduate school, Göttingen |
| 2016 | Co-organizer of the retreat of the IMPRS-PBCS graduate school |
| 2015 | Co-organizer student conference “Third Infinity”, Göttingen |